On Turbulence Transition in Shear Flows

Dissertation

zur

Erlangung des Doktorgrades

der Naturwissenschaften

(Dr. rer. nat.)

dem Fachbereich Physik

der Philipps-Universität Marburg

vorgelegt von

Marina Kristin Pausch

aus Marburg

Marburg, 2018

Vom Fachbereich Physik der Philipps-Universität Marburg
(Hochschulkennziffer 1180) als Dissertation angenommen am: 6.12.2018
Autorin: Dipl.-Phys. Marina Kristin Pausch
Erstgutachter: Prof. Dr. Bruno Eckhardt, Philipps-Universität Marburg
Zweitgutachter: Dr. Yongyun Hwang, Imperial College London
Tag der mündlichen Prüfung: 13.12.2018

Wahrlich es ist nicht das Wissen, sondern das Lernen,
nicht das Besitzen, sondern das Erwerben,
nicht das Da-Seyn, sondern das Hinkommen,
was den grössten Genuss gewährt.
(Carl Friedrich Gauß)

Zusammenfassung

Der Übergang zur Turbulenz in linear stabilen Scherströmungen wie der Rohrströmung und der ebenen Couette Strömung ist seit vielen Jahren Gegenstand aktiver Forschung. Die Anwendung der Theorie dynamischer Systeme hat das Verständnis der zugrundeliegenden physikalischen Mechanismen enorm verbessert. Insbesondere die Suche nach exakten Lösungen der Navier-Stokes Gleichungen, wie Fixpunkten oder periodischen Orbits, liefert Einblicke in die turbulente Dynamik, da diese sogenannten exakten kohärenten Strukturen der turbulenten Bewegung im Zustandsraum zugrundeliegen. Direkte numerische Simulationen (DNS) der Navier-Stokes Gleichungen stellen selbst für einfache Geometrien eine Herausforderung dar, da viele zeitliche und räumliche Skalen aufgelöst werden müssen. Daher bedarf es der Entwicklung effizienter, niedrigdimensionaler Modelle zur weiteren Untersuchung des Turbulenzübergangs.

Einfache, grundlegende Modelle bestehen aus einem Wirbel und einem Streak, sowie einer Nichtlinearität. Das sind die Basisbestandteile der transienten Verstärkung von Störungen und des sich selbst erhaltenden Prozesses, die wiederum den Übergang zur Turbulenz verursachen. Wir vergleichen deterministische und Rausch-induzierte Übergänge für ein solches niedrigdimensionales Modell und wir finden qualitativ verschiedene Übergangsszenarien.

Ein vielversprechender Ansatz sind quasilineare Näherungen, für die die Nichtlinearität der Navier-Stokes Gleichungen auf einen kleinen Teil reduziert wird, der ausreichend ist, um die turbulente Dynamik aufrechtzuerhalten. Die Geschwindigkeitsfelder werden dazu in zwei Gruppen von Moden zerlegt und nur gewisse Kopplungen zwischen den Gruppen werden beibehalten. Insbesondere werden alle Selbstwechselwirkungen zwischen den Moden der zweiten Gruppe vernachlässigt, bis auf diejenigen, die zurück an die erste Gruppe koppeln. Wir implementieren verschiedene Varianten quasilinearer Näherungen in DNS der ebenen Couette Strömung und untersuchen diese Modellsysteme unter Gesichtspunkten der Theorie dynamischer Systeme, das heißt, wir studieren den ihnen

zugrundeliegenden Zustandsraum.

Für die in Strömungsrichtung quasilineare Näherung beschreiben die beiden Gruppen das Strömungsfeld mit bzw. ohne Variation in Strömungsrichtung. In den Gleichungen der zweiten Gruppe werden die Selbstwechselwirkungen zwischen in Strömungsrichtung variierenden Moden vernachlässigt. Ein detaillierter Vergleich der quasilinearen Näherung und des vollen Systems ist möglich für die exakten kohärenten Strukturen, die in der ebenen Couette Strömung existieren. Das Verfolgen bekannter Fixpunkte des vollen nichtlinearen Systems in die quasilineare Näherung liefert qualitativ ähnliche Geschwindigkeitsfelder und mittlere Strömungsprofile. Die Bifurkationsdiagramme der Zustände und insbesondere die Bifurkationspunkte werden durch die Näherung gut erfasst. Zudem konnten wir einer Bifurkationskaskade folgen, die ausgehend von einem Fixpunkt des Systems zur Ausbildung eines lokalen chaotischen Attraktors führt, analog zum vollen nichtlinearen System.

Eine interessante Eigenschaft dieser in Strömungsrichtung quasilinearen Näherung ist die Tatsache, dass nur einige wenige Moden zu den quasilinearen Zuständen beitragen. Obwohl die Anzahl aktiver Moden beträchtlich reduziert ist, sind viele Eigenschaften des vollen Systems auch im quasilinearen Modell enthalten. Mit zunehmender Reynoldszahl können über instabile Eigenvektoren und Bifurkationen der Zustände weitere Moden aktiv werden. Wenn die zusätzlichen Moden nacheinander auftauchen, zeigen ihre Amplituden ein intermittentes Verhalten.

Mit generalisierten quasilinearen Näherungen können wir systematisch zwischen der in Strömungsrichtung quasilinearen Näherung und dem vollen nichtlinearen System interpolieren, indem wir die Anzahl der Moden in der ersten Gruppe vergrößern. Das führt zu einer quantitativen Verbesserung der Ergebnisse der Näherung im Vergleich zum vollen System, aber die Reduzierung der Anzahl aktiver Moden geht dabei verloren.

Die Ergebnisse zeigen, dass diese quasilinearen Näherungen die Untersuchung vereinfachter Modellsysteme ermöglichen, die die Eigenschaften des vollen nichtlinearen Systems besitzen und die direkt und systematisch aus den Navier-Stokes Gleichungen abgeleitet werden.

Abstract

The onset of turbulence in shear flows like pipe flow or plane Couette flow, for which the laminar profile is linearly stable for all Reynolds numbers, has remained a puzzle for many years. Immense progress towards the understanding of the underlying physical mechanisms has been made by the application of ideas from dynamical systems theory. In particular, the search for exact solutions of the Navier-Stokes equations, like fixed points and periodic orbits, allowed a better grasp of the turbulent dynamics as these exact coherent structures are underlying the turbulent motion in state space. Direct numerical simulations (DNS) of the Navier-Stokes equations are challenging, even for simple geometries, as many spatial and temporal scales need to be resolved. Therefore, there exists a need to develop efficient, low-dimensional models to further explore the features of the transition to turbulence.

The most elementary models consist of a vortex and a streak plus a nonlinearity. These are the basic ingredients for the transient amplification of perturbations and the self-sustaining process, which in turn cause the transition. We compare deterministic and noise-induced transitions for such a low-dimensional model and we find qualitatively different transition states for the different scenarios.

A promising ansatz are quasilinear approximations, for which the nonlinearities of the Navier-Stokes equations are restricted to a small set which is sufficient to maintain turbulent dynamics. For this purpose, the velocity fields are decomposed into two groups of modes, and only certain couplings between the groups are kept. In particular, all self-interactions within the second group are neglected, except for the ones that map to the first group, thereby introducing a feedback from the second to the first group. We implement quasilinear approximations into DNS of plane Couette flow and analyze these models from a dynamical systems perspective, i.e. we investigate their underlying state space

structure.

For the streamwise quasilinear approximation, the first and the second group describe the flow field without and with variation in downstream direction, respectively. In the equations of the second group, the self-interactions between streamwise varying modes are neglected. A detailed comparison between the approximation and the full system is possible for the exact coherent structures in plane Couette flow. From the continuation of known fixed points of the full nonlinear system to the streamwise quasilinear system we observe qualitatively similar velocity fields and mean profiles. The bifurcation diagrams of the states and in particular the bifurcation points are captured well by the approximation. Furthermore, we were able to follow a bifurcation cascade starting at an exact coherent structure and leading to the formation of a local chaotic attractor, by analogy with the fully nonlinear system.

An interesting property of the streamwise quasilinear model is that the energy spectra of the quasilinear states contain a few elements only. Even though the set of active modes is considerably reduced, many features of the full system can be found within the streamwise quasilinear approximation. With increasing Reynolds number, further modes can be activated by unstable eigenvectors and bifurcations. When the additional modes subsequently emerge, their amplitudes show intermittent behaviour.

In a generalized quasilinear setting we can systematically interpolate between the quasilinear approximation and the fully nonlinear system by increasing the set of modes contained in the first group. This leads to a quantitative improvement of the results compared to the full system, but the reduction in the number of active modes is lost.

The results show that the quasilinear approximation allows to systematically deduce from the Navier-Stokes equations simplified models that share the characteristics of the full system, and that should be useful for further analytical representations of the dynamics of transitional shear flows.

Contents

1 Introduction

The nature of the transition to turbulence in shear flows is a question which has first been adressed in the famous publication by Reynolds (1883) "An experimental investigation of the circumstances which determine whether the motion of water shall be direct or sinuous, and of the law of resistance in parallel channels" and which has puzzled scientists ever since. Turbulence has been an active field of research for many years, but still the question of how a fluid flow changes from regular, laminar motion to irregular, turbulent motion is not fully understood. The investigation of the transition to turbulence and its underlying mechanisms is not only a question of fundamental research, but there are also many engineering applications where the transition should be either triggered or avoided mostly in order to save energy. For example, turbulence is desirable for the efficient mixing of two fluids in industrial processes, while the wings of aircrafts are designed so as to delay the transition to turbulence in their boundary layer and thereby to reduce skin friction drag.

In his pipe flow experiments Reynolds observed that whether a transition to turbulence in the pipe can be triggered by finite amplitude perturbations depends on the ratio of the product of the fluid velocity and the diameter of the pipe to the fluid's viscosity. This dimensionless parameter today is known as the Reynolds number (Sommerfeld, 1908; Rott, 1990). For low Reynolds numbers up to a critical value the flow always relaminarizes and for high Reynolds numbers above a second critical value the flow is always turbulent. Inbetween the flow exhibits a transition to turbulence depending on the strengh and the type of perturbations. The critical amplitude of perturbations that trigger a transition decreases with increasing Reynolds number. This double threshold for transition, i.e. the requirement of exceeding a critical Reynolds number as well as a critical perturbation amplitude, comes about because pipe flow falls into the class of shear flows which show a subcritical transition to turbulence.

This means turbulent dynamics arises although the laminar profile is still linearly stable. This class of flows also contains plane Couette flow which is studied in this thesis. It describes a fluid sheared between two infinitely extended plates that move into opposite directions.

An important approach towards the understanding of the transition to turbulence in linearly stable shear flows originates from dynamical systems theory. It consists of searching for unstable exact numerical solutions of the equations of motion, i.e. the Navier-Stokes equations, like fixed points and periodic orbits (Nagata, 1990; Schmiegel and Eckhardt, 1997). Such solutions form the scaffold underlying the turbulent motion in state space. From a dynamical system's perspective this means that the turbulent region of state space consists of numerous unstable invariant solutions and a chaotic trajectory approaches one solution along its stable manifold, gets pushed away along its unstable direction, again gets attracted by another solution and so forth. Since all the states are unstable they can only show up transiently during the evolution of the turbulent flow, but they have been identified in experiments and numerical simulations (Hof et al., 2004; Kerswell and Tutty, 2007; Schneider et al., 2007a; Eckhardt et al., 2008; Cvitanović and Gibson, 2010). In addition, there are particular exact solutions that lie on the boundary between the laminar and the turbulent regime in state space, so-called *edge states*; the boundary is formed by their stable manifold (Skufca et al., 2006; Schneider et al., 2007b, 2008; de Lozar et al., 2012). The unstable exact numerical solutions appear in saddle-node bifurcations in a finite distance from the laminar state. They form a chaotic saddle in state space consisting of more and more such structures with increasing Reynolds number. Hence, a sufficiently strong perturbation of the laminar flow can lead to turbulent motion.

Although the equations of motion have already been derived in the middle of the 19th century by Navier and Stokes, only few analytical solutions are known as they form a system of nonlinear partial differential equations and thus are very difficult to solve. This is why the availability of powerful computers led to enormous progress towards the understanding of turbulent flows as it became possible to numerically solve the equations of motion, at least for simple geometries. For the computation of "real" problems with complex geometries

like the flow of air around an airplane, fully-resolved direct numerical simulations (DNS) quickly reach their limits as high resolutions are required due to the strong interactions between small and large scales in space and in time. Therefore, one has to rely on simplified models and approximations to make predictions for such flows.

Studying simplyfied models has often proven to be useful for the investigation of the transition to turbulence in linearly stable shear flows, for example Waleffe (1997); Moehlis et al. (2004, 2005); Barkley (2011). The dynamical importance of streaks, i.e. streamwise coherent structures, in the transition to turbulence motivated the use of streamwise constant and streamwise averaged models (Farrell and Ioannou, 2012; Thomas et al., 2014, 2015; Bretheim et al., 2015), in which the flow field is decomposed into a streamwise constant mean velocity profile and a streamwise varying perturbation flow field. One set of models which use such a decomposition are quasilinear approximations for which certain terms of the nonlinear couplings are neglected. Previous studies using quasilinear approximations compared properties for dynamically active states, flow statistics and mean profiles and have, for example, successfully been used to describe atmospheric currents (Marston et al., 2016; Tobias and Marston, 2017; Thomas et al., 2014, 2015; Nikolaidis et al., 2016).

In this thesis the transition to turbulence in linearly stable shear flows is investigated using low-dimensional models and direct numerical simulations to examine ideas from dynamical systems theory. We will apply quasilinear and generalized quasilinear approximations to the simulation of plane Couette flow and analyse them from a dynamical systems perspective. In particular, we will focus on exact coherent structures which have the advantage to be stationary and simple. Therefore, such structures are easy to compare to their counterparts from full numerical simulations.

Chapter 2 gives a more detailed introduction into the governing equations of fluid flow and the transition to turbulence including the ideas from dynamical systems theory. Furthermore, the quasilinear and generalized quasilinear approximations are explained. In chapter 3 optimal perturbations of the laminar state that trigger a transition are investigated for a shear flow model. In chapter 4 we show that the 9-mode shear flow model by Moehlis, Faisst and Eckhardt

can easily be separated into streamwise constant and streamwise varying modes without further approximation and we analyse its properties from a quasilinear approximation perspective. Subsequently, in chapters 5 and 6, exact coherent structures, i.e. fixed points and traveling wave solutions, in transitional plane Couette flow are investigated within the quasilinear and the generalized quasilinear approximation. The results are presented and compared to the results of the full DNS. The last chapter contains the conclusions and a brief outlook.

2 Theoretical Background

2.1 Navier-Stokes equation and Reynolds number

The fundamental equations of motion for incompressible Newtonian fluids are the Navier-Stokes equations. They form a system of nonlinear partial differential equations for the velocity field $\vec{v}(\vec{x}, t)$ of the flow:

$$\frac{\partial \vec{v}}{\partial t} + (\vec{v}\,\vec{\nabla})\vec{v} = -\frac{\vec{\nabla} P}{\rho} + \nu \Delta \vec{v} + \vec{f} \tag{2.1}$$

with the continuity equation

$$\vec{\nabla}\,\vec{v} = 0, \tag{2.2}$$

where P is the pressure, ρ is the constant density of the fluid, ν is the kinematic viscosity and $\vec{f}$ describes a possible volume force density.

For a Newtonian fluid the shear stress is directly proportional to the velocity gradient and the viscosity is not affected by the shear. Many common fluids like water, air and oil are Newtonian fluids and they can be treated as incompressible as long as the velocity of the flow is well below the speed of sound. By contrast, blood and toothpaste are examples for Non-Newtonian fluids and their motion is not governed by the Navier-Stokes equations in the form given above.

The Navier-Stokes equations inherit all the complexity of fluid flows, therefore it cannot be expected that their solutions are simple. In fact, solving the Navier-Stokes equation poses a big challenge to physicists, engineers and mathematicians and simplifications and models are often needed when studying fluid dynamics. The computer-based numerical investigation of the Navier-Stokes equations using so-called Direct Numerical Simulation (DNS) is possible for simple geometries and moderate Reynolds numbers, but seems to be out of reach in the coming years for “real” problems like the flow around vehicles or

meteorological phenomena.

An important quantity in fluid mechanics for the classification and prediction of flow behaviour is the dimensionless Reynolds number Re. It is a combination of typical system parameters and it describes the competition between inertia and viscous diffusion in the flow:

$$Re = \frac{|(\vec{v}\,\vec{\nabla})\vec{v}|}{|\nu\Delta\vec{v}|} \approx \frac{U^2/L}{\nu U/L^2} = \frac{UL}{\nu}, \tag{2.3}$$

where U is a typical velocity and L is a typical size of the system. The inertial forces, represented by the advective term $(\vec{v}\,\vec{\nabla})\vec{v}$, drive the fluid to maintain its movement while the viscous forces $\nu\Delta\vec{v}$ absorb kinetic energy of the flow by internal friction. For low Reynolds numbers the viscous forces are dominant and the fluid flows in parallel layers between which no mixing occurs. This is the laminar flow regime. Turbulence, i.e. a chaotic and unpredictable motion of the fluid, arises at high Reynolds numbers where there is not much influence of viscosity and the advection becomes dominant. Typical Reynolds numbers range from 10^{-5} for bacteria, over 10^5 for a jogger to 10^9 for an airplane.

With the Reynolds number, the dimensionless velocity $\vec{u} = \vec{v}/U$, position $\vec{x} = \vec{x}'/L$ and pressure $p = P/(\rho U^2)$, the Navier-Stokes equations can be written in dimensionless form:

$$\frac{\partial\vec{u}}{\partial t} + (\vec{u}\,\vec{\nabla})\vec{u} = -\vec{\nabla}p + \frac{1}{Re}\Delta\vec{u} + \vec{f} \tag{2.4}$$

with

$$\vec{\nabla}\,\vec{u} = 0. \tag{2.5}$$

The Reynolds number remains the only control parameter for a flow with a given geometry and boundary conditions. If two flows have the same geometry but on a different overall scale, they are hydrodynamically similar provided the Reynolds numbers are the same. This fact is used in engineering for the design of experiments in water channels or wind tunnels on reduced scales.

2.2 Transition to turbulence in shear flows

A fast flow of a fluid will become turbulent, i.e. irregular, rapidly varying and chaotic. The most obvious idea about the transition from the smooth and time-independent laminar flow to that substantially different flow state is that the laminar flow is stable at low Reynolds numbers before it loses stability at a critical Reynolds number Re_c. Such a transition is called "supercritical". Above the critical point such flows show a rich variety of patterns which become increasingly complex with increasing Reynolds number, finally leading to turbulent motion. For instance, in the co-rotating case of Taylor-Couette flow (the flow in the gap between two rotating cylinders), the flow becomes centrifugally unstable when the inner cylinder is rotating faster than the outer cylinder and one observes a cascade to turbulence from so-called Taylor vortex flow, over wavy vortex flow, modulated wavy vortices and turbulent Taylor vortices, finally leading to featureless turbulence with transitions between the flow regimes at well-defined values of the Reynolds number (Andereck et al., 1986). This route to turbulence has been confirmed within linear stability theory not only for Taylor-Couette flow, but also for Rayleigh-Bénard flow (the flow between two parallel planes heated from below) and other flow situations, where transition has been successfully predicted.

For other shear flows like plane Couette flow or pipe flow, the laminar profile remains linearly stable for all Re (Romanov, 1973; Schmid and Henningson, 1999; Meseguer and Trefethen, 2003), but nevertheless a transition to turbulence has been observed in experiments and simulations for $Re \approx 2000$ in pipe flow (with Re defined by diameter of the pipe and mean velocity) and $Re \approx 300$ in plane Couette flow (with Re defined by half the gap width between the plates and half their velocity difference). For plane Poiseuille flow (the pressure-driven flow between parallel plates) linear stability theory predicts an instability at $Re_c = 5772$, far beyond the experimentally observed transition near $Re = 1000$ (Orszag, 1971; Orszag and Kells, 1980). Such a transition is called "subcritical". There is a lower critical value of the Reynolds number below which all perturbations decay and the flow always remains laminar, and there is an upper critical value of Re above which the flow is always turbulent. For intermediate values of Re

a double threshold exists, i.e. a transition to turbulence occurs depending on the amplitude and shape of disturbances, with the critical amplitude decreasing with increasing Re (Darbyshire and Mullin, 1995; Hof et al., 2003; Mellibovsky and Meseguer, 2009).

For these flows the transition mechanism is not well understood. There are no states of simpler dynamics between the laminar state and turbulence, as can be observed for flows with linear instability like the rolls in Rayleigh-Bénard convection or the Taylor vortices in the Taylor-Couette system, but the flow pattern is immediately temporally and spatially fluctuating (Moxey and Barkley, 2010; Duguet et al., 2010). Due to the linear stability of the laminar state localized turbulent spots (puffs and slugs in pipe flow or oblique stripes in plane Couette flow) emerge for transitional Reynolds numbers (Prigent et al., 2003; Prigent and Dauchot, 2005; Duguet and Schlatter, 2013). For pipe flow Avila et al. (2011) estimated a critical Re for the onset of persistent turbulent dynamics from the balance of the decay and splitting rates of turbulent puffs.

2.2.1 Non-normal energy amplification and nonlinear mixing

An explanation for the transition to turbulence of these wall-bounded shear flows despite their linear stability is the combination of non-normal energy growth with nonlinear mixing (Boberg and Brosa, 1988; Trefethen et al., 1993; Gebhardt and Grossmann, 1994; Grossmann, 2000; Eckhardt and Pandit, 2003). Due to the linear stability of the laminar flow, ultimately all infinitesimal disturbances have to decay. Nevertheless, perturbations can grow transiently, because the linearized operator of the Navier-Stokes equations is non-normal with non-orthogonal eigenfunctions. Perturbations will be damped in the directions overlapping with these eigenfunctions, but in the other directions disturbances can grow and draw energy from the laminar profile and thus from the shear before they decay. Therefore, the perturbations which have only little overlap with the eigenfunctions experience the biggest energy growth. Typically, they are downstream vortices which then modulate the base flow in such a way that there are regions with faster and slower streamwise velocity, the so-called streaks. However, non-normal amplification alone does not suffice to explain the transition to turbulence in these systems as all streamwise perturbations

will eventually decay, because all eigenvalues are negative. Here the energy-preserving nonlinearity $(\vec{u}\vec{\nabla})\vec{u}$ comes into play, which, due to the differential operator, not only changes the amplitude but also the direction of the perturbations. The nonlinearity mixes the modes and recreates non-overlapping modes, i.e. spanwise modulations of the flow field, which can again experience an energy growth leading to a break-down of the streaks and finally to the regeneration of the streamwise vortices. Waleffe (1997) investigated this cycle and termed it the *self-sustaining process*. In the Navier-Stokes dynamics this mechanism seems to be in a good balance with energy dissipation so that there is neither an infinite amplification nor a decay of all disturbances and the dynamics may become turbulent. However, it is likely that turbulence in these linearly stable systems is not persistent, but of a transient nature (Brosa, 1989; Eckhardt et al., 1998; Eckhardt and Mersmann, 1999; Hof et al., 2006, 2008; Avila et al., 2010; Schneider et al., 2010b).

2.2.2 Dynamical systems theory and exact coherent structures

In the past years progress towards understanding the onset of turbulence for linearly stable shear flows has been made by pursuing ideas from dynamical systems theory.

The state space of the system consists of all velocity fields that satisfy the respective boundary conditions; it contains the laminar profile as stable fixed point as well as unstable invariant solutions of the Navier-Stokes equation. They appear in saddle-node bifurcations at a finite distance from the laminar state and their number increases with Re. Such exact coherent structures (ECS) can be equilibria, traveling waves or periodic orbits. Equilibria are stationary 3d flow patterns, traveling waves are equilibria which experience a drift in the translationally invariant directions, and periodic orbits are solutions which are repeated after some finite time. These ECS together with their stable and unstable manifolds form the scaffold on which the continuous turbulent trajectory lives in state space. From a dynamical systems perspective turbulence can then be described as “a walk among unstable solutions” (Schneider et al., 2010a).

The first examples of such structures have numerically been found for plane Couette flow by Nagata (1990) and have been analysed further by Clever and

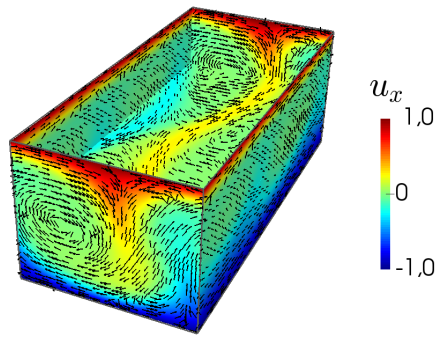

Figure 2.1: Velocity field of the NBC state at $Re = 400$. It consists of a pair of streamwise vortices and a pair of downstream streaks. The velocity in the streamwise direction is color-coded, the arrows show the in-plane velocities.

Busse (1997) and Waleffe (2003). This so-called Nagata-Busse-Clever (NBC) state consists of a pair of streaks and a pair of counter-rotating vortices, see figure 2.1. Today many invariant solutions are known, see for example Schmiegel (1999) and Gibson et al. (2009). The equilibria as well as the traveling waves and periodic orbits are unstable. They will not appear persistently during the time-evolution of the velocity field, but close passes to these solutions have been observed in experiments and simulations (Hof et al., 2004; Schneider et al., 2007a; Eckhardt et al., 2008; Cvitanović and Gibson, 2010). It was shown that the transition to turbulence is related to the presence of these exact coherent structures in state space.

Kreilos and Eckhardt (2012) adressed the question of what happens between the emergence of the first coherent structures and the onset of turbulence and they were able to find a bifurcation cascade starting at the upper branch NBC state, see figure 2.2. The figure shows the maxima of the cross-flow energy, i.e. the energy contained in the transversal flow components, versus the Reynolds number, for a trajectory starting near the upper branch state. Right after the NBC states appear in a saddle-node bifurcation at $Re_c = 163.8$, the upper branch state is linearly stable (within the considered domain size and symmetry

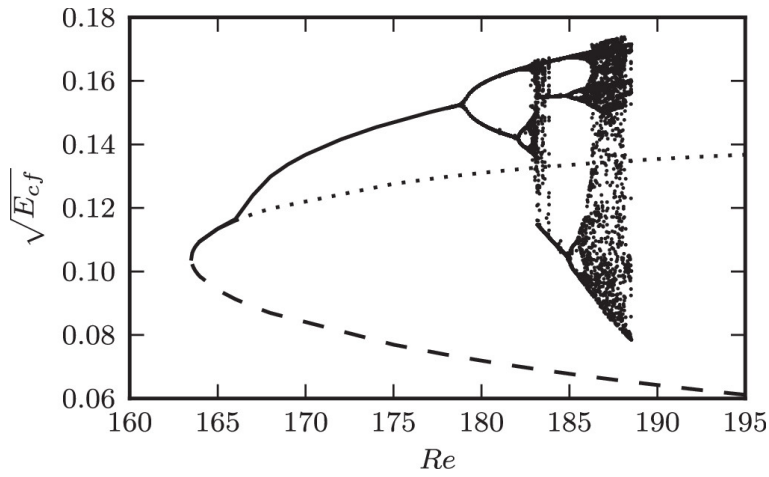

Figure 2.2: (Reprinted from Kreilos and Eckhardt (2012) with permission of AIP Publishing.) Square root of the cross flow energy versus Re for the NBC states and the emerging chaotic attractor. The NBC states appear in a saddle-node bifurcation at $Re = 163.8$. The unstable lower branch state is shown as a dashed line. The stable upper branch state is shown as a solid line and it is shown as a dotted line after it became unstable in a Hopf bifurcation. A period-doubling cascade leads to chaotic bands with a period-3 window. At $Re = 188.51$ the attractor is destroyed in a crisis bifurcation and all trajectories decay to the laminar state.

subspace). A stable periodic orbit is created in a Hopf bifurcation at $Re = 166.05$ (Clever and Busse, 1997), followed by a cascade of period-doubling bifurcations that lead to the creation of a chaotic attractor. The lower branch state (dashed line) is the edge state; it has one unstable direction only and its stable manifold separates the basin of attraction of the laminar state from that of the chaotic attractor (Skufca et al., 2006; Schneider et al., 2007b, 2008). At $Re = 188.51$ the attractor is suddenly destroyed in a crisis bifurcation and there remains a transient chaotic saddle (Grebogi et al., 1983). Trajectories can now leave the saddle and decay to the laminar profile; there is an exponential distribution of lifetimes and a sensitive dependence on initial conditions (Kreilos et al., 2014).

Figure 2.3 shows a sketch of the corresponding state space portrait near the onset of turbulence, starting from the saddle-node bifurcation of the NBC states,

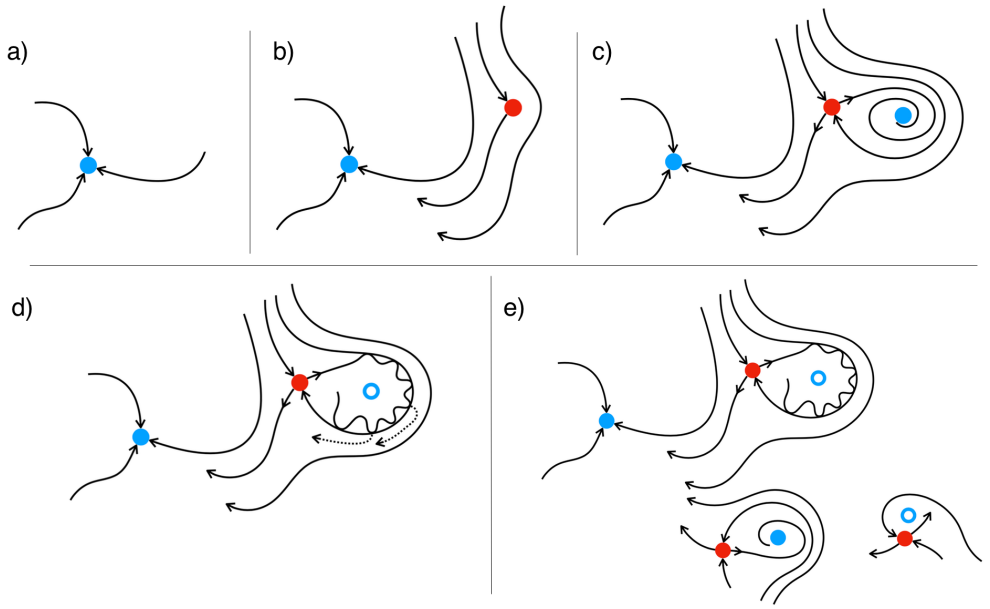

Figure 2.3: State space portrait near the transition to turbulence (adapted from Eckhardt (2018)). a) For small Re the laminar profile is the only stable fixed point of the system (blue dot; the arrows indicate its stability). b) At the critical point a new exact coherent structure emerges (red dot) which attracts one initial condition. c) Above Re_c the structure splits up into a saddle state (red) and a node state (blue) and there is a bubble-shaped region of initial conditions that are attracted to the node. d) The chaotic attractor touches its own boundary and changes to a chaotic saddle (blue circle). Trajectories can escape the saddle and be attracted towards the laminar profile. e) For higher Re there is an increasingly complex network of unstable states with their stable and unstable manifolds on which the chaotic trajectory lives.

adapted from Eckhardt (2018). In the following, the lower and upper branch NBC equilibria will be called EQ1 and EQ2, respectively. They are born in a saddle-node bifurcation at a critical Reynolds number that depends on the size of the periodic domain. Below the critical Reynolds number all initial conditions are attracted towards the laminar profile which is the only stable fixed point of the system, figure 2.3a. At the critical point Re_c one equilibrium point (red dot) appears in state space which attracts one initial condition. All other initial conditions are attracted towards the stable laminar fixed point (blue dot), see figure 2.3b. For higher Re this state bifurcates into a saddle (EQ1, red dot) and a node (EQ2, blue dot), shown in 2.3c. The saddle point EQ1 has one unstable direction only, which leads a trajectory either towards the laminar state or towards the node EQ2 which is stable for values of Re slightly above Re_c. The basin of attraction of the stable node has the shape of a droplet with a long and thin tail. With increasing Re the node becomes more and more unstable and undergoes a sequence of secondary bifurcations which lead to periodic orbits and finally to a chaotic attractor, while the bubble-shaped basin of attraction grows. The laminar and the turbulent regime in state space are separated by the "edge of chaos" (Skufca et al., 2006), which is the stable, co-dimension one manifold of the edge state (EQ1). At some point in Re the attractor touches the stable manifold of EQ1, i.e. its own boundary, and the basin of attraction is not closed anymore, but becomes a chaotic saddle (Kreilos and Eckhardt, 2012), figure 2.3d. Such a behaviour is called crisis bifurcation (Grebogi et al., 1983) and turbulent trajectories can escape from the chaotic saddle and decay to the laminar state, and their lifetime depends sensitively on the initial condition. With increasing Re, the lifetimes increase and the saddle grows in state space (Kreilos et al., 2014). Moreover, the network of such states in state space becomes increasingly complex, see figure 2.3e.

This route to the creation of a chaotic saddle is expected to be generic. When Re increases, more such chaotic saddles will appear, originating from further saddle-node bifurcations via chaotic cascades. In contrast to the situation described above, where the bifurcation cascade started from a stable state (within the chosen symmetry-subspace and computational domain), the fixed points usually are unstable. Therefore the bifurcation cascade has to happen in an

unstable subspace of the full system, no global attractor is created and thus the mechanism is difficult to detect.

In summary: Whether an initial condition is able to trigger a transition to turbulence for a certain Reynolds number depends on the amplitude of the disturbance and on its shape. For low Re no exact coherent structures exist, the basin of attraction of the laminar state covers all state space and all perturbations decay to the laminar profile. With increasing Re more and more exact coherent structures emerge and the basin of attraction of the laminar state shrinks. An (amplified) initial condition becomes turbulent if it crosses the edge of chaos and gets caught by the chaotic saddle. The lifetime of the turbulent trajectory grows with Re as the probability that the trajectory leaves the increasingly complex jungle formed by unstable states and their stable and unstable manifolds decreases.

2.3 Quasilinear approximation for shear flows

As mentioned above, treating the Navier-Stokes equations with their full nonlinearities by direct numerical simulations is challenging even for simple geometries when it comes to higher Reynolds numbers. The difficulties come about because of the large variability of scales in space and time and their interactions and they have led to the development of many simplified model systems to investigate the transition to turbulence and turbulent dynamics. For example, low-dimensional models can be obtained by Galerkin projection onto a low-dimensional space (Smith et al., 2005) or by modeling certain features of the flow and their interactions (Hamilton et al., 1995; Moehlis et al., 2004).

Another approach consists in a simplification of the Navier-Stokes equations themselves. Within the quasilinear approximation only a small set of nonlinear interactions is kept which is able to maintain turbulent dynamics. Quasilinear approximations have successfully reproduced features of shear flows (Thomas et al., 2014, 2015; Bretheim et al., 2015) and geostrophic flows (Farrell and Ioannou, 2007; Marston et al., 2016; Tobias and Marston, 2017). These models have especially been used for Direct Statistical Simulations where they can form the basis of a statistical closure. Different quasilinear approaches have in

common that the flow field is decomposed into two sets of modes. Then certain nonlinear couplings between the two sets are omitted and the equations of the second set thereby become quasilinear. The modes contained in the two sets can in principle be chosen arbitrarily.

The quasilinear approximation leads to a reduction of the complexity of the dynamics, but maintains the infinite degrees of freedom of the system. In addition, it has an appealing connection with marginal stability theory that is investigated in chapter 4 for two model systems. In chapters 5 and 6, we investigate different variations of quasilinear approximations, which are explained in the following.

For the definition of the quasilinear approximation a description of the velocity fields as a sum of incompressible basis modes $\vec{v}_l(\vec{x})$ with amplitudes $a_l(t)$ is required:

$$\vec{u}(\vec{x},t) = \sum_l a_l(t)\vec{v}_l(\vec{x}). \tag{2.6}$$

Direct numerical simulations of plane Couette flow use periodic boundary conditions in the translationally invariant streamwise and spanwise directions, in which the flow field is decomposed into Fourier modes. These Fourier modes provide an appropriate basis

$$\vec{u}(\vec{x}) = \sum_{k_x,k_z} \tilde{\vec{u}}_{k_x,k_z}(y)\, e^{2\pi i(k_x x/L_x + k_z z/L_z)}, \tag{2.7}$$

where $\tilde{\vec{u}}_{k_x,k_z}(y)$ are the spectral coefficients and k_x, k_z denote the Fourier wavenumbers in streamwise and spanwise direction, respectively.

2.3.1 Quasilinear approximation in streamwise direction

For the streamwise quasilinear approximation (QLA) for plane Couette flow that is applied in chapter 5 the incompressible flow field is decomposed into two parts

$$\vec{u} = \vec{u}_{\mathrm{I}} + \vec{u}_{\mathrm{II}}, \tag{2.8}$$

with

$$\vec{u}_{\mathrm{I}} = \tilde{\vec{u}}_0(y,z), \tag{2.9}$$

$$\vec{u}_{\mathrm{II}} = \sum_{k_x \neq 0} \tilde{\vec{u}}_{k_x}(y,z)\, e^{2\pi i k_x x/L_x}. \tag{2.10}$$

$\vec{u}_{\mathrm{I}}$ is invariant in downstream direction, i.e. it contains all modes with $k_x = 0$ like the mean flow, the streaks and the downstream vortices as well as their interactions. The second group $\vec{u}_{\mathrm{II}}$ consists of all modes with variation in streamwise direction. This decomposition into the streamwise mean flow and the perturbations is motivated by the prominence of streaks in turbulent dynamics which are kept by group I and the need to include 3-d modulations as in group II. It has been shown that streaks contribute a significant part to the turbulent kinetic energy (Morrison et al., 2004; Hutchins and Marusic, 2007a,b).

With the projections $\mathcal{P}_{\mathrm{I}}$ and $\mathcal{P}_{\mathrm{II}}$ onto these two divergence-free subspaces

$$\mathcal{P}_{\mathrm{I}}\vec{u} = \vec{u}_{\mathrm{I}} \tag{2.11}$$

$$\mathcal{P}_{\mathrm{II}}\vec{u} = \vec{u}_{\mathrm{II}} \tag{2.12}$$

which satisfy $\mathcal{P}_{\mathrm{I}} + \mathcal{P}_{\mathrm{II}} = \mathcal{I}$ (identity) and $\mathcal{P}_{\mathrm{I}}\mathcal{P}_{\mathrm{II}} = 0$, the nonlinear term of the Navier Stokes equation becomes

$$\begin{aligned}(\vec{u}\,\nabla)\vec{u} + \nabla\tilde{p} = \quad & \mathcal{P}_{\mathrm{I}}(\vec{u}_{\mathrm{I}}\nabla)\vec{u}_{\mathrm{I}} + \mathcal{P}_{\mathrm{I}}(\vec{u}_{\mathrm{II}}\nabla)\vec{u}_{\mathrm{II}} + \underbrace{\mathcal{P}_{\mathrm{I}}(\vec{u}_{\mathrm{I}}\nabla)\vec{u}_{\mathrm{II}}}_{=0} + \underbrace{\mathcal{P}_{\mathrm{I}}(\vec{u}_{\mathrm{II}}\nabla)\vec{u}_{\mathrm{I}}}_{=0} \\ & + \underbrace{\mathcal{P}_{\mathrm{II}}(\vec{u}_{\mathrm{I}}\nabla)\vec{u}_{\mathrm{I}}}_{=0} + \underbrace{\mathcal{P}_{\mathrm{II}}(\vec{u}_{\mathrm{II}}\nabla)\vec{u}_{\mathrm{II}}}_{\mathrm{QLA}\Rightarrow=0} + \mathcal{P}_{\mathrm{II}}(\vec{u}_{\mathrm{I}}\nabla)\vec{u}_{\mathrm{II}} + \mathcal{P}_{\mathrm{II}}(\vec{u}_{\mathrm{II}}\nabla)\vec{u}_{\mathrm{I}}\end{aligned} \tag{2.13}$$

where $\tilde{p}$ denotes the pressure terms that keep $(\vec{u}\,\vec{\nabla})\vec{u}$ incompressible.

Three out of these eight terms naturally become zero: Streamwise invariant modes coupled with streamwise invariant modes will not have a downstream modulation so that $\mathcal{P}_{\mathrm{II}}(\vec{u}_{\mathrm{I}}\nabla)\vec{u}_{\mathrm{I}} = 0$. Also a coupling between modes with and without a downstream modulation will not contribute to the streamwise invariant subspace, i.e. $\mathcal{P}_{\mathrm{I}}(\vec{u}_{\mathrm{II}}\nabla)\vec{u}_{\mathrm{I}} = 0$ and $\mathcal{P}_{\mathrm{I}}(\vec{u}_{\mathrm{I}}\nabla)\vec{u}_{\mathrm{II}}) = 0$.

Within the quasilinear approximation the self-interactions between modes of

the second group are neglected for the dynamics of $\vec{u}_{\mathrm{II}}$, i.e. $\mathcal{P}_{\mathrm{II}}(\vec{u}_{\mathrm{II}}\nabla)\vec{u}_{\mathrm{II}}$ is set to zero. For the quasilinear studies of chapter 5 a parameter q is introduced such that the system can be tuned between $q = 0$ corresponding to the quasilinear approximation and $q = 1$ corresponding to the full Navier-Stokes equation.

With the above decomposition the Navier-Stokes equation is split into two parts. One part, for which all nonlinearities are kept and which comprises all modes that are invariant in downstream direction

$$\partial_t \vec{u}_{\mathrm{I}} + \mathcal{P}_{\mathrm{I}}(\vec{u}_{\mathrm{I}}\nabla)\vec{u}_{\mathrm{I}} + \mathcal{P}_{\mathrm{I}}(\vec{u}_{\mathrm{II}}\nabla)\vec{u}_{\mathrm{II}} + \nabla p = \frac{1}{Re}\Delta\vec{u}_{\mathrm{I}}, \tag{2.14}$$

and the second part that contains all downstream variations and for which the nonlinear couplings among the $\vec{u}_{\mathrm{II}}$ modes have been neglected

$$\partial_t \vec{u}_{\mathrm{II}} + \mathcal{P}_{\mathrm{II}}(\vec{u}_{\mathrm{I}}\nabla)\vec{u}_{\mathrm{II}} + \mathcal{P}_{\mathrm{II}}(\vec{u}_{\mathrm{II}}\nabla)\vec{u}_{\mathrm{I}} = \frac{1}{Re}\Delta\vec{u}_{\mathrm{II}}. \tag{2.15}$$

This equation is quasilinear in that it is linear in $\vec{u}_{\mathrm{II}}$ with a parametric coupling to $\vec{u}_{\mathrm{I}}$. The feedback $\mathcal{P}_{\mathrm{I}}(\vec{u}_{\mathrm{II}}\nabla)\vec{u}_{\mathrm{II}}$ to the dynamics of $\vec{u}_{\mathrm{I}}$ is essential for the existence of nontrivial solutions (Moffatt, 1990; Farrell and Ioannou, 2012) and will be discussed further in chapter 4. Figure 2.4 shows a visualization of the interactions that are kept within the streamwise quasilinear approximation.

Previous studies within the quasilinear approximation focused on statistical properties of the flows that require time-integrations. Here, the focus is on the comparison of exact coherent structures and their bifurcations, i.e. the building blocks of turbulence from a dynamical system's perspective. The results will be presented in chapter 5.

2.3.2 Generalized quasilinear approximation

The generalized quasilinear approximation (GQL) has been introduced for the statistical simulation of zonal jets (Marston et al., 2016) and for rotating plane Couette flow (Tobias and Marston, 2017). Compared to the streamwise quasilinear approximation, the generalized quasilinear approximation consists in a different separation of modes. The flow field is decomposed into one group containing the large spatial scales and another group which contains the small

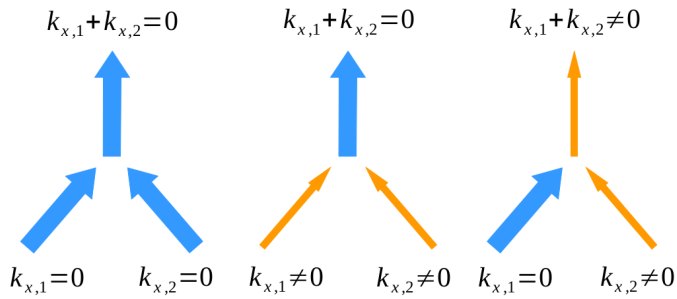

Figure 2.4: Visualization of the modes that are kept within the streamwise quasilinear approximation. For the dynamics of streamwise invariant modes with $k_x = 0$ (blue arrows) the self-interactions between streamwise invariant modes and the self-interactions between streamwise varying modes are kept. For the dynamics of the streamwise varying modes with $k_x \neq 0$ (orange arrows) only the nonlinear couplings between streamwise varying and streamwise invariant modes are kept.

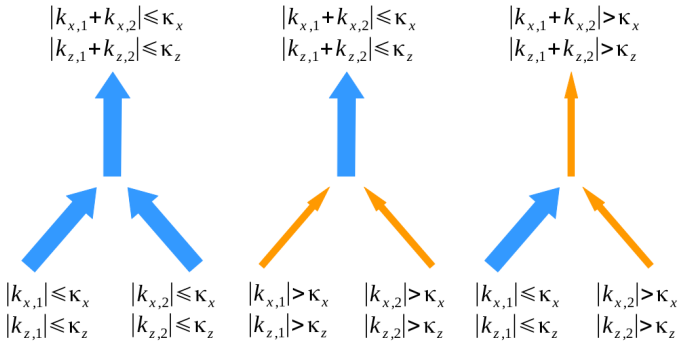

Figure 2.5: Visualization of the modes that are kept within the generalized quasilinear approximation. For the dynamics of the low wavenumber modes with $|k_x| \leq \kappa_x$ and $|k_z| \leq \kappa_z$ (blue arrows) the self-interactions between low wavenumber modes, i.e. $\mathcal{P}_{\mathrm{I}}(\vec{u}_{\mathrm{I}}\nabla)\vec{u}_{\mathrm{I}}$, and the self-interactions between high wavenumber modes, i.e. $\mathcal{P}_{\mathrm{I}}(\vec{u}_{\mathrm{II}}\nabla)\vec{u}_{\mathrm{II}}$ are kept. For the dynamics of the high wavenumber modes with $|k_x| > \kappa_x$, $|k_z| > \kappa_z$ (orange arrows) only the nonlinear couplings between low and high wavenumber modes, i.e. $\mathcal{P}_{\mathrm{II}}(\vec{u}_{\mathrm{I}}\nabla)\vec{u}_{\mathrm{II}} + \mathcal{P}_{\mathrm{II}}(\vec{u}_{\mathrm{II}}\nabla)\vec{u}_{\mathrm{I}}$ are kept.

spatial scales. As in Fourier space, large and small spatial scales are associated with small and high wavenumbers, respectively, this leads to the following decomposition of the velocity field:

$$\vec{u} = \vec{u}_{\mathrm{I}} + \vec{u}_{\mathrm{II}} \tag{2.16}$$

$$\vec{u}_{\mathrm{I}} = \sum_{|k_x|\leq\kappa_x} \sum_{|k_z|\leq\kappa_z} \tilde{\vec{u}}_{k_x,k_z}(y)\, e^{2\pi i k_x x/L_x + 2\pi i k_z z/L_z} \tag{2.17}$$

$$\vec{u}_{\mathrm{II}} = \sum_{|k_x|>\kappa_x} \sum_{|k_z|>\kappa_z} \tilde{\vec{u}}_{k_x,k_z}(y)\, e^{2\pi i k_x x/L_x + 2\pi i k_z z/L_z} \tag{2.18}$$

Note that the splitting of the modes is applied in both translationally invariant directions of plane Couette flow, i.e. in streamwise x- and in spanwise z-direction. The respective thresholds κ_x and κ_z can be set independently and the streamwise quasilinear approximation is included as a particular limit, namely for $\kappa_x = 0, \kappa_z \to \infty$, as well as the full nonlinear system for $\kappa_x \to \infty, \kappa_z \to \infty$.

With the projections $\mathcal{P}_{\mathrm{I}}$ and $\mathcal{P}_{\mathrm{II}}$ onto the two subspaces from (2.17) and (2.18), the nonlinear term of the Navier-Stokes equation can be written as

$$\begin{aligned}(\vec{u}\,\nabla)\vec{u} + \nabla\tilde{p} = \quad & \mathcal{P}_{\mathrm{I}}(\vec{u}_{\mathrm{I}}\nabla)\vec{u}_{\mathrm{I}} + \mathcal{P}_{\mathrm{I}}(\vec{u}_{\mathrm{II}}\nabla)\vec{u}_{\mathrm{II}} + \underbrace{\mathcal{P}_{\mathrm{I}}(\vec{u}_{\mathrm{I}}\nabla)\vec{u}_{\mathrm{II}}}_{\mathrm{GQL}\Rightarrow=0} + \underbrace{\mathcal{P}_{\mathrm{I}}(\vec{u}_{\mathrm{II}}\nabla)\vec{u}_{\mathrm{I}}}_{\mathrm{GQL}\Rightarrow=0} \\ & + \underbrace{\mathcal{P}_{\mathrm{II}}(\vec{u}_{\mathrm{I}}\nabla)\vec{u}_{\mathrm{I}}}_{\mathrm{GQL}\Rightarrow=0} + \underbrace{\mathcal{P}_{\mathrm{II}}(\vec{u}_{\mathrm{II}}\nabla)\vec{u}_{\mathrm{II}}}_{\mathrm{GQL}\Rightarrow=0} + \mathcal{P}_{\mathrm{II}}(\vec{u}_{\mathrm{I}}\nabla)\vec{u}_{\mathrm{II}} + \mathcal{P}_{\mathrm{II}}(\vec{u}_{\mathrm{II}}\nabla)\vec{u}_{\mathrm{I}}.\end{aligned} \tag{2.19}$$

Within the generalized quasilinear approximation, four out of the eight projections are neglected such that the Navier-Stokes equations of $\vec{u}_{\mathrm{I}}$ and $\vec{u}_{\mathrm{II}}$ are of the same structure as for the streamwise quasilinear approximation, see (2.14) and (2.15). Interactions between low wavenumber modes (group I) and high wavenumber modes (group II) will be omitted for the dynamics of the low wavenumber modes $\vec{u}_{\mathrm{I}}$. For the dynamics of the high wavenumber modes $\vec{u}_{\mathrm{II}}$ all self-interactions between the low modes as well as between the high modes will be omitted. The diagrams in figure 2.5 vizualize the nonlinear interactions which are kept.

The generalized quasilinear approximation thus allows for a scattering of energy between different high wavenumber modes via interactions with the low wavenumber modes. The fully nonlinear system can be recovered by increasing the number of modes contained in the first group $\vec{u}_{\mathrm{I}}$. In chapter 6 we will examine the properties of exact coherent structures and their bifurcation diagrams for different choices of the thresholds κ_x and κ_z in comparison to the streamwise quasilinear approximation and the fully nonlinear system.

3 Direct and noisy transitions in a low-dimensional shear flow model

The results presented in this chapter have been published in *Direct and noisy transitions in a model shear flow*, Marina Pausch and Bruno Eckhardt, Theoretical and Applied Mechanics Letters 5 (2015).

3.1 Introduction

As discussed in the previous chapter, the transition to turbulence for many shear flows like plane Couette flow or pipe flow is not due to a linear instability of the laminar profile. The transition requires perturbations of sufficient amplitude which have to cross the boundary to the basin of attraction of the turbulent regime. From a dynamical systems point of view this boundary between the laminar and the tubulent regime is the stable manifold of the so-called edge state which is a saddle state that lies on this boundary and has only one unstable direction. Figure 3.1 shows the corresponding state space structure with the stable laminar profile which is divided from the turbulent regime by a boundary (red line). This boundary is the "edge of chaos", i.e. the stable manifold of the edge state. Initial conditions need to cross this boundary to be able to trigger turbulence. Previous studies of optimal perturbations involve time-integration of the systems (Pringle and Kerswell, 2010; Monokrousos et al., 2011; Pringle et al., 2012; Duguet et al., 2013; Cherubini and De Palma, 2013; Cherubini and Palma, 2014). We here do not regard transition times, but only focus on a geometric optimization. Since there are mechanisms in the systems that amplify small disturbances, the presence of thermodynamic fluctuations can be sufficient to trigger the transition to turbulence (Luchini, 2010; Sengers and Ortiz de Zárate, 2010; Ortiz de Zárate and Sengers, 2011, 2012; Luchini, 2017).

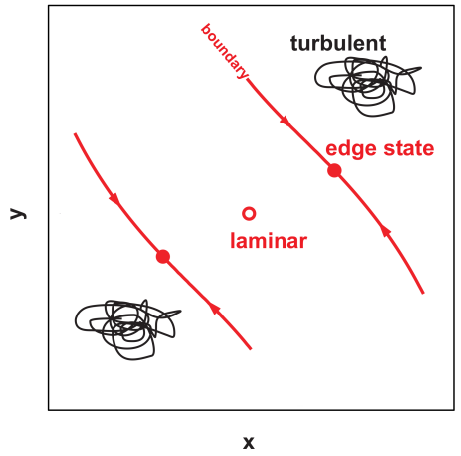

Figure 3.1: Sketch of state space for a linearly stable shear flow with the stable laminar state (open circle) and the turbulent states, divided by a boundary (red line).

In this chapter, "optimal" initial conditions that trigger turbulence are studied for two direct transition scenarios and for noise-induced transitions for a 2-dimensional model system which allows for a 2-d visualization of state space. The investigation of the optimal transition states and their scaling with Re can improve our understanding of the transition to turbulence and help to design control strategies.

3.2 The model

The 2-dimensional model investigated in this chapter is a rescaled version of a model from Baggett and Trefethen (1997):

$$\dot{x} = -x + Ry - y\sqrt{x^2 + y^2}/R \tag{3.1}$$

$$\dot{y} = -2y + x\sqrt{x^2 + y^2}/R \tag{3.2}$$

The model has two variables where x can be considered as the amplitude of streaks and y as the amplitude of vortices, respectively. The parameter R plays the role of the Reynolds number. The model has a non-normal linear part and an "energy"-conserving nonlinearity, i.e. if only the nonlinear terms are evolved in time the "energy" x^2+y^2 is preserved. It is based on the self-sustaining cycle found by Waleffe (1997): x is the streak that is driven by the decaying vortex y. For $R < R_c = \sqrt{8}$ there is only one fixed point of the model which is the stable "laminar" state in the origin $(0,0)$. At $R = R_c$ four other symmetry-related fixed points (x_c, y_c) and $(-x_c, -y_c)$ appear, with

$$x_c = R(2R \pm 2\sqrt{R^2-8})/D_\pm, \tag{3.3}$$

$$y_c = R(R^2-4 \pm R\sqrt{R^2-8})/D_\pm, \tag{3.4}$$

and $D_\pm = \sqrt{8+2R^2 \pm 2R\sqrt{R^2-8}}$. The advantage of such a 2-dimensional model is that the whole state space can easily be visualized, as shown in figure 3.2. There are the two unstable saddle states which lie closer to the origin and are marked with full symbols. They are the "edge states" of the system. The two stable node states lie further out in the region where turbulence would form if more degrees of freedom were available, so in the following they will be called the "turbulent" states. The red lines are the stable manifolds of the edge states and form the boundary between the laminar and the turbulent basin of attraction.

3.3 Optimal initial conditions for transition

An initial condition close to the laminar state will always decay. Increasing the distance from the laminar state, initial conditions that become turbulent will eventually appear. Different norms can be introduced to measure the distance to the laminar state for different criteria. The Euclidean norm $Q_E = 1/2(x^2+y^2)$ corresponds to the energy of the initial condition and its isocontours in state space are circles. The energy dissipation of the initial condition is given by $Q_\epsilon = 1/2(x^2+2y^2)$ and the corresponding isocontours are ellipses. Noise-driven transitions can be described by the isocontours of a probability density function, as will be explained in section 3.3.4. In the following, optimal perturbations for

the 2-d model will be found with respect to the three different criteria.

The black circle in figure 3.2 shows the optimal transition state obtained for the energy of the initial condition at $R = 3$. Geometrically, it is the biggest circle that can be drawn around the laminar state that just touches the stable manifold of the edge state, because it contains one initial condition - the one on the edge - that does not decay to the laminar state. Other optimization criteria, the energy dissipation norm and the noise norm, have ellipsoidal isocontours as examplarily shown in grey for the noise norm.

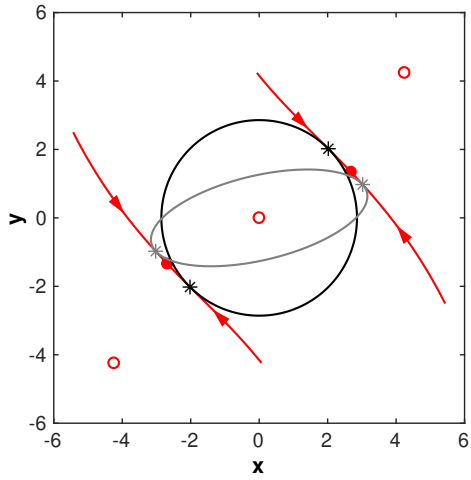

Figure 3.2: State space of the 2-d model for the transition to turbulence for $R = 3$. The stable and unstable fixed points are marked by open and full symbols, respectively. The stable fixed point at the origin is called the "laminar" state and the two nodes from the bifurcation are called "turbulent" states. The two saddle states are the "edge states", and the red lines indicate their stable manifolds. The black circle and the grey ellipsoid indicate the states where the energy norm (3.6) and the noise norm (3.11) are minimal, respectively. Stars mark the points where they touch the stable manifolds.

3.3.1 Modified edge tracking algorithm

An optimal transition state corresponds to the maximal value of the respective functional up to which all initial conditions return to the laminar state and for

slightly larger values the first initial conditions will become turbulent. These optimal states are found by a modified edge-tracking algorithm which optimizes the respective quadratic functional $Q_X(x,y) = \vec{x}^T Q \vec{x}$. This functional can be the energy Q_E, the energy dissipation Q_ϵ or the noise norm Q_N, which are given in equations (3.6), (3.7) and (3.11), respectively.

An arbitrary initial condition in the vicinity of the edge is brought onto the edge by edge tracking. Typically this is done by integrating the trajectories until they are sufficiently close to either the laminar or the turbulent state. Here the time-evolution of the trajectory towards the edge state is stopped at the time with minimal distance to it, i.e. when the trajectory turns towards the laminar or the turbulent state. The velocity at this point then is projected onto the normal of the stable eigenvector. This projection provides information on whether the tested initial condition is going to move upwards towards the turbulent state or downwards to become laminar. This criterion allows to find a point $\vec{x}_0$ on the edge also when the point is already very close to the edge and the time to pass the edge state becomes very large.

The point $\vec{x}_0$ on the edge is then propagated along the time direction $\vec{x}_1 = \vec{x}_0 + s\vec{f}(\vec{x}_0)$ where $\dot{\vec{x}} = \vec{f}(\vec{x})$ denotes the equations of motion. The parameter s is chosen in such a way that the functional $Q(s)$ is minimized:

$$s = -\frac{\vec{f}^T(\vec{x}_0) Q \vec{x}_0 + \vec{x}_0^T Q \vec{f}(\vec{x}_0)}{2\vec{f}^T(\vec{x}_0) Q \vec{f}(\vec{x}_0)} \tag{3.5}$$

It is ensured that the norm of the shift $\|s\vec{f}\|$ is kept below a certain threshold to allow for linear approximations. The new point $\vec{x}_1$ is then again used as initial condition for an edge tracking and the whole process is repeated until $\|s\vec{f}\|$ falls below a convergence threshold, here 10^{-5}.

3.3.2 Initial conditions of minimal energy

The optimals found for the energy norm

$$Q_E = \frac{1}{2}(x^2 + y^2) \tag{3.6}$$

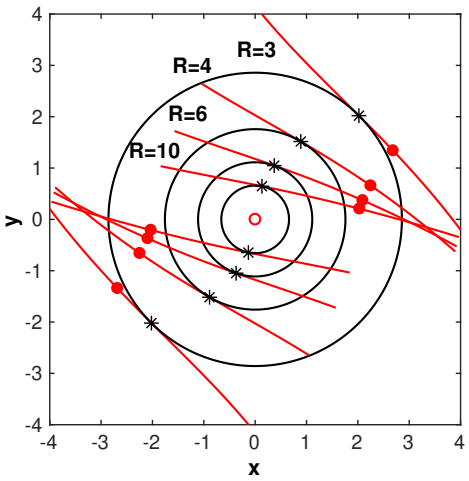

Figure 3.3: Optimal states in energy norm for different R. The isocontours of the energy are indicated by the black circles. Stars mark the points where they touch the stable manifolds of the edge states (indicated as red lines and full symbols). The laminar state is the open symbol in the origin.

are plotted in figure 3.3. The black circles are states of fixed energy and they correspond to parameter values of $R = 3, 4, 6$ and 10 from the outer to the inner circle. The full red symbols are the edge states with their stable manifolds shown as red lines. With increasing Reynolds number the edge states approach the x-axis and their stable manifolds rotate so as to become parallel to the x-axis, while the turbulent states move further out and are not shown in the plot. The optimal state is the maximal circle that just touches the stable manifold of the edge state. All initial conditions with an energy that is smaller than this optimal one will decay to the laminar profile. For slightly larger energies the first initial conditions become turbulent. The optimal transition states in energy norm for the different values of R are marked with black stars. Because of the rotation of the stable manifolds, the point of contact with the circles of equal energy moves away from the edge state and approaches the y-axis. This means that the optimal perturbation becomes more vortex-like as the streak component decreases.

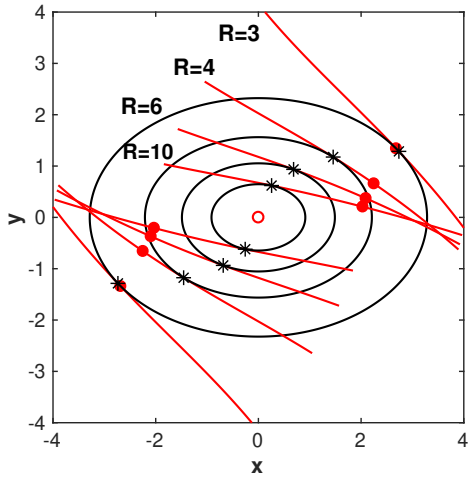

Figure 3.4: Optimal states in dissipation norm for different R as in figure 3.3. The isocontours of the energy dissipation are indicated by the black ellipses.

3.3.3 Initial conditions of minimal energy dissipation

The functional for the energy dissipation is defined as

$$Q_\epsilon = \frac{1}{2}(x^2 + 2y^2) \tag{3.7}$$

as the diagonal terms in the linear part of the equations of motion correspond to the dissipation in the original Navier-Stokes equation. Finding initial conditions which are minimal with respect to this functional geometrically means to find the point where an ellipse touches the stable manifold.

The ellipses and transition points for different values of R are shown in figure 3.4. The comparison with the points of contact found for the energy functional shows that the points are different, but move in a similar manner in both cases.

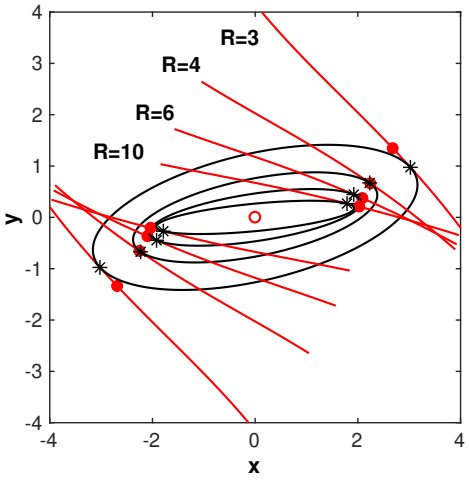

Figure 3.5: Optimal states for the noise norm for different R. The black ellipsoids show the iso-contours of the probability density function. With increasing R they become narrower in the y-direction and stretch out along the x-direction. In combination with the rotation of the stable manifolds (red lines) the point of contact (stars) now stays close to the edge state (full symbols) and moves towards the x-axis. This is physically plausible, as a small perturbation in y (in the vortex direction) will produce a strong streak in the x-direction, and it is then the streak that triggers the transition.

3.3.4 Optimal noisy transitions

To study transitions which are driven by noise, a stochastic forcing is added to the equations of motion:

$$\dot{x} = -x + Ry - y\sqrt{x^2+y^2}/R + \xi_x \tag{3.8}$$

$$\dot{y} = -2y + x\sqrt{x^2+y^2}/R + \xi_y \tag{3.9}$$

with $\langle \xi_i(t) \rangle = 0$ and $\langle \xi_i(t)\xi_j(t') \rangle = D_{ij}\delta_{i,j}\delta(t-t')$ for Gaussian white noise. Here $D_{11} = D_{22} = D$ is chosen, i.e. both components are driven with equal noise amplitude.

A Gaussian probability density function for the two components is obtained in a linear approximation around the laminar fixed point as described in Eckhardt

et al. (1998),

$$p(x, y) \sim \exp(-\vec{x}^T Q \vec{x}/D) \tag{3.10}$$

with the noise norm

$$\begin{aligned} Q_N(x, y) &= \vec{x}^T Q \vec{x} \\ &= \frac{3}{2(R^2+9)}(3x^2 - 2Rxy + (R^2+6)y^2). \end{aligned} \tag{3.11}$$

Unlike the previously discussed energy and dissipation functionals, the noise functional depends on the Reynolds number. The iso-contours $p = const$ of the probability density are ellipsoids given by this norm and they shrink or increase with the noise amplitude D like $Q_N \sim -\ln(p)D$. Increasing D thus increases the chance of a transition to the turbulent state. The aim is to find the point where a trajectory most likely enters the basin of attraction of the turbulent state due to noise-induced fluctuations. This point is obtained as the point of contact between the ellipsoidal iso-contours and the stable manifold of the edge state.

The optimals for different values of the parameter R are shown in figure 3.5. With increasing value of the parameter R the ellipsoids become more elongated in x-direction and they are rotated into the opposite direction as the stable manifolds of the edge states, so that the point of contact always stays close to the edge state. This is different to the two previously studied cases and means that the noise-induced transition is always dominated by the streak.

Figure 3.6 shows the probability density of the trajectory to be at point (x, y) for $R = 6$ in the part of state space where the transition is expected to occur. The calculated optimal transition point is indicated by a star. 20000 initial conditions which start at the laminar state have been evolved in time for 20 time units with a step size of $dt = 10^{-3}$. The trajectories have been integrated with an explicit Euler method. The noise amplitude D has been chosen such that in the linearized case a trajectory spends 5% of the time outside of the optimal ellipsoid, indicated in white. We mirror trajectories from the third quadrant of the state space to the first quadrant, because the state space is symmetric to the origin. The upper figure is obtained from a calculation without the

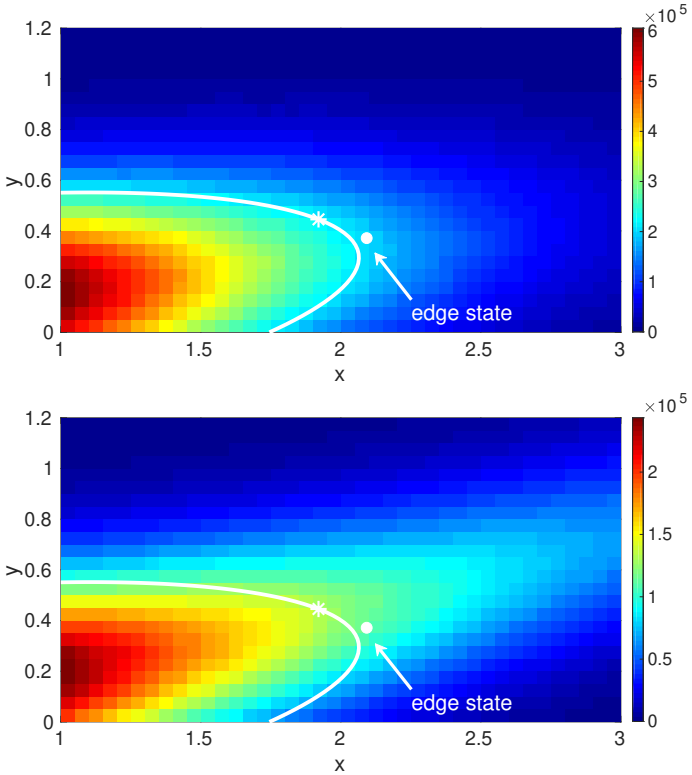

Figure 3.6: Top: Probability density of the trajectory to be at (x, y) for the linearized equations with noise for $R = 6$. Shown is the region of phase space where the transition is expected to occur. The time evolution of 20000 initial conditions has been calculated which start at the laminar state and evolve for 20 time units with a step size of $dt = 10^{-3}$. It can be seen that the iso-contours $p = const$ are of elliptical shape. The star indicates the point where the noise norm touches the stable manifold of the edge state. Bottom: Probability density as in the top panel, but for the full nonlinear equations with noise. Note that the iso-contours of equal probability are stretched out towards the turbulent state and that they cross the stable manifold close to the point of contact indicated as the optimal state.

nonlinear part and shows the ellipsoidal shape of the iso-contours. The bottom figure is obtained from a calculation with the nonlinear part and it can be seen that the probability density function stretches out along the path towards the turbulent state. It leaks out of the basin of attraction of the laminar profile so that trajectories can cross over and become turbulent. Note that the transition happens close to the calculated touching point between the ellipsoid and the stable manifold of the edge state, indicated as a star in both figures.

3.4 Comparison and conclusions

The differences in the selected optimal initial conditions by the three different criteria becomes clear if the points of transition are compared. In figure 3.7 the edge state is indicated in red and the points of contact for the energy, the energy dissipation and the noise norm are shown in blue, magenta and green, respectively. In the deterministic cases for the energy and the energy dissipation, the optimal transition states approach the origin along the y-axis while in the noisy case the optimal states do not move towards the origin, but towards the x-axis.

Within the hydrodynamic interpretation the optimal initial conditions for the energy and the dissipation norm are more vortex-like, while the optimal perturbations for the noisy case with a stochastic forcing are more streak-like and remain close to the edge state with increasing value of R. In the direct transition scenarios with optimal energy or energy dissipation, the optimal states are vortices which lead to the evolution of streaks and can be amplified by non-normal amplification via the self-sustaining process to trigger a transition to turbulence, in agreement with the description in section 2.2.1 and the references therein. The critical amplitudes of the optimal perturbations decrease with increasing R like $1/R^2$ in both cases as shown in figure 3.8. This reflects that shear flows become more susceptible to disturbances with increasing Reynolds number, and hence with increasing flow rate.

Flows in the presence of noise may show different structures at the transition point, because the existing disturbances can grow to develop streaks and the probability density function then stretches out along the streak direction due to

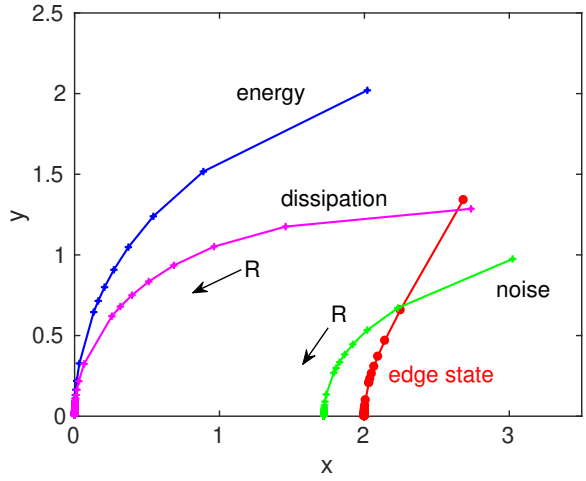

Figure 3.7: Location of the points of contact and the edge state. The optimal transition points for the energy and the energy dissipation are shown in blue and magenta, respectively. They are vortex-like and approach the origin along the y-axis with increasing R. The optimal points for noise-induced transitions (green) are streak-like and move towards the x-axis. The edge state approaches $(2, 0)$ as $R \to \infty$ (red dots).

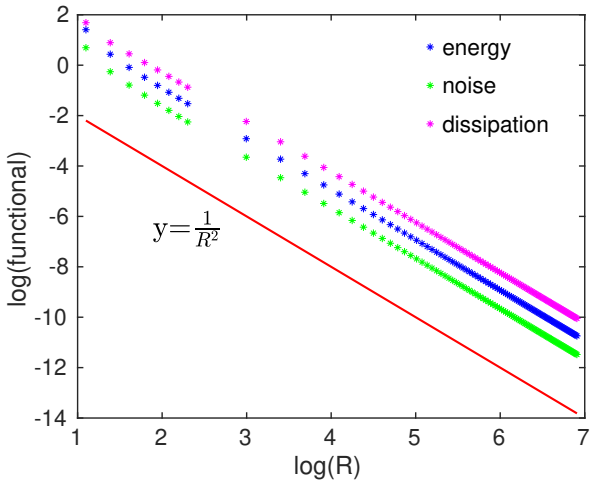

Figure 3.8: Scaling of the norms of the optimal perturbations for the energy (blue), the energy dissipation (magenta) and for noise-induced transitions (green). In all three cases, the critical amplitudes decay like $1/R^2$. A reference line is shown in red.

non-normal amplification. The transition then happens on top of these existing streaks. In the noisy case, a small perturbation in the vortex direction y will produce a strong streak which triggers the transition. Despite the differences the scaling with R is the same as in the other two cases, see figure 3.8. The critical amplitudes all decay like $1/R^2$. Similar phenomena can be expected for plane Couette flow and related shear flows.

4 Shear flow models with quasilinear structure

4.1 Introduction

The investigation of simplified models has led to a better understanding of the transition to turbulence in linearly stable shear flows. The quasilinear approximation as described in section 2.3.1 consists of a decomposition of the velocity field into one part which is invariant in downstream direction (with components u_I) and another part with streamwise variations (components u_i). For the streamwise varying components only those nonlinear interactions are kept which result in streamwise invariant fields; the other nonlinear interactions are dropped. As explained in section 2.3.1, this decomposition results in two sets of equations, (2.14) and (2.15), which have the following structure:

$$\partial_t u_I = \mathcal{N}(u_I, u_J) + \mathcal{R}(u_i, u_j) \tag{4.1}$$

for the streamwise invariant modes u_I, u_J of group I and

$$\partial_t u_i = \mathcal{L}_{ij}(u_I) u_j \tag{4.2}$$

for the group II modes u_i, u_j with variation in streamwise direction. In the equations of the first group, $\mathcal{N}(u_I, u_J)$ denotes the nonlinear interactions between the streamwise invariant modes and $\mathcal{R}(u_i, u_j)$ denotes the Reynolds stresses arising from the nonlinear interactions between the streamwise varying modes. The equations of the second group are quasilinear as they are linear in u_i and do not contain self-interactions within the group II modes, but the u_i are parametrically coupled to the modes of group I via $\mathcal{L}_{ij}(u_I)$.

Several low-dimensional models including the four and eight dimensional models by Waleffe (1997) and the 9-mode model by Moehlis et al. (2004, 2005) have

such a quasilinear structure by construction, without further approximation. In this chapter we will investigate properties of such quasilinear models.

4.2 Waleffe's 4d model

The four mode model of Waleffe (1997) is a model of the self-sustaining process and it consists of four amplitude equations:

$$\frac{d}{dt}M = -\frac{\kappa_M^2}{Re}M - \sigma_S V S + \frac{\kappa_M^2}{Re} + \sigma_M L^2 \tag{4.3}$$

$$\frac{d}{dt}S = -\frac{\kappa_S^2}{Re}S + \sigma_S M V - \sigma_L L^2 \tag{4.4}$$

$$\frac{d}{dt}V = -\frac{\kappa_V^2}{Re}V + \sigma_V L^2 \tag{4.5}$$

$$\frac{d}{dt}L = \underbrace{-\Big(\frac{\kappa_L^2}{Re} + \sigma_M M - \sigma_L S + \sigma_V V\Big)}_{=Q(M,S,V)} L \tag{4.6}$$

where M corresponds to the mean flow, S to the streak, V to the vortex, and L denotes the mode with longitudinal variation. Some variables have been renamed compared to the original equations to clarify these relations. The κ's and σ's are damping and coupling constants, respectively, and Re is the Reynolds number.

The first equation contains the forcing, in a term that drives the mean profile κ_M^2/Re; all equations contain damping terms as well as terms with quadratic couplings between the modes. With regard to the structure shown at the beginning of this chapter, M, S and V belong to the set of modes u_I which are streamwise invariant and L belongs to the group u_i. The model has a quasilinear structure without further approximation: The equation for L is quasilinear by construction and the term in brackets $Q(M, S, V)$ corresponds to the matrix $\mathcal{L}(u_I)$ of equation (4.2).

For a fixed point $\vec{u}_{FP} = (M_{FP}, S_{FP}, V_{FP}, L_{FP})$ of the system all time derivatives vanish, i.e. $d\vec{u}/dt = \vec{0}$. For equation (4.6) there are two possible solutions: either $L = 0$ or $Q(M, S, V) = 0$. The first case leads to the trivial solution as for $L = 0$ the vortex V decays and with it the streak S and the system becomes

laminar. Hence, the requirement for the existence of non-trivial fixed points is that $Q(M,S,V)=0$. Then only L is free and can act back onto the equations of group I via Reynolds stresses and thereby determine the solutions in set I such that non-trivial fixed points can exist. Note that $Q=0$ represents marginal stability of $\mathcal{L}(u_I)$.

Figure 4.1 illustrates this marginal stability condition of $Q(M,S,V)$. The chosen parameter values are $\alpha=1.49$, $\beta=\pi/2$ and $\gamma=1.82$, which determine the κ's and σ's to $\kappa_M^2\approx 2.47$, $\kappa_S^2\approx 3.31$, $\kappa_V^2\approx 5.78$, $\kappa_L^2\approx 5.66$, $\sigma_M\approx 0.24$, $\sigma_S\approx 1.19$, $\sigma_V\approx 0.10$ and $\sigma_L\approx 0.33$ (see (Waleffe, 1997) for the relations). The model then has two non-trivial fixed points which appear in a saddle-node bifurcation at $Re_c=137.17$.

We put $L=\lambda L_*$ with $L_*=L(u_{FP})$ at $Re=Re_c$ such that the Reynolds stresses in the equations for M,S and V become $\sim\lambda^2L_*^2$. The fixed point values of M,S and V and hence $Q(M,S,V)$ then can be calculated in dependence of λ: setting dV/dt (equation (4.5)) to zero gives

$$V(\lambda)=\frac{Re}{\kappa_V^2}\sigma_V\lambda^2L_*^2. \tag{4.7}$$

$M(\lambda)$ and $S(\lambda)$ then follow from $dM/dt=0$ and $dS/dt=0$ (equations (4.3) and (4.4)):

$$S(\lambda)=\frac{\Big(-\frac{Re}{\kappa_S^2}\sigma_L+\frac{Re^2}{\kappa_S^2\kappa_V^2}\Big)\sigma_S\sigma_V\lambda^2L_*^2+\frac{Re^3}{\kappa_S^2\kappa_V^2\kappa_M^2}\sigma_S\sigma_V\sigma_M\lambda^4L_*^4}{1+\frac{Re^4}{\kappa_S^2\kappa_M^2\kappa_V^4}\sigma_S^2\sigma_V^2\lambda^4L_*^4} \tag{4.8}$$

$$M(\lambda)=1+\Big(\frac{Re}{\kappa_M^2}\sigma_M-\frac{Re^2}{\kappa_M^2\kappa_V^2}\sigma_S\sigma_V S(\lambda)\Big)\lambda^2L_*^2 \tag{4.9}$$

Figure 4.1 shows

$$Q(\lambda)=-(\kappa_L^2/Re+\sigma_M M(\lambda)-\sigma_L S(\lambda)+\sigma_V V(\lambda)) \tag{4.10}$$

from equation (4.6) in dependence of λ for different values of the Reynolds number. For $Re=Re_c$ only one solution $Q=0$ exists, which corresponds to the fixed point at the bifurcation with $\lambda=1$, as expected. For smaller values of

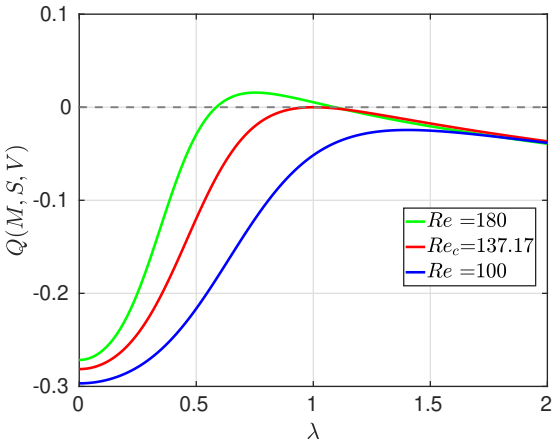

Figure 4.1: Illustration of the marginal stability condition for Waleffe's 4d model. The model has two nontrivial fixed points that appear in a saddle-node bifurcation at $Re_c = 137.17$ (red line) corresponding to $Q = 0$. For $Re > Re_c$ there are two solutions $Q = 0$ which belong to the upper and lower branch states (green line). For $Re < Re_c$ no nontrivial fixed points exist and hence there is no solution with $Q = 0$ (blue line).

Re there is no fixed point of the system and accordingly no value of λ for which $Q = 0$. For $Re > Re_c$ there exist two solutions $Q = 0$, corresponding to the upper and lower branch fixed points of the system. The existence of a nontrivial fixed point $\vec{u}_{FP}$ with $\partial_t \vec{u}_{FP} = 0$ requires that $Q(u_{I,FP}) = 0$.

4.3 The 9-mode model

The 9-mode shear flow model has been derived by Moehlis et al. (2004, 2005) and describes a sinusoidal shear flow of an incompressible fluid between two free-slip walls. The model comprises nine modes $u_l(x, y, z)$ describing the laminar profile, its modification, streaks, vortices, spanwise flows and couplings:

$$\vec{u}(x, y, z, t) = \sum_{l=1}^{9} a_l(t)\vec{u}_l(x, y, z) \tag{4.11}$$

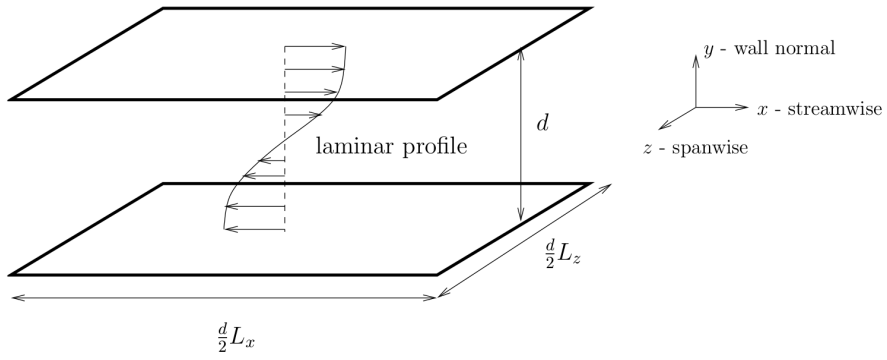

Figure 4.2: (Reprinted from Moehlis et al. (2005) with permission of SIAM.) Geometry of the sinusoidal shear flow.

with the amplitudes $a_l(t)$ and x, y, and z denoting the streamwise, wall-normal and spanwise direction, respectively, see figure 4.2. The fluid is incompressible and the flow is periodic with length L_x in the streamwise and with length L_z in the spanwise direction. The walls are located at $y = \pm 1$. The corresponding nine amplitude equations are of the form:

$$\dot{a_l} = \frac{\beta^2}{Re}\delta_{l,1} - \frac{d_l}{Re}a_l + \sum_{m,n} N_{l,mn}a_m a_n \tag{4.12}$$

The first term captures that only the first mode, i.e. the laminar profile, is driven. The second term represents the viscous damping of the modes, the $N_{l,mn}$ represent the nonlinear couplings and Re is the Reynolds number.

4.3.1 Separation of modes

The 9-mode model naturally has a quasilinear structure. The streamwise invariant modes (group I) are modes 1 and 9 (the base flow and its modification), mode 2 (streak) and mode 3 (downstream vortex). The modes with variation in downstream direction (group II) are modes 4 and 5 (spanwise flows), 6 and 7 (normal vortices) and 8 (mixing mode). The exact representation of the modes can be found in (Moehlis et al., 2004, 2005).

The corresponding nine amplitude equations naturally separate into two qual-

itatively different sets of equations for group I and group II.

The amplitude equations for group I (with modes 1,2,3 and 9) are

$$\dot{a}_1 = \frac{\beta^2}{Re} - \frac{\beta^2}{Re}a_1 - \sqrt{\frac{3}{2}}\frac{\beta\gamma}{\kappa_{\alpha\beta\gamma}}a_6a_8 + \sqrt{\frac{3}{2}}\frac{\beta\gamma}{\kappa_{\beta\gamma}}a_2a_3, \tag{4.13}$$

$$\dot{a}_2 = -\left(\frac{4\beta^2}{3} + \gamma^2\right)\frac{a_2}{Re} + \frac{5\sqrt{2}}{3\sqrt{3}}\frac{\gamma^2}{\kappa_{\alpha\gamma}}a_4a_6 - \frac{\gamma^2}{\sqrt{6}\kappa_{\alpha\gamma}}a_5a_7 - \frac{\alpha\beta\gamma}{\sqrt{6}\kappa_{\alpha\gamma}\kappa_{\alpha\beta\gamma}}a_5a_8 - \sqrt{\frac{3}{2}}\frac{\beta\gamma}{\kappa_{\beta\gamma}}(a_1a_3 - a_3a_9), \tag{4.14}$$

$$\dot{a}_3 = -\frac{\beta^2+\gamma^2}{Re}a_3 + \frac{\beta^2(3\alpha^2+\gamma^2) - 3\gamma^2(\alpha^2+\gamma^2)}{\sqrt{6}\kappa_{\alpha\gamma}\kappa_{\beta\gamma}\kappa_{\alpha\beta\gamma}}a_4a_8 + \frac{2}{\sqrt{6}}\frac{\alpha\beta\gamma}{\kappa_{\alpha\gamma}\kappa_{\beta\gamma}}(a_4a_7 + a_5a_6), \tag{4.15}$$

$$\dot{a}_9 = -\frac{9\beta^2}{Re}a_9 - \sqrt{\frac{3}{2}}\frac{\beta\gamma}{\kappa_{\alpha\beta\gamma}}a_6a_8 + \sqrt{\frac{3}{2}}\frac{\beta\gamma}{\kappa_{\beta\gamma}}a_2a_3, \tag{4.16}$$

where $\kappa_{\alpha\gamma} = \sqrt{\alpha^2+\gamma^2}$, $\kappa_{\beta\gamma} = \sqrt{\beta^2+\gamma^2}$ and $\kappa_{\alpha\beta\gamma} = \sqrt{\alpha^2+\beta^2+\gamma^2}$, and $\alpha = 2\pi/L_x$, $\beta = \pi/2$ and $\gamma = 2\pi/L_z$. The equations have the structure shown in (4.1) without further approximation. There are nonlinear couplings between modes of group I as well as Reynolds stresses from couplings between modes of group II, but no interactions between the modes of the two groups.

The amplitude equations for group II (with modes 4,5,6,7 and 8) are

$$\dot{a}_4 = -\frac{3\alpha^2+4\beta^2}{3Re}a_4 - \frac{\alpha}{\sqrt{6}}(a_1a_5 + a_5a_9) - \frac{10}{3\sqrt{6}}\frac{\alpha^2}{\kappa_{\alpha\gamma}}a_2a_6 - \sqrt{\frac{3}{2}}\frac{\alpha\beta\gamma}{\kappa_{\alpha\gamma}\kappa_{\beta\gamma}}a_3a_7 - \sqrt{\frac{3}{2}}\frac{\alpha^2\beta^2}{\kappa_{\alpha\gamma}\kappa_{\beta\gamma}\kappa_{\alpha\beta\gamma}}a_3a_8 \tag{4.17}$$

$$\dot{a}_5 = -\frac{\alpha^2+\beta^2}{Re}a_5 + \frac{\alpha}{\sqrt{6}}(a_1a_4 + a_4a_9) + \frac{\alpha^2}{\sqrt{6}\kappa_{\alpha\gamma}}a_2a_7 - \frac{\alpha\beta\gamma}{\sqrt{6}\kappa_{\alpha\gamma}\kappa_{\alpha\beta\gamma}}a_2a_8 + \frac{2}{\sqrt{6}}\frac{\alpha\beta\gamma}{\kappa_{\alpha\gamma}\kappa_{\beta\gamma}}a_3a_6, \tag{4.18}$$

$$\dot{a}_6 = -\frac{3\alpha^2+4\beta^2+3\gamma^2}{3Re}a_6 + \frac{10}{3\sqrt{6}}\frac{\alpha^2-\gamma^2}{\kappa_{\alpha\gamma}}a_2a_4 - 2\sqrt{\frac{2}{3}}\frac{\alpha\beta\gamma}{\kappa_{\alpha\gamma}\kappa_{\beta\gamma}}a_3a_5 + \frac{\alpha}{\sqrt{6}}(a_1a_7 + a_7a_9) + \sqrt{\frac{3}{2}}\frac{\beta\gamma}{\kappa_{\alpha\beta\gamma}}(a_1a_8 + a_8a_9), \tag{4.19}$$

$$\dot{a}_7 = -\frac{\alpha^2+\beta^2+\gamma^2}{Re}a_7 - \frac{\alpha}{\sqrt{6}}(a_1a_6 + a_6a_9) + \frac{1}{\sqrt{6}}\frac{\gamma^2-\alpha^2}{\kappa_{\alpha\gamma}}a_2a_5 + \frac{1}{\sqrt{6}}\frac{\alpha\beta\gamma}{\kappa_{\alpha\gamma}\kappa_{\beta\gamma}}a_3a_4, \tag{4.20}$$

$$\dot{a}_8 = -\frac{\alpha^2+\beta^2+\gamma^2}{Re}a_8 + \frac{2}{\sqrt{6}}\frac{\alpha\beta\gamma}{\kappa_{\alpha\gamma}\kappa_{\alpha\beta\gamma}}a_2a_5 + \frac{\gamma^2(3\alpha^2-\beta^2+3\gamma^2)}{\sqrt{6}\kappa_{\alpha\gamma}\kappa_{\beta\gamma}\kappa_{\alpha\beta\gamma}}a_3a_4 \tag{4.21}$$

and they are of the form of equation (4.2). These equations are quasilinear in the group II modes as there are only couplings between modes of group I and modes of group II and no couplings within group II.

In the following, the amplitudes of group I and group II will be labeled with subscripts I, J and i, j, respectively, consistent with equations (4.1) and (4.2). At a fixed point of the system all time derivatives vanish, i.e. $\dot{a}_I = 0$ and $\dot{a}_i = 0$. There exist two possibilies for solutions of the quasilinear equations $\dot{a}_i = \mathcal{L}_{ij}(a_I)a_j = 0$. If $a_j = 0$, the nonlinear couplings $\mathcal{R}(a_i, a_j)$ in the amplitude equations of group I vanish. As a consequence, the equation for the downstream vortex mode a_3 is of the form $\dot{a}_3 = -\frac{d_3}{Re}a_3$ and thus the downstream vortex is bound to decay. This also leads to the decay of the streak a_2 and ultimately the laminar profile is obtained (trivial solution with $a_1 = 1$ and $a_2 = \ldots = a_9 = 0$). If $a_j \neq 0$, nontrivial stationary solutions require amplitudes a_I such that the matrix $\mathcal{L}_{ij}(a_I)$ has an eigenvalue $\Lambda = 0$. Then only the a_i are free and the corresponding neutral eigenvector can act back onto the equations of group I via the couplings between the a_i. These Reynolds stresses $\mathcal{R}(a_i, a_j)$ then self-consistently determine the fixed point values of group I such that nontrivial solutions can exist. This explanation is valid for all models which have a quasilinear structure as described above.

4.3.2 Fixed points

The fixed points of the nine mode model for the domain with $L_x = 4\pi$ and $L_z = 2\pi$ (NBC domain) are known from numerical computations (Moehlis et al., 2005) and have been confirmed by a Groebner basis approach (Pausch et al., 2014). In particular, it has been shown that all existing fixed points have been found. This makes the nine mode model an ideal framework in which to study

r	1	2	3	4	
$a_{9,r}$	-	-	-	-	0.089735712302478
$a_{8,r}$	+	-	+	-	0.063145095419022
$a_{7,r}$	-	+	-	+	0.179527330436095
$a_{6,r}$	+	-	+	-	0.106357125449557
$a_{5,r}$	+	+	-	-	0.035660223181101
$a_{4,r}$	+	+	-	-	0.016820147510723
$a_{3,r}$	+	-	-	+	0.034546810931729
$a_{2,r}$	+	-	-	+	0.048172536068084
$a_{1,r}$	+	+	+	+	0.192378589277698

r	5	6	7	8	
$a_{9,r}$	-	-	-	-	0.076441638712620
$a_{8,r}$	+	-	+	-	0.073427703733148
$a_{7,r}$	-	+	-	+	0.299006893267837
$a_{6,r}$	+	-	+	-	0.071244931925345
$a_{5,r}$	+	+	-	-	0.077141213856470
$a_{4,r}$	+	+	-	-	0.015756853890238
$a_{3,r}$	+	-	-	+	0.035586633113838
$a_{2,r}$	+	-	-	+	0.026548639723050
$a_{1,r}$	+	+	+	+	0.312025251586419

Table 4.1: The eight fixed points of the amplitude equations of the 9-mode model at $Re = 400$. A fixed point is the combination of one column of signs and a column of values.

ideas about the properties of quasilinear systems.

The nontrivial fixed points appear in a saddle-node bifurcation at $Re_c = 308.16$. For $Re < Re_c$ no fixed points exist besides the laminar profile. For $Re > Re_c$ there are two sets of fixed points, each of which contains four symmetry-related solutions, as shown in table 4.1 for $Re = 400$.

Figure 4.3 shows the variation of the real parts of the eigenvalues Λ_i of $\mathcal{L}_{ij}(a_{I,FP})$ for the upper and lower branch fixed point with Re. At the fixed points the matrix has one neutral eigenvalue $\Lambda_0 = 0$ for all Re, as expected from the above discussion. In addition, there is one positive complex pair and one negative complex pair of eigenvalues. The existence of a neutral eigenvalue of the quasilinear subsystem at the fixed points represents the marginal stability condition which is inherent in quasilinear systems. However, in this specific model there also exist positive eigenvalues of the subsystem $\mathcal{L}_{ij}(a_{I,FP})$.

On the other hand, the real eigenvalue Λ_0 of the matrix $\mathcal{L}_{ij}(a_I)$ is neutral only at the fixed points of the system. Figure 4.4 shows the visualization of the saddle-node bifurcation of the fixed points in the quasilinear subsystem. We

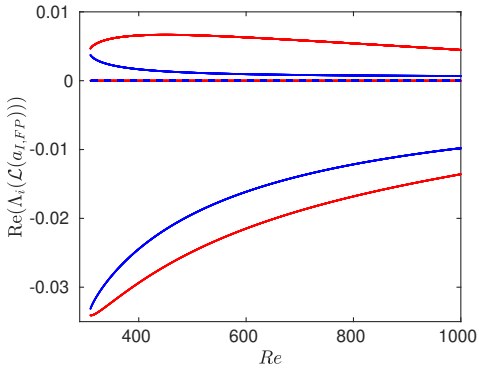

Figure 4.3: Variation of the real parts of the eigenvalues of $\mathcal{L}_{ij}(a_{I,FP})$ with the Reynolds number for the two fixed points of the 9 mode model. The eigenvalues for the lower branch fixed point $\vec{a}_{FP1}$ and for the upper branch fixed point $\vec{a}_{FP5}$ are shown in red and blue, respectively. Both fixed points have a positive and a negative complex pair of eigenvalues and a real neutral eigenvalue for all Re.

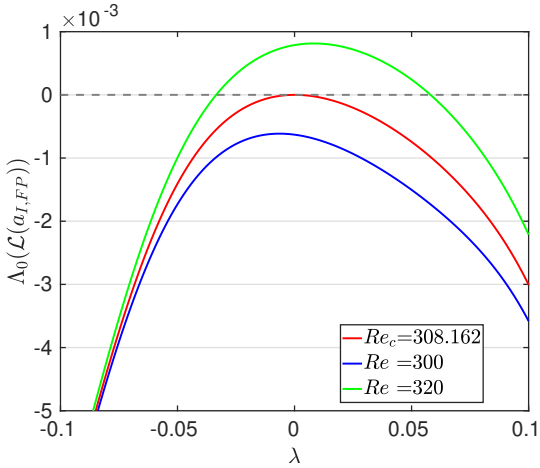

Figure 4.4: Bifurcation diagram in eigenspace of $\mathcal{L}_{ij}(a_I)$. For $Re = Re_c$ there exists one solution with a neutral eigenvalue corresponding to the single fixed point at the bifurcation point. For $Re < Re_c$ no nontrivial fixed points of the system exist and thus no solutions $\mathcal{L}_{ij}(a_I(\lambda)) = 0$. For $Re > Re_c$ the parabola crosses the x-axis and the two intersection points belong to the lower and the upper branch fixed points.

start with the fixed point values of the group II modes $\vec{a}_{\mathrm{II},FP}(Re_c)$ at the saddle-node bifurcation and vary this vector in the direction in which the saddle and the node state separate after the bifurcation:

$$\vec{a}_{\mathrm{II}}(\lambda) = \vec{a}_{\mathrm{II},FP}(Re_c) + \lambda \vec{t_c} \tag{4.22}$$

with

$$\vec{t_c} = \frac{\vec{a}_{\mathrm{II}}^{(saddle)}(Re_c^+) - \vec{a}_{\mathrm{II}}^{(node)}(Re_c^+)}{|\vec{a}_{\mathrm{II}}^{(saddle)}(Re_c^+) - \vec{a}_{\mathrm{II}}^{(node)}(Re_c^+)|}, \tag{4.23}$$

where the parameter λ is varied from -0.1 to 0.1 and the tangent $\vec{t_c}$ at the bifurcation point is approximated by the difference of the two fixed points slightly above the bifurcation point, i.e. for Re_c^+. For the Reynolds stresses $\mathcal{R}(a_i(\lambda), a_j(\lambda))$ obtained from $\vec{a}_{\mathrm{II}}(\lambda)$, we calculate the solutions of the fixed point equations for group I, $\dot{a}_I = 0$, which now depend on λ and the chosen Re. We insert the solutions $a_I(\lambda)$ into $\mathcal{L}_{ij}(a_I)$ and calculate the eigenvalues of the quasilinear subsystem. Their variation with λ is shown in figure 4.4 for three different Reynolds numbers: $Re = 300$ (below the bifurcation), $Re_c = 308.162$ (at the bifurcation) and $Re = 320$ (above the bifurcation).

For $Re < Re_c$ there is no neutral eigenvalue of $\mathcal{L}_{ij}(a_I(\lambda))$ as no fixed points of the system exist. At the bifurcation point $Re = Re_c$ the parabola touches the x-axis and there exists one solution with a neutral eigenvalue which corresponds to the single fixed point that just emerged. For larger Re the parabola intersects the x-axis and the resulting two neutral eigenvalues correspond to the lower and the upper branch fixed points, respectively.

4.3.3 Finding fixed points using zero eigenvalue condition

The condition that the real eigenvalue of $\mathcal{L}_{ij}(a_I)$ has to be zero at the fixed point can be used to determine the fixed points of the system. The corresponding neutral eigenmode then induces the Reynolds stresses $\mathcal{R}(a_i, a_j)$ in the equations of group I, which determine the fixed point of set I. This self-consistency can be used to find the fixed points of the system, i.e. the solutions of $\dot{\vec{a}}_{FP} = f(\vec{a}_{FP}) = 0$, in an iterative procedure.

Starting with a random initial condition for $\vec{a}_{\mathrm{I}} = (a_1, a_2, a_3, a_9)$ taken from

uniformly distributed random numbers in $[0, 1]$ with random signs, 5 eigenvalues of $\mathcal{L}_{ij}(a_I)$ are calculated. The entries of the eigenvector that corresponds to the smallest real eigenvalue of $\mathcal{L}_{ij}(a_I)$ are then inserted as values for $\vec{a}_{\mathrm{II}} = (a_4, a_5, a_6, a_7, a_8)$.

From the system's equations in short notation as introduced at the beginning of this chapter:

$$\dot{a}_I = \mathcal{N}(a_I, a_J) + \mathcal{R}(a_i, a_j), \tag{4.24}$$

$$\dot{a}_i = \mathcal{L}_{ij}(a_I) a_j, \tag{4.25}$$

one obtains for the Newton's method:

$$\vec{a}^{(n+1)} = \vec{a}^{(n)} - \begin{pmatrix} \frac{\partial \mathcal{N}}{\partial a_I} & \frac{\partial \mathcal{R}}{\partial a_i} \\ \frac{\partial \mathcal{L}_{ij}}{\partial a_I} a_i^{(n)} & \mathcal{L}_{ij} \end{pmatrix}^{-1} f(\vec{a}^{(n)}), \tag{4.26}$$

where the matrix is the Jacobian $Df(\vec{a}^{(n)})$ of the system.

Applying the Newton's method and repeating the whole procedure for the respective new values of $\vec{a}_{\mathrm{I}}$, the eigenvalue of the quasilinear subsystem approaches zero, $\vec{a}_{\mathrm{II}}$ approaches the neutral eigenvector and the search converges to a fixed point of the system. For 10 iterations and 20000 random initial conditions approximately 35% converged to each of the two sets of fixed points shown in table 4.1, 21% converged to the laminar state and for the remaining 9% of initial conditions no fixed point of the system was found.

5 Streamwise quasilinear approximation for plane Couette flow

The results presented in this chapter in parts have been published in *Quasilinear approximation for exact coherent states in parallel shear flows*, Marina Pausch, Qiang Yang, Yongyun Hwang and Bruno Eckhardt, Fluid Dynamics Research 51(1): 011402 (2019).

5.1 Introduction

The quasilinear approximation as introduced in chapter 2.3.1 is applied to Direct Numerical Simulations (DNS) of plane Couette flow. In contrast to previous studies, for example by Thomas et al. (2014, 2015), Nikolaidis et al. (2016), Marston et al. (2016) and Tobias and Marston (2017), which compared statistical properties of the flow, we will here analyse and compare properties of the system from a dynamical system's point of view, i.e. we will focus on exact coherent structures (ECS) and their bifurcations. Known ECS of the full nonlinear system are continued to the quasilinear system and it is shown that many important properties are kept within the approximation, even if the number of active modes in downstream direction is significantly reduced.

5.2 Plane Couette flow

In plane Couette flow an incompressible fluid between two infinitely extended plates is driven by the moving upper and lower walls at $y = \pm d/2$, which move at constant speed $\pm U_0$ in opposite x-directions, see figure 5.1. The coordinate system is chosen with x pointing in streamwise, z in spanwise and y in wall-normal direction.

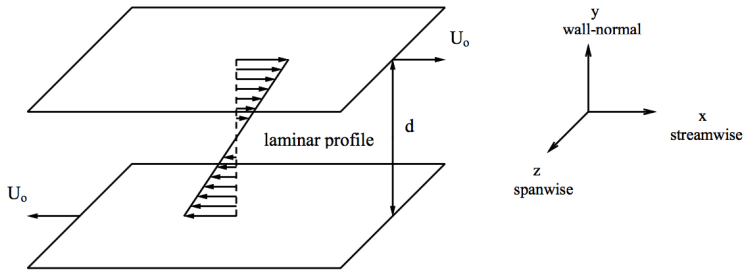

Figure 5.1: The geometry of plane Couette flow.

Scaling the velocity $\vec{u}$ by U_0, lengths by $d/2$ and time by $d/(2U_0)$, the nondimensionalized Navier-Stokes equations are obtained

$$\frac{\partial \vec{u}}{\partial t} + (\vec{u}\,\vec{\nabla})\vec{u} = -\vec{\nabla}p + \frac{1}{Re}\Delta\vec{u}, \tag{5.1}$$

$$\vec{\nabla}\,\vec{u} = 0, \tag{5.2}$$

with the Reynolds number $Re = (U_0 d)/(2\nu)$ and the kinematic viscosity ν.

For plane Couette flow the rotation and translation symmetries of the Navier-Stokes equations are restricted by the presence of the walls to (Gibson et al., 2009):

$$\sigma_x[u,v,w](x,y,z) = [-u,-v,w](-x,-y,z), \tag{5.3}$$

$$\sigma_z[u,v,w](x,y,z) = [u,v,-w](x,y,-z), \tag{5.4}$$

$$\sigma_{xz}[u,v,w](x,y,z) = [-u,-v,-w](-x,-y,-z), \tag{5.5}$$

$$\tau(l_x,l_z)[u,v,w](x,y,z) = [u,v,w](x+l_x,y,z+l_z). \tag{5.6}$$

Physically, σ_x is a rotation by π around the z-axis and σ_z is a reflection at the x,y-plane. σ_{xz} corresponds to a point-reflection at the origin and $\tau(l_x,l_z)$ describes continuous translations by l_x and l_z in the streamwise and spanwise direction, respectively.

5.3 Numerical simulations

For the DNS of plane Couette flow in the following two chapters, the open-source code `channelflow` by J. Gibson has been used and adapted for computations within the quasilinear approximation. `Channelflow` is designed to solve the incompressible Navier-Stokes equation in channel geometries. The boundary conditions are periodic in streamwise and spanwise directions with length L_x and L_z, respectively, and there are no-slip boundary conditions at the walls, i.e. the fluid at the wall moves with velocity ± 1.

For the computations, the total velocity field is decomposed into the base flow and fluctuations, i.e. $\vec{u}_{tot} = y\vec{e}_x + \vec{u}$ for plane Couette flow. The deviations $\vec{u}$ from the laminar flow $y\vec{e}_x$ then satisfy Dirichlet boundary conditions at the walls: $\vec{u}(x, \pm 1, z) = \vec{0}$. The deviations form a vector space, i.e. they can be multiplied by scalars and added to one another. This is not valid for the total velocity fields as the boundary conditions at the walls would be violated.

The velocity field is expanded in Fourier x Chebychev x Fourier modes in the x-, y- and z- directions. The resolution of the grid $[N_x, N_y, N_z]$ sets the possible Fourier wavenumbers $-N_x/2+1 \leq k_x \leq N_x/2$ and $-N_z/2+1 \leq k_z \leq N_z/2$ and thus defines the length scale of flow structures that can be resolved by this finite set of Fourier modes. For smooth functions the representation by Fourier modes is spectrally accurate. The magnitudes of the Fourier coefficients then decrease rapidly which allows for the representation of a field by its Nth order truncated Fourier series (Canuto et al., 1988). Another advantage is that a differentiation in spectral space reduces to a multiplication with ik_x or ik_z, respectively. For time-stepping a third-order semi-implicit backwards-differentiation scheme is used with 2/3-dealiasing in x and z.

`Channelflow` provides routines for the computation of (relative) equilibria and periodic orbits with a Newton-Krylov algorithm based on the work by Viswanath (2007) as well as for the calculation of eigenvalues and eigenvectors using Arnoldi-iteration. For further details of the code we refer to the `channelflow` website `http://channelflow.org`.

As the translation invariance in x- and z-direction is approximated by periodic boundary conditions for the numerical computations, an important symmetry

subgroup is $S = \{e, s_1, s_2, s_3\}$ with

$$s_1[u,v,w](x,y,z) = [u,v,-w](x+\frac{L_x}{2},y,-z) \tag{5.7}$$

$$s_2[u,v,w](x,y,z) = [-u,-v,w](-x+\frac{L_x}{2},-y,z+\frac{L_z}{2}) \tag{5.8}$$

$$s_3[u,v,w](x,y,z) = [-u,-v,-w](-x,-y,-z+\frac{L_z}{2}) \tag{5.9}$$

which are the so-called "shift-reflect" and "shift-rotate" transformations. Many of the known equilibria and periodic orbits, including the NBC-equilibria, belong to the "S-invariant subspace", i.e. they are invariant under the symmetry group S. This means if $\vec{u}(\vec{x},t)$ is a solution, so are $s_1\vec{u}(\vec{x},t)$, $s_2\vec{u}(\vec{x},t)$ and $s_1s_2\vec{u}(\vec{x},t) = s_3\vec{u}(\vec{x},t)$. However, spanwise traveling waves cannot be invariant under s_1 (and thus s_3) symmetry as the operation contains an inversion of the spanwise velocity. Likewise, streamwise traveling waves cannot be invariant under s_2 or s_3 symmetry. Solutions which are invariant under s_3 symmetry always are stationary as s_3 prevents drifting in both directions.

5.3.1 Quasilinear approximation

For the quasilinear approximation explained in chapter 2.3, the Fourier modes are the required basis modes of the velocity field (compare equations (2.6) and (2.7)):

$$\vec{u} = \sum_{k_x=-N_x/2+1}^{N_x/2} \tilde{\vec{u}}_{k_x}(y,z)\, e^{2\pi i k_x x/L_x} \tag{5.10}$$

and thus the flow field can be decomposed by the respective choice of Fourier wave numbers k_x. Decomposing the velocity field into streamwise constant and streamwise varying modes then consists in a separation of the $k_x = 0$ modes into group I and the $k_x \neq 0$ modes into group II (equations (2.9) and (2.10)):

$$\vec{u}_{\mathrm{I}} = \tilde{\vec{u}}_0(y,z) \tag{5.11}$$

$$\vec{u}_{\mathrm{II}} = \sum_{k_x\neq 0} \tilde{\vec{u}}_{k_x}(y,z)\, e^{2\pi i k_x x/L_x} \tag{5.12}$$

The Navier-Stokes equations for the two groups thus become:

$$\partial_t \vec{u}_\mathrm{I} + \mathcal{P}_\mathrm{I}(\vec{u}_\mathrm{I}\nabla)\vec{u}_\mathrm{I} + \mathcal{P}_\mathrm{I}(\vec{u}_\mathrm{II}\nabla)\vec{u}_\mathrm{II} + \nabla p = \frac{1}{Re}\Delta\vec{u}_\mathrm{I} \tag{5.13}$$

$$\partial_t \vec{u}_\mathrm{II} + \mathcal{P}_\mathrm{II}(\vec{u}_\mathrm{I}\nabla)\vec{u}_\mathrm{II} + \mathcal{P}_\mathrm{II}(\vec{u}_\mathrm{II}\nabla)\vec{u}_\mathrm{I} + q\,\mathcal{P}_\mathrm{II}(\vec{u}_\mathrm{II}\nabla)\vec{u}_\mathrm{II} = \frac{1}{Re}\Delta\vec{u}_\mathrm{II} \tag{5.14}$$

In equation (5.14), the self-interacting term $\mathcal{P}_\mathrm{II}(\vec{u}_\mathrm{II}\nabla)\vec{u}_\mathrm{II}$ of the group II modes, which is omitted within the quasilinear approximation, contains a prefactor q. This prefactor can be used to tune between the full Navier-Stokes equation ($q = 1$) and the quasilinear approximation ($q = 0$) to continue exact coherent structures from the full to the quasilinear system.

Note that for calculations within the quasilinear approximation a degeneracy occurs, because the equations of group II split into individual equations for the different orthogonal Fourier modes in k_x. As the group II equations are linear neither the amplitudes nor the phases of the different k_x-modes are fixed. Only the squares of the group II modes contribute to the equations of group I so that phase shifts between the group II modes are not visible in $\vec{u}_\mathrm{I}$. This degeneracy can lead to unfamiliar looking flow fields, but it is avoided by continuation from the nonlinear states so that the relative phases are inherited. Moreover, many of the observed quasilinear states in this chapter only contain modes $k_x = 0$ and ± 1 and the degeneracy requires at least one more set of modes to become visible.

In this chapter we study exact solutions of the Navier-Stokes equations and their properties in different periodic domains within the streamwise quasilinear approximation and compare them to results of the full nonlinear system.

5.4 NBC states in optimal domain

The results presented here are for the well-known Nagata-Busse-Clever states (NBC) in the optimal domain found by Waleffe (Nagata, 1990; Clever and Busse, 1997; Waleffe, 2003) which is $\Omega = [L_x, L_y, L_z] = [2\pi/\alpha, 2, 2\pi/\gamma]$ with $\alpha = 0.577$ and $\gamma = 1.150$ and a resolution of $[N_x, N_y, N_z] = [48, 33, 48]$. "Optimal domain" here means that the states appear at the lowest Reynolds number compared to other box sizes, namely at $Re_c = 127.7$. The bifurcation diagram $D(Re)$ is

shown in blue in figure 5.2, where D is the energy dissipation of the states

$$D = \frac{1}{V}\int_V dV|\vec{\nabla} \times (\vec{u} + y\vec{e}_x)|^2, \tag{5.15}$$

that equals 1 for the laminar state. $V = L_x L_y L_z$ is the volume of the box. In the bifurcation there appear the so-called lower and upper branch solutions, indicating the lower and higher dissipation of the states. From the corresponding flow fields of the upper and the lower branch state at $Re = 400$ in the left column of figure 5.3, it can be seen that the coherent structures correspond to a pair of high and low speed streamwise streaks, the upper branch with a modulation in downstream direction. The colour indicates the velocity of the fluid in the streamwise x-direction and the arrows show the in-plane velocities at the walls and in the midplane, i.e. for $y = 0$.

The corresponding quasilinear states are obtained by continuation from the full system. Figure 5.2 also shows the bifurcation diagram for the quasilinear states as a red curve. The two curves are qualitatively in good agreement, but for higher Re the upper branches move apart. The bifurcation points lie close together at $Re_c = 127.7$ and $D_c = 1.8$ in the full system and at $Re_c = 135.5$ and $D_c = 1.75$ in the quasilinear system. The velocity fields of the corresponding quasilinear states look very similar to the states in the full nonlinear system. The quasilinear upper branch state has less structure and less variation in spanwise direction, but the quasilinear approximation captures the essential elements of the flow structure.

The bifurcation curves of the upper branches of the two systems separate for higher Re. This can be explained by the amplitudes of the different Fourier modes which are shown in figure 5.4 for the states from figure 5.3, i.e. the upper and lower branch NBC states in the full and in the quasilinear system at $Re = 400$. In the full nonlinear system the upper branch state is supported by many more modes than the lower branch state. In the quasilinear approximation the spanwise k_z amplitudes are similar to those in the full system, but for both quasilinear states only modes $k_x = 0$ and ± 1 contribute to the flow field. All modes with $k_x > 1$ are inactive. Thus, for the upper branch state there are many modes that contribute in the full system and are not captured by the

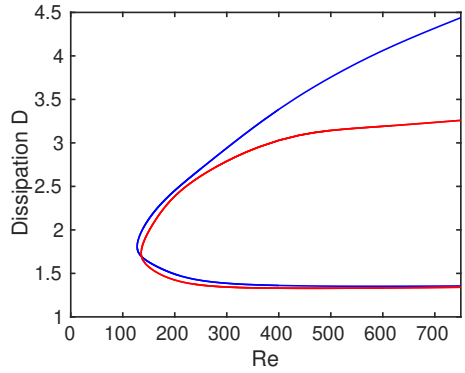

Figure 5.2: Bifurcation diagrams for the Nagata-Busse-Clever state in the optimal domain for the nonlinear system and the quasilinear approximation in blue and red, respectively.

quasilinear approximation. Furthermore, higher wavenumber modes make a larger contribution to the energy dissipation than the low wavenumber modes. This explains both the differences which are visible in the velocity fields and the separation in the bifurcation diagram between the full nonlinear and the quasilinear upper branch. However, it is remarkable that the differences in dissipation in the bifurcation diagram are not very large.

5.4.1 Stability properties

The differences in the modal content have consequences for the stability of the states. Figure 5.5 shows the eigenvalues of the NBC states in the full and in the quasilinear system at $Re = 400$. For the lower branch state, the eigenvalue spectra are very similar for both systems. The quasilinear state only has one positive eigenvalue 0.0353, i.e. one unstable direction, just as the nonlinear state with eigenvalue 0.0315. For the upper branch the differences are bigger: the nonlinear state has 17 pairs of complex conjugate and 1 real positive eigenvalues and thus in total 35 positive eigenvalues, whereas the quasilinear state only has 10 positive eigenvalues, all of which come in complex pairs. The maximal quasilinear eigenvalues are $0.0241 \pm 0.0253i$ which is much smaller than $0.053 \pm 0.042i$ for the nonlinear state. Thus the quasilinear upper branch state has

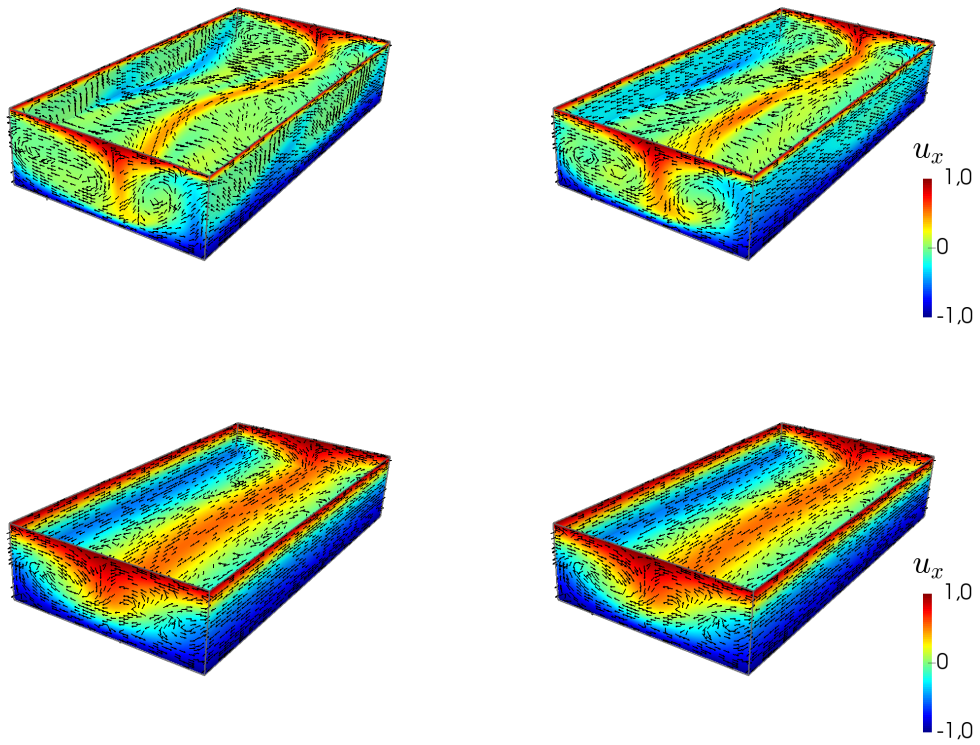

Figure 5.3: Velocity fields of the upper branch (top row) and lower branch (lower row) NBC states in the full system (left column) and in the quaslinear approximation (right column) at $Re = 400$. The flow in the midplane of the domain is shown, i.e. for $y = 0$. The velocity field is coded by colour and 2d vectors. The colourmap indicates the fluid velocity in the streamwise x-direction, the arrows indicate in-plane velocities.

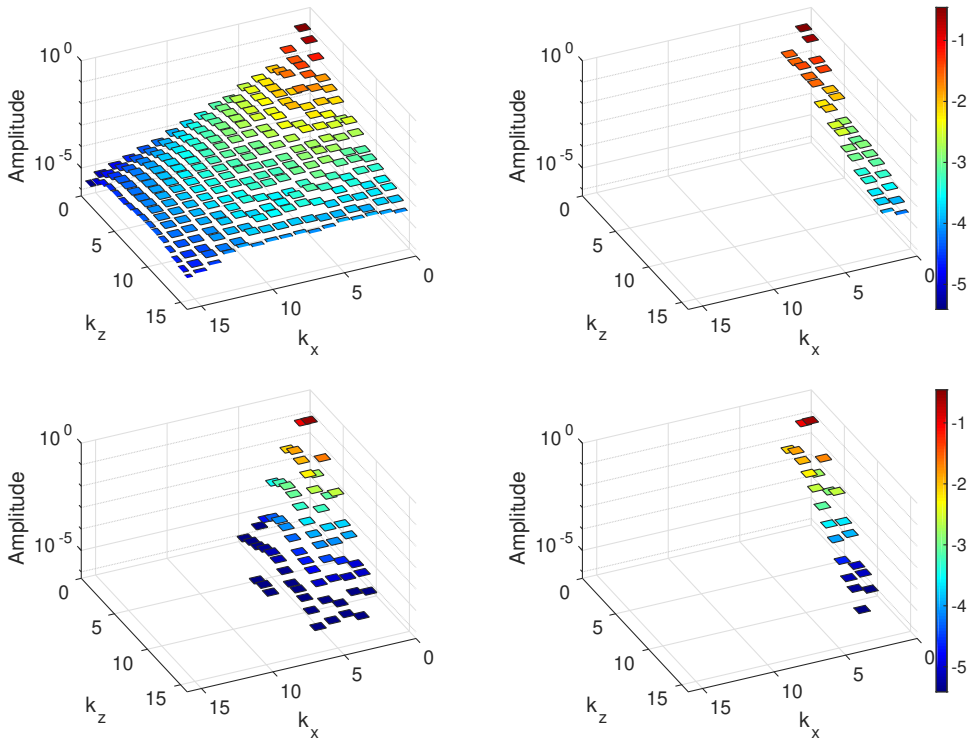

Figure 5.4: Modal content of the ECS from figure 5.3. Shown are the upper branch (top row) and lower branch states (lower row), obtained from the full Navier-Stokes equation (left column) and within the quasi-linear approximation (right column).

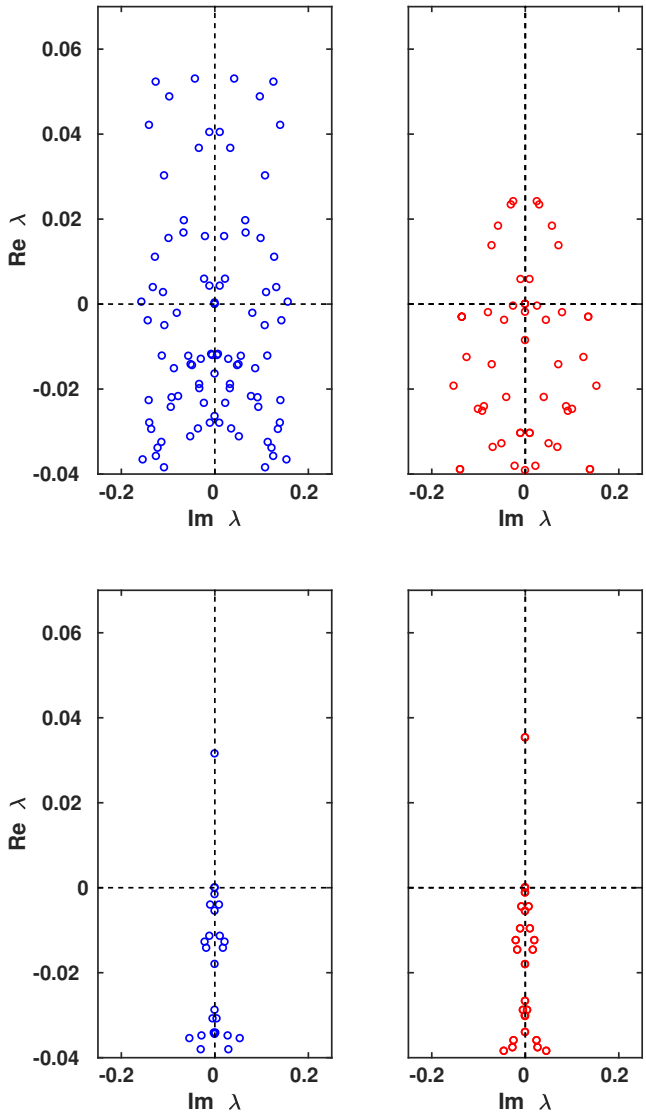

Figure 5.5: Eigenvalue structure of the NBC states from figure 5.3 at $Re = 400$. The eigenvalues of the upper branch (top row) and lower branch (lower row) are shown for the nonlinear state in blue (left) and the quasilinear state in red (right), respectively.

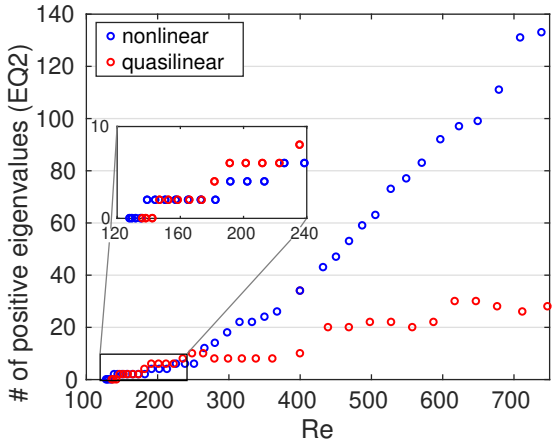

Figure 5.6: Number of positive eigenvalues vs. Re for the upper branch state in the full Navier-Stokes setting (blue) and in the quasilinear approximation (red).

less and weaker instabilities than the nonlinear state, probably caused by the absence of the higher streamwise Fourier modes.

Figure 5.6 shows how the number of positive eigenvalues of the upper branch state changes with increasing Re. Again, blue symbols correspond to the nonlinear and red symbols to the quasilinear system, respectively. Compared to the nonlinear state, the number of positive eigenvalues of the quasilinear upper branch state increases non-monotonically and more slowly.

Furthermore, in the quasilinear system some of the complex conjugated eigenvalue pairs are degenerated. The figure shows the total number of positive eigenvalues, not the number of distinct ones. We observed that all the eigenfunctions which belong to non-degenerated eigenvalues only contain the modes with $k_x = 0, \pm 1$. The eigenfunctions belonging to the sets of two degenerated pairs of eigenvalues each contain one particular higher k_x-pair only. For example, at $Re = 400$ the quasilinear upper branch state has five positive complex conjugate eigenvalue pairs and all corresponding eigenvalues contain only modes $k_x = 0, \pm 1$. With increasing Re more eigenvalues become unstable and for $Re \approx 440$ there are eight complex conjugate pairs of positive eigenvalues and one set of two degenerated complex conjugate pairs, so 20 positive eigenvalues

in total. In the eigenfunctions only modes $k_x = 0, \pm 1$ are present, except of in the eigenfunctions which belong to the degenerated set. These eigenfunctions only contain the modes $k_x = \pm 2$. For $Re \approx 530$ further eigenvalues have become unstable, among them another set of two degenerated eigenvalue pairs with eigenfunctions containing only modes $k_x = \pm 3$. Once these unstable eigendirections are present, perturbations in these additional modes can grow and thus the modes can be activated in the temporal evolution of the flow field (see section 5.7).

The degeneracy of the eigenvalues can be explained by considering the linearization around the fixed point $\vec{u}_{FP}$ for the quasilinear system. In general, a fixed point of a system of differential equations $\dot{\vec{u}} = f(\vec{u})$ satisfies

$$\dot{\vec{u}}_{FP} = \vec{f}(\vec{u}_{FP}) = 0. \tag{5.16}$$

The linearization around the fixed point leads to

$$\frac{d}{dt}(\vec{u}_{FP} + \delta\vec{u}) \approx \vec{f}(\vec{u}_{FP}) + Df(\vec{u}_{FP})\,\delta\vec{u} \tag{5.17}$$

with a perturbation $\delta\vec{u}$ and the Jacobian $Df(\vec{u})$ of the system. With (5.16) this reduces to

$$\dot{\delta}\vec{u} = Df(\vec{u}_{FP})\,\delta\vec{u}. \tag{5.18}$$

The eigenvalues and eigenvectors of the Jacobian $Df(\vec{u}_{FP})$ thus determine the stability properties of the fixed point.

As has been introduced in chapter 4, the quasilinear system reads in short notation

$$\dot{u}_I = \mathcal{N}(u_I, u_J) + \mathcal{R}(u_i, u_j) \tag{5.19}$$

$$\dot{u}_i = \mathcal{L}_{ij}(u_I)u_j \tag{5.20}$$

with components I, J of group I and i, j of group II, respectively, and the linearization thus yields

$$\frac{d}{dt}\begin{pmatrix}\delta u_I \\ \delta u_i\end{pmatrix} = \begin{pmatrix} \frac{\partial \mathcal{N}}{\partial u_I} & \frac{\partial \mathcal{R}}{\partial u_i} \\ \frac{\partial \mathcal{L}_{ij}}{\partial u_I} u_{i,FP} & \mathcal{L}_{ij} \end{pmatrix}\begin{pmatrix}\delta u_I \\ \delta u_i\end{pmatrix}. \tag{5.21}$$

For the quasilinear system the equations of group II separate for the different Fourier modes in streamwise direction k_x. As the fixed point of the system only contains modes with $|k_x| \leq 1$, the lower left entry of the Jacobian vanishes for all $|k_x| \geq 2$:

$$\frac{d}{dt}\begin{pmatrix}\delta u_I \\ \delta u_i\end{pmatrix} = \begin{pmatrix}\frac{\partial \mathcal{N}}{\partial u_I} & \frac{\partial \mathcal{R}}{\partial u_i} \\ 0 & \mathcal{L}_{ij}\end{pmatrix}\begin{pmatrix}\delta u_I \\ \delta u_i\end{pmatrix}. \tag{5.22}$$

This results in a degeneracy of the eigenvalues of the $(\pm k_x)$-couples for all $|k_x| \geq 2$. The corresponding eigenfunctions only contain the respective $(\pm k_x)$-modes as the Fourier modes for different k_x are orthogonal.

5.4.2 Energy spectra

There are different possibilities to recover the full Navier-Stokes equation from the quasilinear approximation. One way is to increase the number of modes for which the self-interactions are kept. This approach will be discussed in chapter 6. Another possibility is to introduce a nonlinearity parameter q for the nonlinear terms that are omitted for the approximation, i.e. the self-interactions of the group II modes in the equations of group II. This parameter can then be tuned from $q = 0$, which is the quasilinear approximation, to $q = 1$, which is the full Navier-Stokes equation. Figure 5.7 shows the modal content of the upper branch NBC state for $Re = 400$ when the parameter is varied from $q = 1$ in the upper left to $q = 0.5$ in the upper right and $q = 0.1$ in the lower left and finally to $q = 0$ in the lower right. The panels on the left show the decadic logarithm of the amplitude of the modes in dependence on k_x and k_z. The amplitude is defined as

$$A(\vec{u}_{k_x,k_z}) = \sqrt{\frac{1}{V}\int_V |\vec{u}_{k_x,k_z}|^2 dV} \tag{5.23}$$

with

$$\vec{u}_{k_x,k_z} = \tilde{\vec{u}}_{k_x,k_z}(y)\, e^{2\pi i(k_x x/L_x + k_z z/L_z)}. \tag{5.24}$$

The right panels show the sum of absolute values of the Chebyshev coefficients for a few of the lowest order combinations of (k_x, k_z) on the diagonal, i.e. $(0,0), (1,1), \ldots$, versus k_y. There is a smooth transition from the nonlinear to the quasilinear system. With decreasing parameter q the modal content is

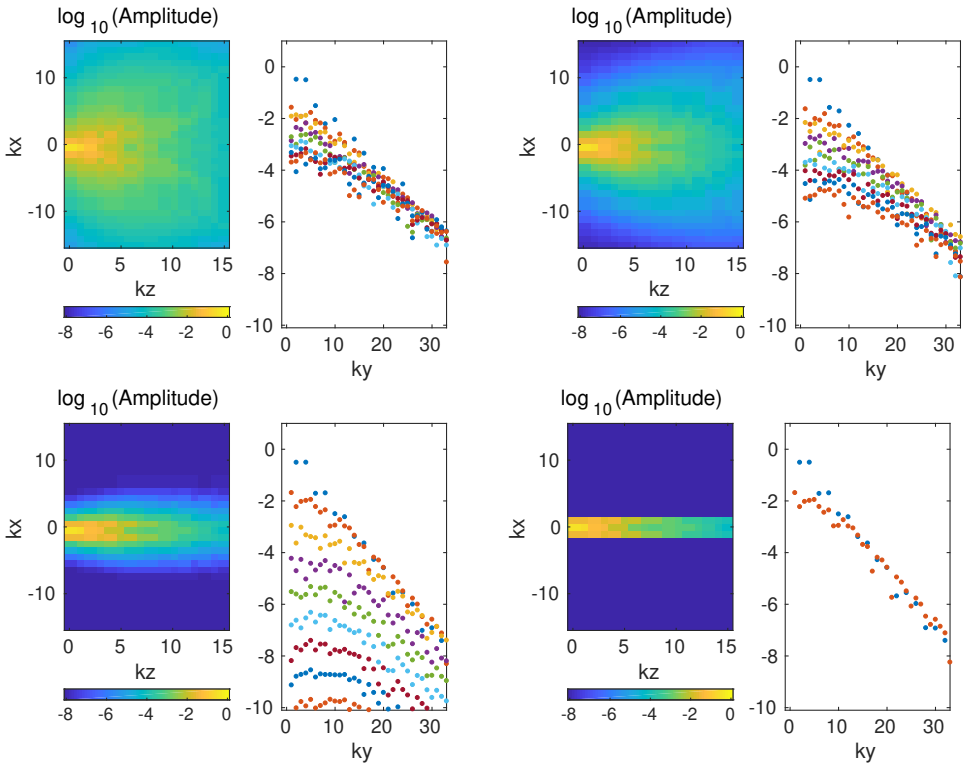

Figure 5.7: Modal content on a logarithmic scale during the transition from the fully nonlinear system (top left) to the quasilinear approximation (lower right) for the NBC upper branch at $Re = 400$. The transition is achieved by varying the nonlinearity parameter q from $q = 1$ (upper left) to $q = 0.5$ (upper right), $q = 0.1$ (lower left) and then $q = 0$ (lower right). The panels on the left show the amplitudes of the modes in the k_x-k_z-plane and the panels on the right show the sum of absolute values of the Chebyshev coefficients for (k_x, k_z) on the diagonal vs k_y. In the 2-d representations one can see how the modes in k_x are removed, with very little change in the amplitudes along k_z. In the panels on the right, different colours indicate different k_x. For $q = 1$ they are all close together, then begin to separate as q decreases and for $q = 0$ only two sets are left.

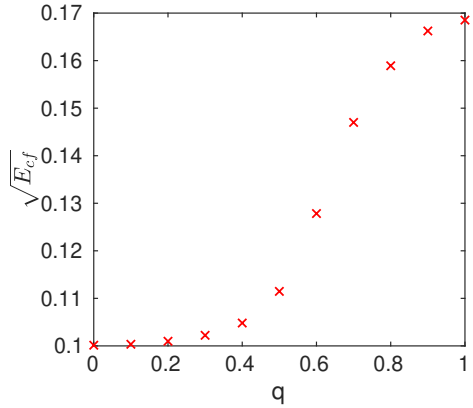

Figure 5.8: Square root of the cross flow energy E_{cf} for the transition from the quasilinear solution at $q = 0$ to the nonlinear state at $q = 1$ corresponding to figure 5.7.

reduced until most of the k_x modes eventually vanish for $q = 0$ while the amplitudes along k_z do not change much. For the quasilinear approximation only modes with $k_x = 0, \pm 1$ contribute to the flowfield.

This smooth but non-uniform transition is also apparent when the square root of the cross-flow energy of the states is plotted for different values of the nonlinearity parameter q, see figure 5.8. The cross-flow energy is the energy contained in the transverse components of the flow field and thus it does not contain the dominant downstream contribution of the laminar flow. It is defined as

$$E_{cf} = \frac{1}{V} \int_V (v^2 + w^2) dV \tag{5.25}$$

with v and w being the spanwise and wall-normal components of the flow field $\vec{u} = (u, v, w)$. For q-values smaller than 0.5, E_{cf} is considerably smaller than for the nonlinear state. For higher values of q there is a rather steep increase until E_{cf} lies within 10% of its full value when q exceeds 0.8.

5.4.3 Statistics

In figure 5.9 the statistics of the quasilinear states in red are compared to the fully nonlinear NBC states in blue. Each of the panels contains solid lines for

the states at the bifurcation point, as well as dashed and dotted lines for the upper and lower branch states at $Re = 400$. The first panel shows the mean profiles U as functions of y, for which the agreement between quasilinear and nonlinear solutions is very good. As discussed above, for the nonlinear states many more modes with higher downstream wavenumbers contribute to the flow field, especially for the upper branch state. This is recognizable when comparing the root mean squares (rms) of the velocity components $\vec{u}' = (u', v', w')$ where the prime $'$ denotes the difference from the mean flow. The quasilinear states contain less modes which results in smaller spanwise fluctuations and hence in larger differences in the comparison of v'_{rms} and w'_{rms}. The differences in u'_{rms} and in the Reynolds stress $-\overline{u'v'}$ are smaller. As expected from the comparison of the velocity fields and bifurcation diagrams, the overall agreement is better for the lower branch state than for the upper branch state.

5.5 Quasilinear states in the W03 domain

The results presented in this section are for the so-called W03 cell (Waleffe, 2003), i.e. for $[L_x, L_y, L_z] = [2\pi/\alpha, 2, 2\pi/\gamma]$ with $\alpha = 1.14$ and $\gamma = 2.5$, and for a resolution of $[N_x, N_y, N_z] = [48, 35, 48]$. Halcrow (2008) provides a detailed study of known ECS for this domain size. We compare equilibria from the `channelflow` database to their quasilinear approximations. We study the modal content of the states as well as their stability properties and the bifurcation diagrams. In figure 5.10 the bifurcations for the different nonlinear and quasilinear states are shown in blue and red, respectively.

EQ1 / EQ2: These are again the NBC states, but in a different computational box so that some properties are changed. The lower branch state EQ1 and the upper branch state EQ2 appear in a saddle-node bifurcation at $Re_c \approx 218.0$ for the nonlinear system and at $Re_c \approx 216.0$ for the quasilinear system, see figure 5.10a. Here again, the bifurcation diagram is captured very well by the quasilinear approximation, except that D is lower for the quasilinear upper branch state. From the computation of the eigenvalues, we find that the lower branch solution has only one unstable direction for a large range of Re, but it has three positive eigenvalues shortly after the bifurcation in the quasilinear system, just

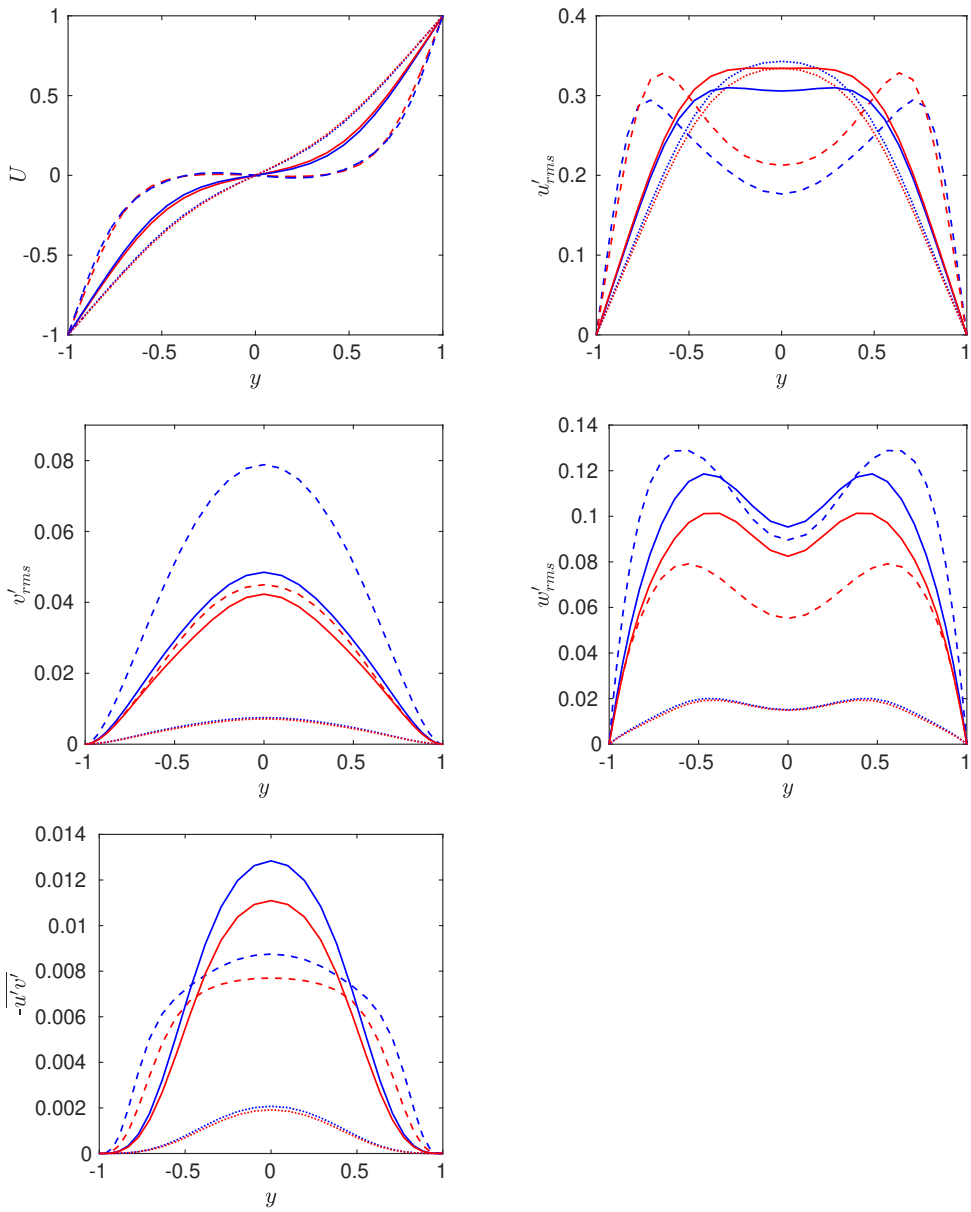

Figure 5.9: Statistics for the NBC state for the nonlinear states in blue and for the quasilinear states in red. The upper branch and lower branch state at $Re = 400$ are shown with dashed and dotted lines, respectively. Solid lines show the states at their respective bifurcation point. Shown are the mean flow U, the root mean square of the velocity components (for the difference from the mean flow) and the Reynolds stress in dependence on y.

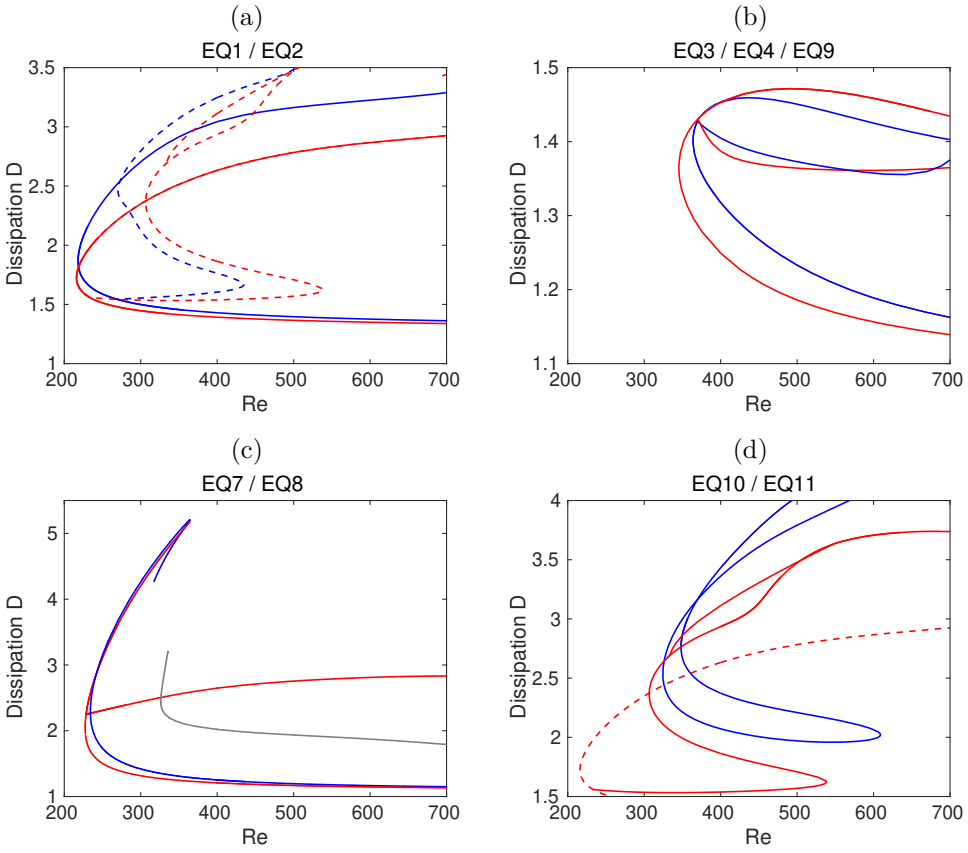

Figure 5.10: Bifurcation diagrams for different equilibria in the W03 domain for the nonlinear system and the quasilinear approximation in blue and red, respectively. The dashed lines indicate a connection between the states from a) and d). The grey line in c) shows the bifurcation diagram of EQ5/EQ6 in the nonlinear system; the continuation to the quasilinear system has led to the state bifurcating from EQ8ql (red line).

as in the nonlinear system. When an unstable $s3$-symmetric eigenfunction of EQ1 becomes stable, a further state bifurcates from EQ1 at $Re \approx 269$ (dashed blue) in the nonlinear and at $Re \approx 233$ (dashed red) in the quasilinear system. The lower and upper branch states are S-symmetric; the bifurcating states are $s3$-symmetric. The other unstable eigenfunction is s2-symmetric in both cases and its change of stability seems to be related to the bifurcation of a spanwise traveling wave (TW1).

EQ3 / EQ4 / EQ9: The comparison of the bifurcation diagrams in figure 5.10b again shows a good qualitative agreement of the curves. EQ3 and EQ4 lie within the S-invariant subspace and they appear in a saddle-node bifurcation at $Re_c \approx 345.9$ and $D_c \approx 1.37$ for the quasilinear system and at $Re_c \approx 363.9$ and $D_c \approx 1.40$ for the nonlinear system. EQ9 is $s3$-symmetric and bifurcates from EQ4 at $Re \approx 370.2$ in the nonlinear and at $Re \approx 369.3$ in the quasilinear case, respectively, when a $s3$-symmetric eigenfunction becomes unstable.

EQ7 / EQ8: EQ7 and EQ8 also lie within the S-invariant subspace and they appear at $Re_c \approx 227.3$ and $D_c \approx 2.07$ in the quasilinear approximation in contrast to $Re_c \approx 234.1$ and $D_c \approx 2.27$ for the fully nonlinear system, see figure 5.10c. EQ8 does not exist for values of $Re \gtrsim 364$ in the nonlinear system so we have not continued it to higher Re for the quasilinear system. Figure 5.11 shows a comparison of the modal content and the flowfields of EQ7 at $Re = 400$. For the nonlinear state only every second mode is active and thus the quasilinear state contains very few modes. Even with this small set of modes the velocity field is captured remarkably well in the quasilinear approximation.

EQ5 / EQ6: The continuation of both the S-invariant equilibria EQ5 and EQ6 leads to the same state in the quasilinear system. This state is also S-invariant and bifurcates from the quasilinear state EQ8ql, see figure 5.10c. The bifurcation diagram of the nonlinear states EQ5 and EQ6 is indicated in grey.

EQ10 / EQ11: EQ10 and EQ11 possess $s3$-symmetry and appear at $Re_c \approx 306.4$ and $D_c \approx 2.4$ in the quasilinear system and at $Re_c \approx 324.5$ and $D_c \approx 2.5$ in the nonlinear system, see figure 5.10d. The states that we found from continuation of the full solutions to the quasilinear approximation correspond to the state that bifurcates from EQ1. Apparently, there is no such connection for the nonlinear system. There is, however, another state in figure 5.10a (dashed

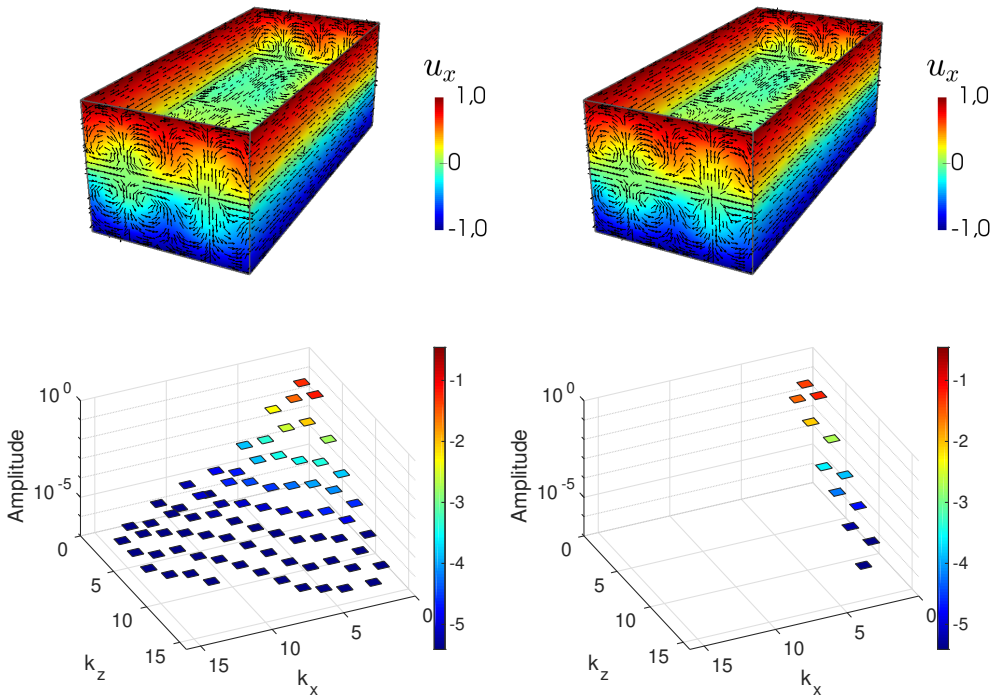

Figure 5.11: Velocity field (with laminar profile added) and modal content of EQ7 in the W03 domain at $Re = 400$ obtained from the full Navier-Stokes equation (left column) and within the quasilinear approximation (right column). The velocity in the streamwise direction is colour-coded; the arrows show in-plane velocities.

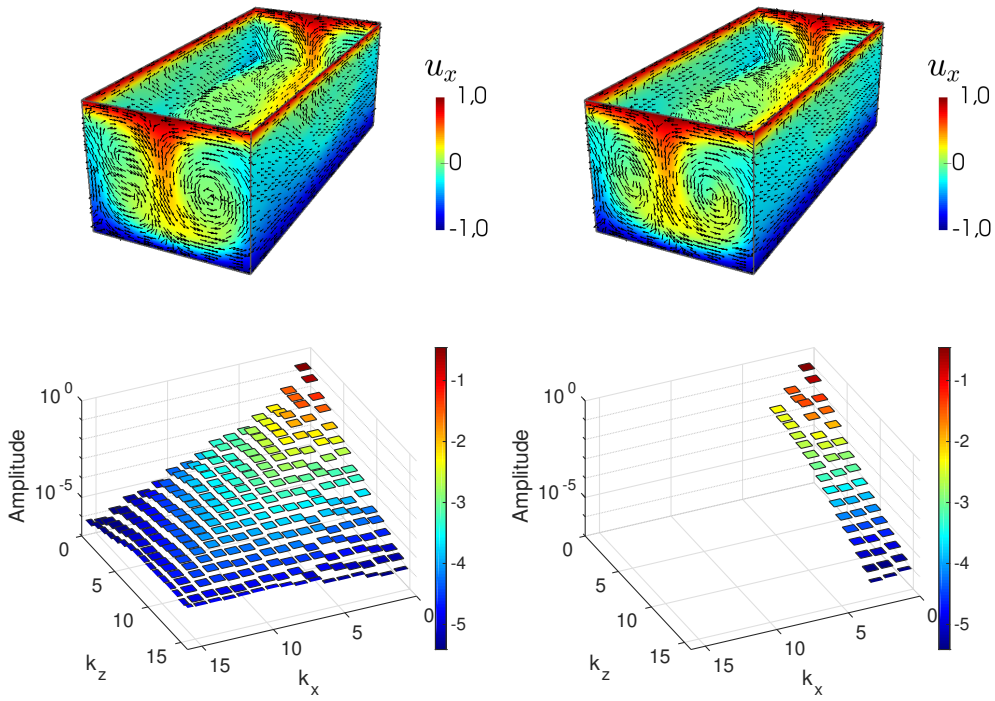

Figure 5.12: Velocity fields (with laminar profile added) and modal content of the nonlinear equilibrium EQ11 (left column) and the quasilinear equilibrium EQ11qlB (right column) at $Re = 400$. The velocity in the streamwise direction is colour-coded; the arrows show in-plane velocities.

blue) in the nonlinear system that shows such a bifurcation. The modal content of the nonlinear states EQ11 and the one from figure 5.10a mainly differ in the modes with higher k_x and that might be the reason why the states merge in the quasilinear approximation. There is a bifurcation of a further state, we call it EQ11qlB, from the upper branch quasilinear solution at $Re \approx 333.8$ and $D \approx 2.7$ which merges once again with the upper branch for higher Re.

TW1: TW1 is a $s2$-symmetric, spanwise-traveling relative equilibrium. For $Re = 400$ it has a small mean velocity in z-direction which is $\bar{u}_z = 0.0048$ in the nonlinear and $\bar{u}_z = 0.0041$ in the quasilinear system, respectively. It is not

$\mathrm{Re}(\lambda)$	$\mathrm{Im}(\lambda)$
0.0797	0.0598
0.0704	
$4.8563 \cdot 10^{-7}$	$6.3865 \cdot 10^{-7}$
$-1.9777 \cdot 10^{-7}$	
-0.0009	

Table 5.1: Leading eigenvalues $\lambda = \mathrm{Re}(\lambda) \pm \mathrm{Im}(\lambda)$ of EQ11qlB at $Re = 400$ obtained from Arnoldi iteration. There is one additional neutral eigenvalue that results from the degeneracy occuring in the quasilinear approximation. The accuracy of the neutral eigenvalues is a measure for the accuracy of the applied Arnoldi method.

shown in the bifurcation diagrams.

All equilibria discussed above only contain the streamwise modes $k_x = 0$ and $k_x = \pm 1$ in the range of transitional Reynolds numbers that are studied here. The only exception is the state EQ11qlB, which inherits the additional modes $k_x = \pm 2$, see figure 5.12. When the state bifurcates from EQ11ql at $Re \approx 334$, a pair of degenerated real eigenvalues of EQ11ql becomes unstable. The corresponding eigenvectors only contain modes $k_x = \pm 2$. Apparently, bifurcations can add further modes. We expect more such bifurcations to exist, which add more streamwise modes for higher Reynolds numbers.

As has been explained in section 5.3, a degeneracy occurs for EQ11qlB, because phase shifts between the k_2-modes of group II do not change the velocity field $\vec{u}_\mathrm{I}$ of group I. This degeneracy is visible in the eigenvalues of EQ11qlB, see table 5.1, which shows the leading eigenvalues obtained from Arnoldi iteration. There are three neutral eigenvalues, two of which result from the continuous translation symmetries in streamwise and spanwise directions. The third neutral eigenvalue is a consequence of the aforementioned degeneracy.

5.6 Dynamics and transition to turbulence

As explained in section 2.2.2, a route to the creation of a local chaotic saddle has been found within the nonlinear system (Kreilos and Eckhardt, 2012; Kreilos et al., 2014). Its starting point is the upper branch NBC state that is stable

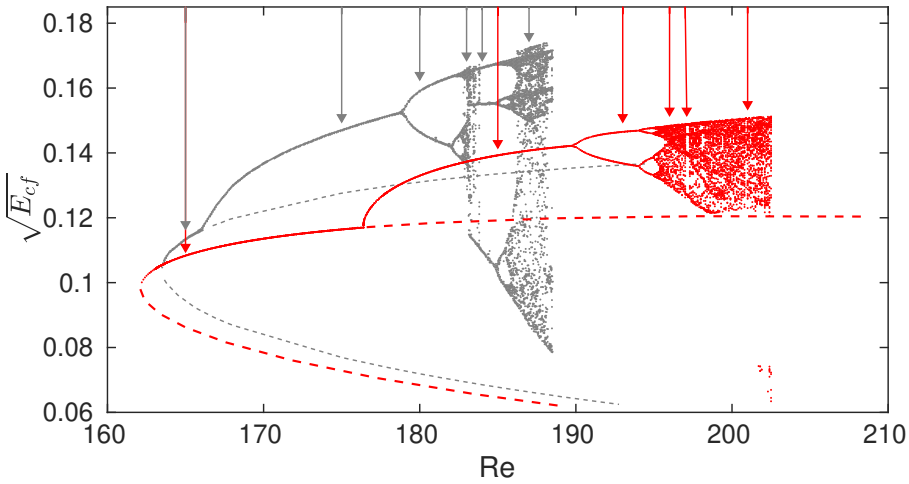

Figure 5.13: The bifurcation diagrams obtained in the full and in the quasilinear system for the $[2\pi, 2, \pi]$ domain. The data shown in grey is reproduced from Kreilos and Eckhardt (2012), the red diagram is obtained within the quasilinear approximation. The dots correspond to maxima of the cross-flow energy for a time series starting near the upper branch. The bifurcation diagrams of the upper and lower branch NBC-states are shown as dashed lines. The arrows mark the Re for which the trajectories on the attractor are shown in figure 5.14.

in the chosen computational domain of $[L_x, L_y, L_z] = [2\pi, 2, \pi]$ and in the s_1-symmetry subspace. The bifurcation scenario is shown in figure 5.13 in grey, the data is reproduced from Kreilos and Eckhardt (2012). In the bifurction diagram the maxima of the cross-flow energy E_{cf} (see equation (5.25)) of a trajectory are plotted. The initial conditions of the trajectories are chosen to lie near the upper branch state within the basin of attraction of the attractor. A single value in the diagram thus corresponds to an equilibrium state or a periodic orbit, two values to the period doubled state and a band of values to chaotic dynamics. The dashed lines indicate the bifurcation diagrams of the upper and lower branch NBC states.

In the nonlinear system, the upper branch state loses its stability in a Hopf bifurcation at $Re = 166.05$, leading to a stable periodic orbit. A period dou-

bling cascade follows, which increases the complexity of the attracting state and thereby leads to the formation of a local chaotic attractor. At $Re \approx 188.51$, the attractor is destroyed in a crisis bifurcation when it touches its own boundary, i.e. the stable manifold of the lower branch state. For higher Re, a local chaotic saddle is left behind.

A qualitatively identical scenario is obtained for the quasilinear system for the same computational box and symmetry subspace. In the bifurcation diagram shown in red in figure 5.13, the stable quasilinear upper branch state also undergoes a Hopf bifurcation and a periodic doubling cascade leading to chaotic bands with periodic windows. The bifurcations occur at higher Reynolds numbers compared to the fully nonlinear system. It is noticeable that the range of $\sqrt{E_{cf}}$-amplitudes is smaller in the quasilinear case. The quasilinear system contains less small-scale modes in streamwise direction, but the lack of small-scale dynamics does not alter the properties of the system qualitatively.

The energy input I due to wall shear and the energy dissipation rate D are defined as

$$I(t) = 1 + \frac{1}{2A} \int_A dxdz \left(\left.\frac{\partial u}{\partial y}\right|_{y=1} + \left.\frac{\partial u}{\partial y}\right|_{y=-1} \right) \tag{5.26}$$

and

$$D(t) = \frac{1}{V} \int_V dV \left(\vec{\nabla} \times (\vec{u} + y\vec{e}_x) \right)^2 \tag{5.27}$$

with the box volume $V = L_x L_y L_z$ and surface of the wall $A = L_x L_z$. D and I are normalized such that $D = I = 1$ for laminar flow and the change of the kinetic energy is $\dot{E} = -(D - I)$ (Gibson et al., 2008, 2009). For equilibria the total kinetic energy is constant and thus $D = I$ must be satisfied. Also for periodic orbits and for chaotic trajectories, the average kinetic energy has to be constant and therefore the time averages of D and I will be in balance.

In figure 5.14 the dynamics on the chaotic attractor is visualized for different Reynolds numbers and thus for different dynamical regimes on the attractor. The average $(D + I)/2$ of the energy input I and the energy dissipation rate D is plotted versus their difference $D - I$ for 1000 time steps of a trajectory living on the attractor. The difference $D - I$ indicates how much the energy input, which happens on the large scales, and the energy dissipation, which happens on the small scales, are out of phase. Each row of figure 5.14 compares the

dynamics in the nonlinear system (left column, blue) to the quasilinear system (right column, red) for a certain regime of the attractor. The corresponding Re are specified in each figure and they are marked with arrows in figure 5.13. The data is obtained from the energy input I and energy dissipation rate D of the deviation $\vec{u}$ from the laminar flow. Adding the laminar profile would shift the curves by $+1$ in vertical direction. Figure 5.14a corresponds to the stable upper branch NBC state that undergoes a Hopf bifurcation which leads to the periodic orbit shown in figure 5.14b. Figure 5.14c shows a state resulting from the period-doubling cascade and figures 5.14d and 5.14f show trajectories in the chaotic regime. Figure 5.14e corresponds to an intermediate periodic window.

For both systems the growing complexity of the chaotic attractor can be observed. In the nonlinear case the trajectories are more convoluted. However, the overall range in D and I is similar for both systems. Note that in the quasilinear system the bifurcation scenario starts from the upper branch NBC state which only contains $k_x = 0, \pm 1$ modes in downstream direction and that no further modes are activated during the evolution of the attractor. The quasilinear system contains fewer small scale modes than the nonlinear system and thus the quasilinear dynamics on the attractor is less complex.

5.7 Turbulent trajectories

Since all studied equilibria and even the local chaotic attractor have very few active streamwise modes only, it is interesting to explore whether additional modes are activated in turbulent trajectories. Hence, we calculated long turbulent time series of $T = 100\,000$ time units starting near the quasilinear upper branch NBC state EQ2ql for the optimal domain investigated in section 5.4. Besides, the temporal mean

$$\bar{X} = \frac{1}{T} \sum_{t=0}^{T} X(t) \tag{5.28}$$

and standard deviations

$$\sigma_X = \sqrt{\frac{1}{T} \sum_{t=0}^{T} (X_i - \bar{X})^2} \tag{5.29}$$

(a) fixed point

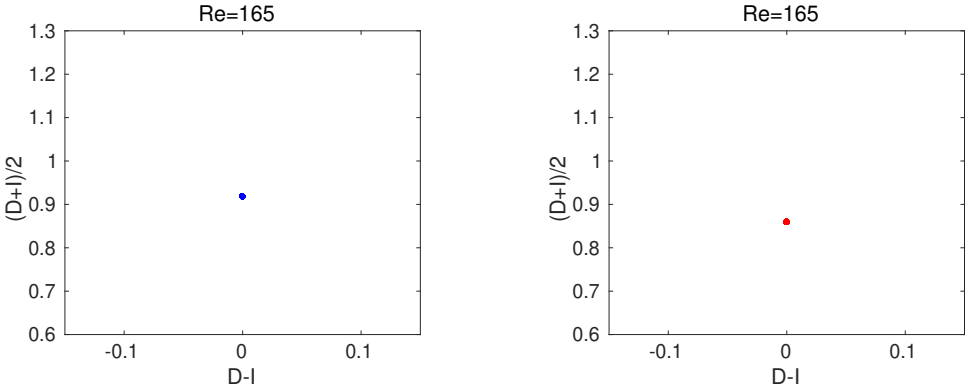

(b) periodic orbit

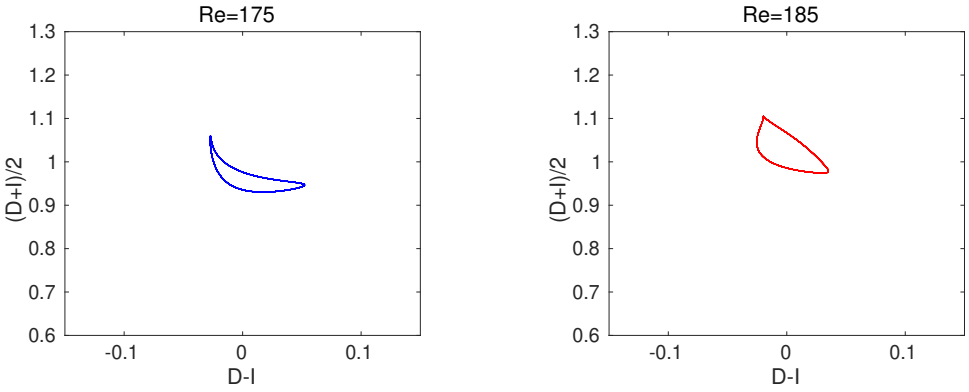

(c) period-doubled state

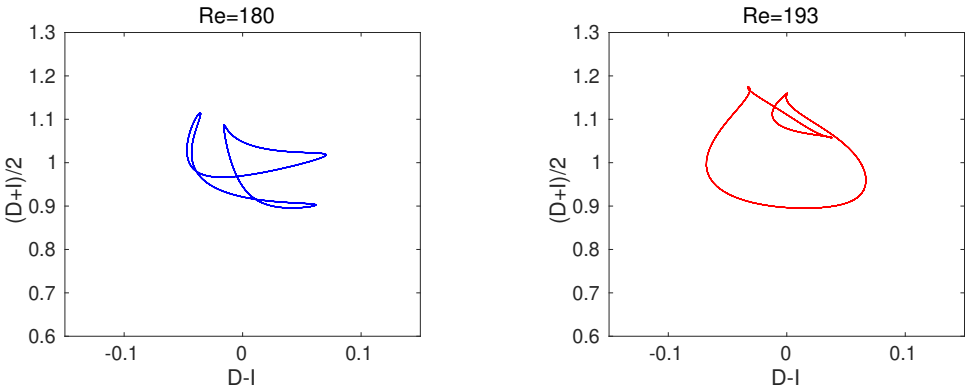

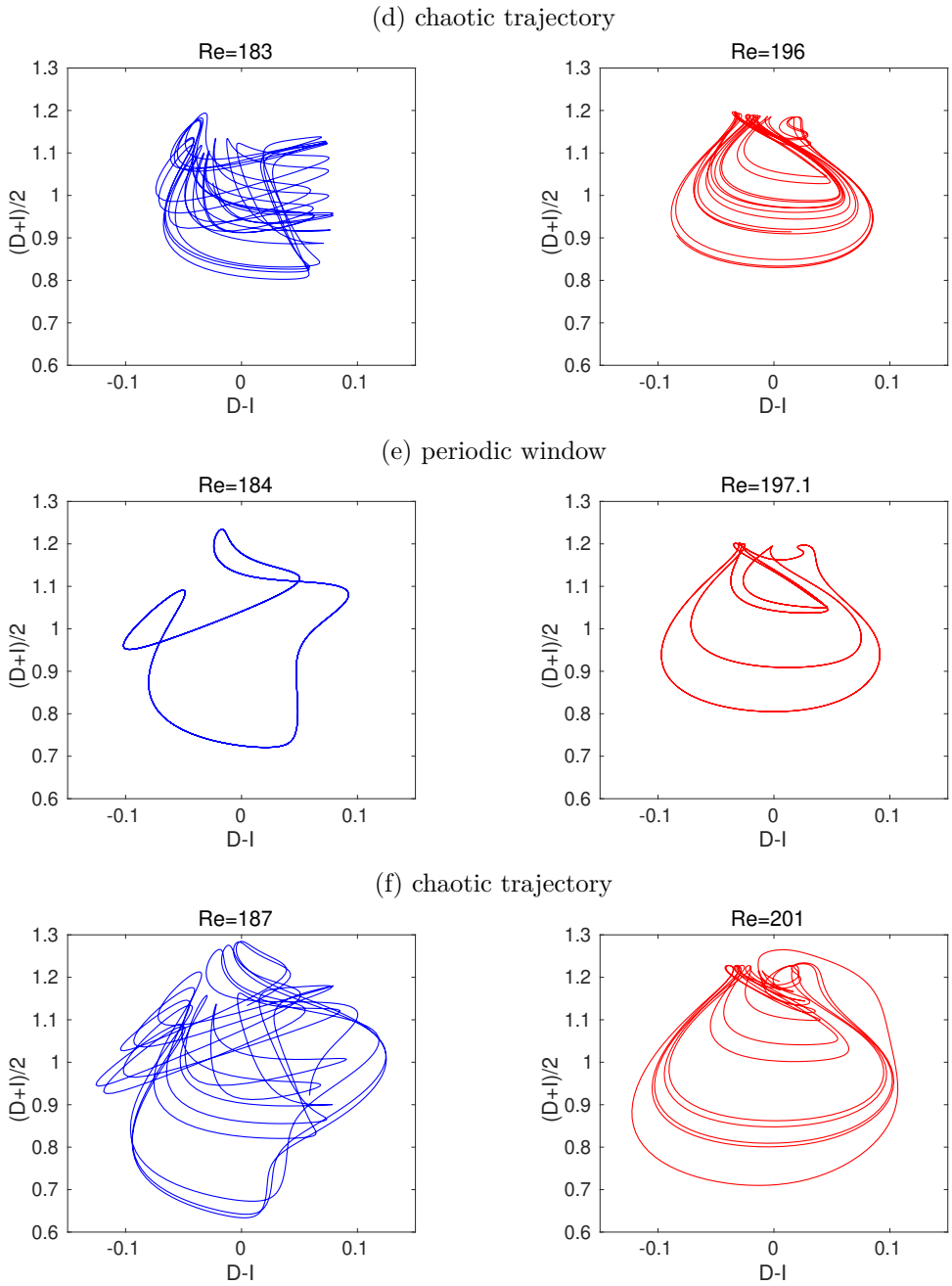

Figure 5.14: Development of the EQ2 attractor with Re. Average $(D + I)/2$ versus difference $D - I$ of the energy input I and energy dissipation rate D for 1000 time units of a trajectory for the full nonlinear system (blue, left column) and the quasilinear system (red, right column) for different dynamical regimes on the attractor. The corresponding Re are marked with grey and red arrows in figure 5.13, respectively.

$Re = 600$	$\bar{D}$	$\bar{I}$	σ_D	σ_I
nonlinear	2.24	2.24	0.39	0.30
quasilinear	2.30	2.30	0.56	0.44
$Re = 800$	$\bar{D}$	$\bar{I}$	σ_D	σ_I
nonlinear	2.80	2.80	0.37	0.27
quasilinear	2.83	2.83	0.54	0.43

Table 5.2: Comparison of mean values and standard deviations of the dissipation rate D and the energy input rate I for turbulent trajectories in the nonlinear and the quasilinear system. The statistics are calculated for time series of $T = 100\,000$ time units. The tables correspond to $Re = 600$ (top) and $Re = 800$ (bottom).

of D and I are compared with the nonlinear system for different Reynolds numbers in table 5.2. Initial transient dynamics are not included in the statistics. The mean values are similar in both systems, but the variability is larger for the quasilinear trajectories. This is also visible when considering the turbulent time series shown in figure 5.15. The figures in the upper row show the square root of the cross-flow energy $\sqrt{E_{cf}}$ for 5000 time units and the figures in the lower row show the corresponding dissipation-energy input diagram. The left and right columns show the nonlinear system in blue and the quasilinear system in red, respectively. It can be observed that for the quasilinear system the phase shift $D - I$ between dissipation rate and energy input is larger than for the nonlinear system. Since the dissipation of energy happens at the small spatial scales of the system, the quasilinear system needs more time to dissipate energy as it contains less small-scale modes and the energy cascade cannot develop.

A comparison of the modes which are active in turbulent trajectories for different Re is shown in figure 5.16. Here, the amplitude of the modes $A(\vec{u}_{k_x,k_z})$, equation (5.23), has been averaged for a time series of $T = 2000$ time units with a step width of $dT = 10$. The decadic logarithm of the temporal mean is colour-coded and plotted versus the streamwise and spanwise wavenumbers k_x and k_z. The left column again corresponds to the fully nonlinear system and the right column to the quasilinear system, respectively. For the nonlinear system, all modes contribute to the turbulent flow field and in general the amplitudes

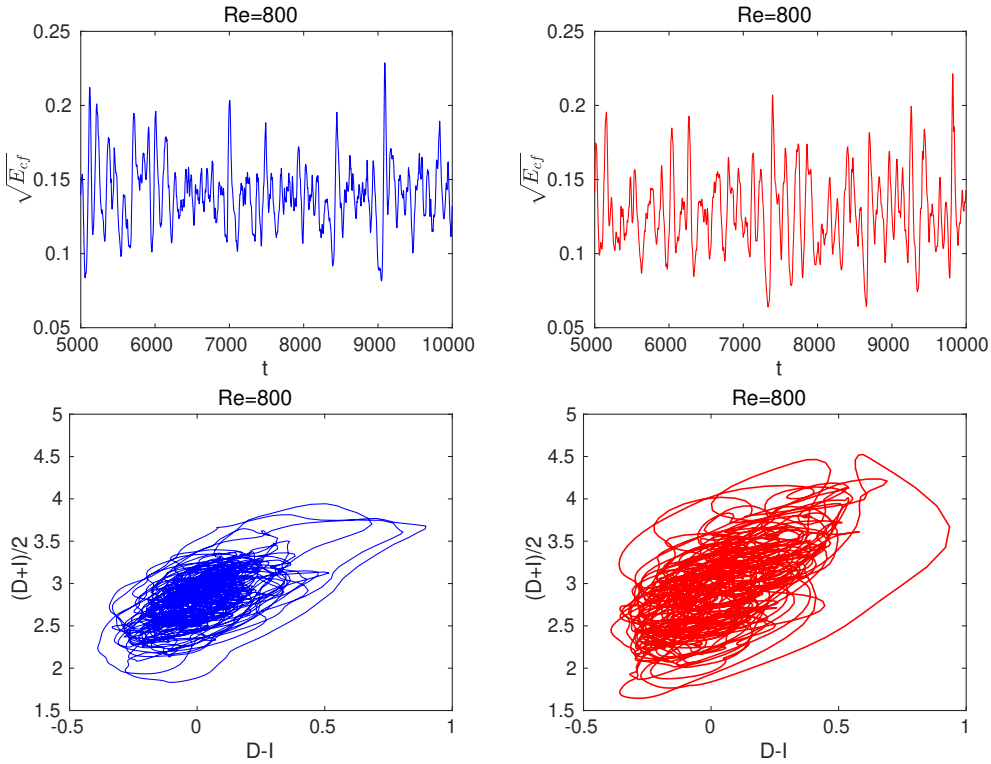

Figure 5.15: Time series of turbulent trajectories for $Re = 800$ of the fully nonlinear system (left column, blue) and the quasilinear system (right column, red). The upper row shows the square root of the cross-flow energy for 5000 time units and the bottom row shows the corresponding dissipation-energy input diagram.

decrease with increasing wavenumbers. In the quasilinear approximation the number of active modes is significantly restricted with respect to the streamwise wavenumbers. The amplitudes are slightly higher than in the nonlinear case, but they also decrease with increasing k_z. For $Re = 600$, modes $k_x = 0, \pm 1$, and ± 2 are present. With increasing Reynolds number, the amplitudes of the $k_x = \pm 2$ modes increase until for $Re \approx 800$ further modes with $k_x = \pm 3$ are activated.

When an additional mode emerges, the time series of the respective k_x-amplitude shows intermittent behaviour. This means that the signal alternates between quiet phases with very small amplitudes and active phases of significantly higher amplitudes. Figure 5.17 shows examples of such time series for different values of Re. The amplitudes of active k_x-modes which are defined as

$$A(\vec{u}_{k_x}(t)) = \sqrt{\frac{1}{V}\int_V |\vec{u}_{k_x}|^2 dV} \tag{5.30}$$

with

$$\vec{u}_{k_x} = \tilde{\vec{u}}_{k_x}(y,z,t)\, e^{2\pi i k_x x/L_x} \tag{5.31}$$

are plotted versus the time t for 15000 time units.

Each figure shows time series of the emerging ($k_x = 2$)-mode in green as well as modes $k_x = 0$ and $k_x = 1$ in blue and red for comparison. While the amplitudes of the fully active modes $k_x = 0$ and $k_x = 1$ fluctuate rather symmetrically about their means, the time series of $k_x = 2$ is intermittent. The interruptions of the quiet phases by the active phases happen irregularly and their duration cannot be predicted. With increasing Reynolds number, the proportion of active phases of the time series increases until the mode is fully activated. In the bottom figure for $Re = 800$ the emerging ($k_x = 3$)-mode can be observed which also shows intermittent behaviour.

The left panel of figure 5.18 shows the temporal mean of the energy contained in the ($k_x = 2$)-mode, i.e.

$$\langle E_2 \rangle_t = \frac{1}{T}\sum_t A^2(\vec{u}_{k_2}(t)), \tag{5.32}$$

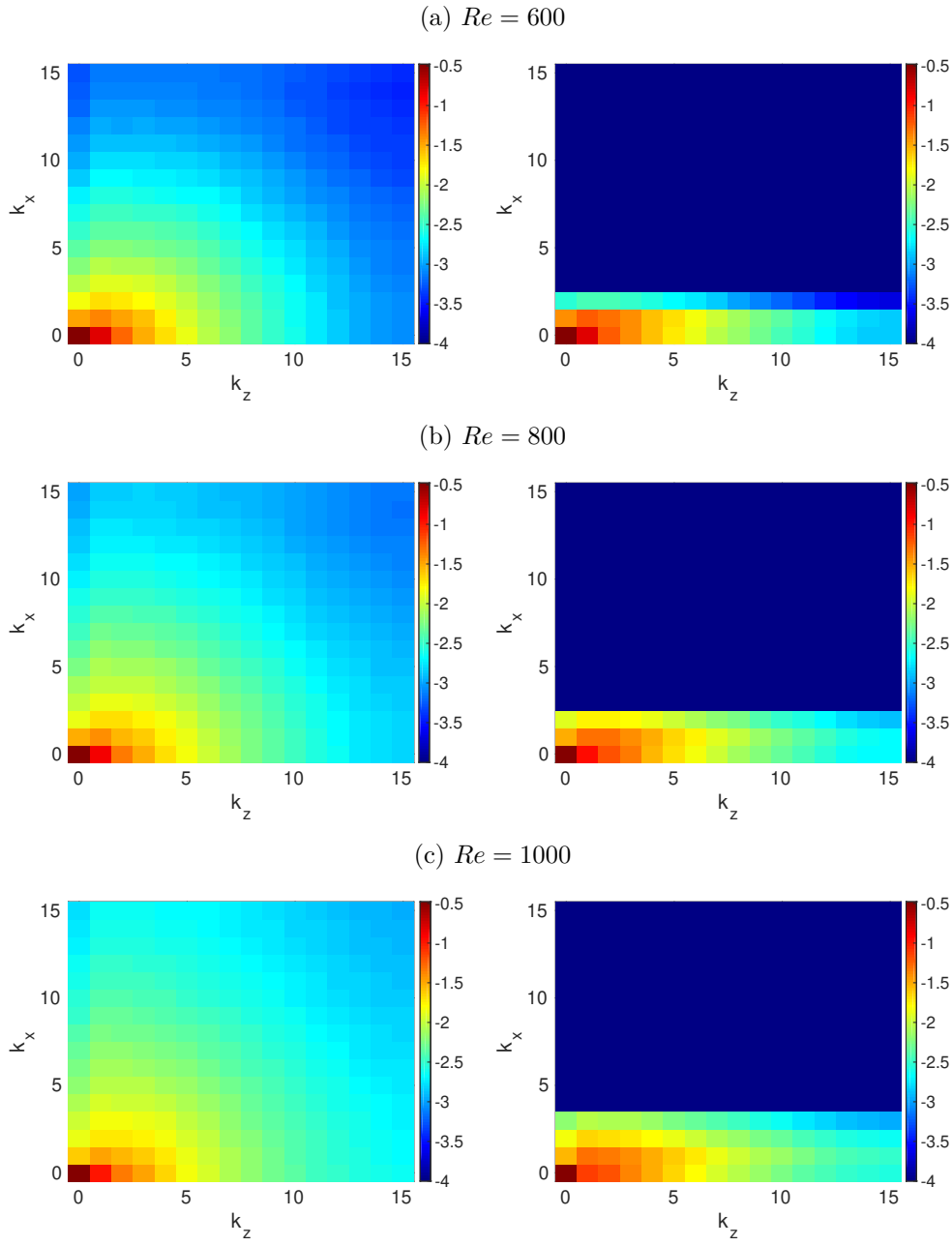

Figure 5.16: Time-averaged amplitudes of the (k_x, k_z)-modes for turbulent trajectories in the nonlinear system (left column) and in the quasilinear system (right column). Colour-coded is the decadic logarithm of the amplitudes. The rows correspond to different Reynolds numbers $Re = 600, 800, 1000$.

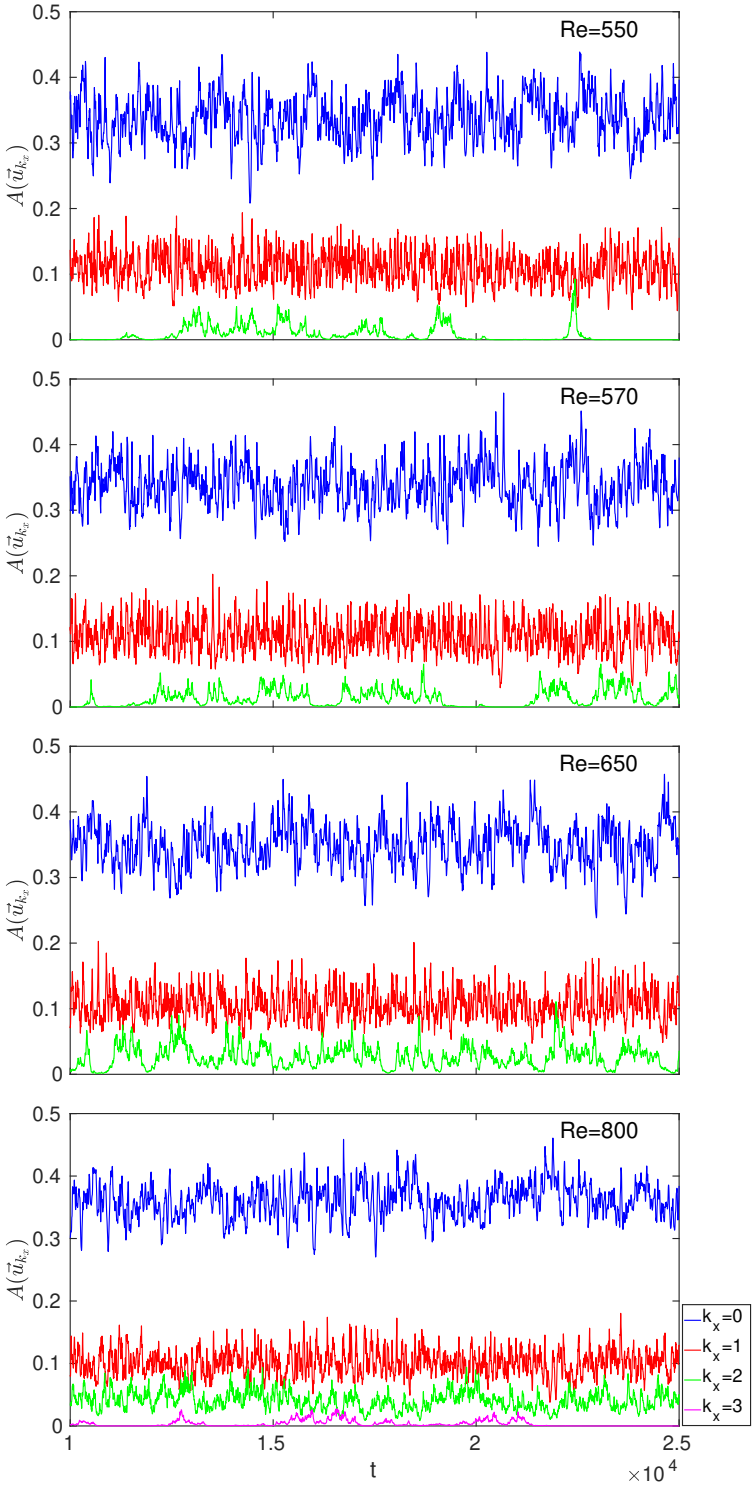

(Caption next page.)

Figure 5.17: (Previous page.) Time series of the amplitudes of the modes with $k_x = 0, 1, 2, 3$ for different Reynolds numbers $Re = [550, 570, 650, 800]$. The emerging ($k_x = 2$)- and ($k_x = 3$)- modes show intermittent behaviour.

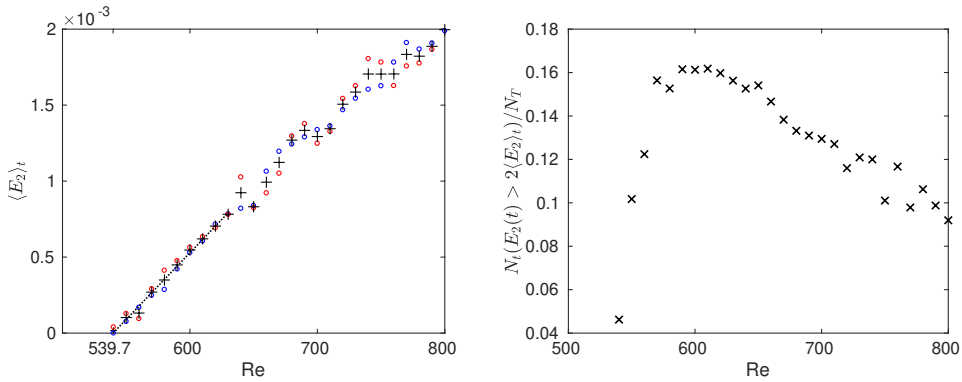

Figure 5.18: Characterization of intermittent time series. Left: Mean energy contained in the emerging ($k_x = 2$)-mode versus Re. The black crosses are obtained from a time series of $T = 100\,000$; the red and blue symbols are obtained by averaging over the first and second half of the time series and they indicate the uncertainties of the mean. The dotted black line shows a linear fit for $Re \leq 630$ that crosses the Re-axis at $Re_c = 539.7$. Right: Fraction of time for which the energy exceeds its doubled mean value as a measure of the degree of intermittency.

obtained for $T = 100\,000$ time units (black symbols). To estimate the accuracy of the mean values, the blue and red symbols show $\langle E_2 \rangle_t$ obtained by separately averaging over the first and second part of the time series, respectively. It can be seen that the uncertainties tend to increase with Re. Near the critical point, the mean energy of mode $k_x = 2$ grows linearly with Re. This corresponds to a square-root scaling for the $(k_x = 2)$-amplitudes which is generic for saddle-node bifurcations. From a linear fit for $Re \leq 630$ we obtain a critical Reynolds number $Re_c = 539.7$.

For an intermittent time series there are long periods where the values are slightly smaller than the mean, and few short periods where the values are much larger than the mean. Thus, the corresponding probability density function will be asymmetric with a long tail to larger values. To characterize the degree of intermittency of the corresponding time series, we consider the fraction of times for which the modal energy exceeds twice its mean value, i.e. for which $E_2(t) > 2\langle E_2 \rangle_t$. This quantity will pick up the frequency of strong events and is therefore a good measure for the degree of intermittency of the time series. The results are plotted in the right panel of figure 5.18. When the $(k_x = 2)$-mode is activated for the first time at $Re \approx 540$, the time series has long quiet episodes with rare intermittent bursts. The degree of intermittency increases with Re up to about 17% for $Re \approx 600$ and then it decreases while the mode becomes fully active.

5.8 Reduction of the resolution

We have seen that in the quasilinear approximation low wavenumbers in streamwise direction contribute to the dynamics only. Therefore it should be possible to reduce the number of modes in streamwise direction without changing the results. Table 5.3 and figure 5.19 show the results for turbulent trajectories of $T = 100\,000$ time units with a streamwise resolution of $N_x = 24$. As expected there is very little difference in the statistics or in the modal content compared to the quasilinear system with higher streamwise resolution.

$Re = 600$	$\bar{D}$	$\bar{I}$	σ_D	σ_I
quasilinear $N_x = 48$	2.30	2.30	0.56	0.44
quasilinear $N_x = 24$	2.30	2.30	0.55	0.43
$Re = 800$	$\bar{D}$	$\bar{I}$	σ_D	σ_I
quasilinear $N_x = 48$	2.83	2.83	0.54	0.43
quasilinear $N_x = 24$	2.86	2.86	0.55	0.43

Table 5.3: Comparison of statistics of turbulent trajectories for the quasilinear approximation with reduced resolution in x. The statistics are calculated for time series of $T = 100\,000$.

(a) $Re = 600$ (b) $Re = 800$

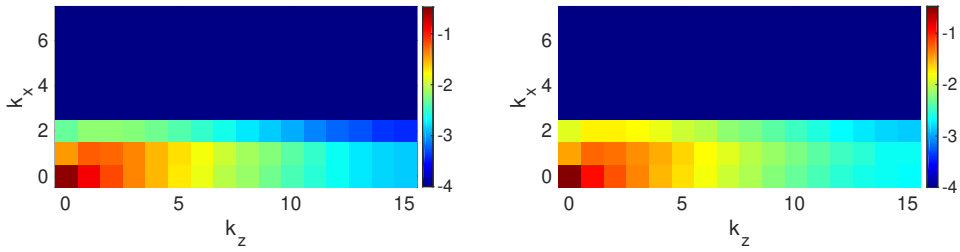

Figure 5.19: Averaged amplitudes of the (k_x, k_z)-modes for turbulent trajectories as in figure 5.16 for the quasilinear approximation with $N_x = 24$.

5.9 Concluding remarks

With the quasilinear approximation a simplified, nonlinear model is obtained which is derived directly from the Navier-Stokes equations and can be implemented in an existing DNS code. An advantage of the investigated quasilinear approach over low-dimensional models is that here the Navier-Stokes equations themselves are simplified and thus the complexity of the dynamics is reduced, while all its key features are captured as has been demonstrated by the results of this chapter. The quasilinear system becomes computationally tractable while it still describes the physics of the problem.

In particular, the streamwise quasilinear approximation reduces the dimensionality to a small set of streamwise wavenumbers only, to be precise $k_x = 0, \pm 1, \pm 2$ for the states and Reynolds numbers studied above. Higher streamwise wavenumbers, which correspond to smaller structures with smaller amplitudes in the nonlinear system, cannot survive without the nonlinear self-interactions between the streamwise varying modes. Even without the high streamwise modes, the mean profiles of the exact coherent structures do not change much compared to the nonlinear system. Moreover, turbulence can be observed in the quasilinear system with mean values for the energy dissipation and energy input rates that are comparable to those of the nonlinear dynamics. As is evident from the modal content of turbulent trajectories, streamwise modes are added when increasing the Reynolds number, but still their number is severely restricted compared to the fully nonlinear system. Hence, the resolution of computations can be significantly reduced which saves time and memory.

Furthermore, the quasilinear approximation can provide ideas for modelling certain properties of fluid flows. For example, the observation that with increasing Re higher k_x-modes become successively activated with amplitudes showing intermittent time series, suggests a hierarchical modelling approach for intermittency.

6 Generalized quasilinear approximation for plane Couette flow

6.1 Introduction

The generalized quasilinear approximation (GQL) as described in section 2.3.2 is applied to DNS of plane Couette flow. It consists in a different separation of the modes; the modes are split into small and large wavenumber modes in both translationally invariant directions, i.e. in x and in z:

$$\vec{u} = \vec{u}_{\mathrm{I}} + \vec{u}_{\mathrm{II}} \tag{6.1}$$

$$\vec{u}_{\mathrm{I}} = \sum_{|k_x|\leq\kappa_x} \sum_{|k_z|\leq\kappa_z} \tilde{\vec{u}}_{k_x,k_z}(y)\, e^{2\pi i k_x x/L_x + 2\pi i k_z z/L_z} \tag{6.2}$$

$$\vec{u}_{\mathrm{II}} = \sum_{|k_x|>\kappa_x} \sum_{|k_z|>\kappa_z} \tilde{\vec{u}}_{k_x,k_z}(y)\, e^{2\pi i k_x x/L_x + 2\pi i k_z z/L_z} \tag{6.3}$$

The wavenumber thresholds κ_x and κ_z can be chosen independently for both directions. Hence, within the GQL one can interpolate between the streamwise quasilinear approximation (QLA) that has been investigated in chapter 5, and the fully nonlinear system. The QLA is recovered in the limit $\kappa_x = 0, \kappa_z = \kappa_{z,max}$. The fully nonlinear system is obtained for $\kappa_x = \kappa_{x,max}, \kappa_z = \kappa_{z,max}$, i.e. when all modes are contained in group I.

Within the GQL, the nonlinear term is restricted such that the coupled Navier-

Stokes equations of the system become:

$$\partial_t \vec{u}_\mathrm{I} + \mathcal{P}_\mathrm{I}(\vec{u}_\mathrm{I}\nabla)\vec{u}_\mathrm{I} + \mathcal{P}_\mathrm{I}(\vec{u}_\mathrm{II}\nabla)\vec{u}_\mathrm{II} + \nabla p = \frac{1}{Re}\Delta\vec{u}_\mathrm{I} \tag{6.4}$$

$$\partial_t \vec{u}_\mathrm{II} + \mathcal{P}_\mathrm{II}(\vec{u}_\mathrm{I}\nabla)\vec{u}_\mathrm{II} + \mathcal{P}_\mathrm{II}(\vec{u}_\mathrm{II}\nabla)\vec{u}_\mathrm{I} = \frac{1}{Re}\Delta\vec{u}_\mathrm{II} \tag{6.5}$$

and thus have the same structure as for QLA with a quasilinear equation for the group II modes. Note that for the GQL four of the total of eight projections are neglected (compare equation (2.19) and figure 2.5), unlike for QLA, where three terms naturally become zero and only the self-interactions between the group II modes are omitted.

In this chapter we investigate to what extent the streamwise quasilinear approximation of the previous chapter with $\kappa_x = 0$ and $\kappa_z = 24$ can be improved by adding further streamwise modes to set I. For this purpose we investigate generalized quasilinear approximations with $\kappa_x = 2$ and $\kappa_x = 5$ for $\kappa_z = 24$. Furthermore, the number of spanwise modes contained in set I is reduced to $\kappa_z = 5$ for $\kappa_x = 0, 2$ and 5.

6.2 NBC states in optimal domain

As a first example for the application of the GQL, the upper branch of the NBC states will be discussed. The QLA for this state has been discussed in section 5.4. The domain size is $[L_x, L_y, L_z] = [2\pi/\alpha, 2, 2\pi/\gamma]$ with $\alpha = 0.577$ and $\gamma = 1.150$, and with resolution $[N_x, N_y, N_z] = [48, 33, 48]$. Figure 6.1 shows the modal content of the state at $Re = 250$ for the different choices of the thresholds κ_x and κ_z. The Reynolds numbers of the saddle-node bifurcations are given in table 6.1.

Figure 6.1b shows the amplitude of the modes for the QLA with $[\kappa_x, \kappa_z] = [0, 24]$. For figures 6.1d and f, two and five streamwise modes are added to group I, respectively, i.e. $[\kappa_x, \kappa_z] = [2, 24]$ and $[\kappa_x, \kappa_z] = [5, 24]$. As a consequence, the fixed point contains more active modes compared to the QLA case. The corresponding bifurcation points are improved compared to QLA, see table 6.1. The statistics of the nonlinear fixed point are reproduced very well for $[\kappa_x, \kappa_z] = [2, 24]$ and they are indistinguishable from the fully nonlinear case for

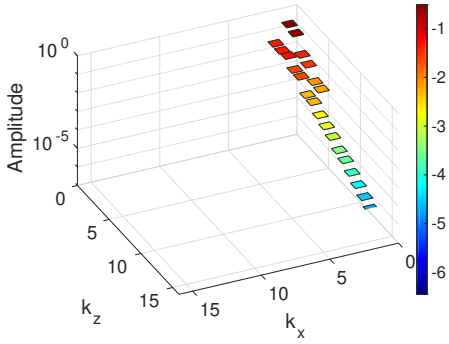

(a) $\kappa_x = 0, \kappa_z = 5$

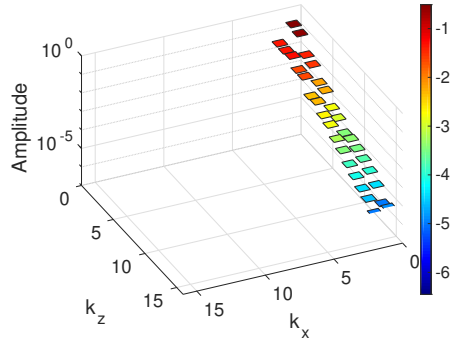

(b) $\kappa_x = 0, \kappa_z = 24$, QLA

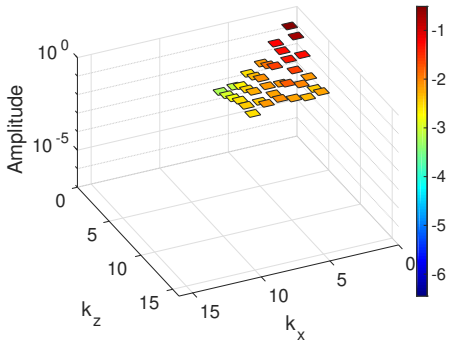

(c) $\kappa_x = 5, \kappa_z = 5$

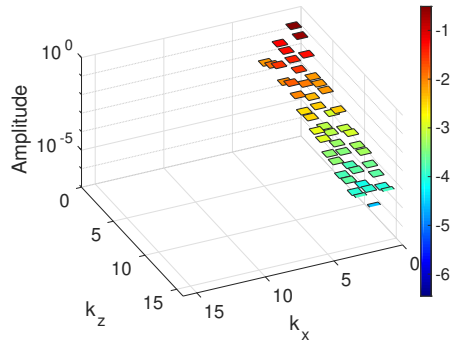

(d) $\kappa_x = 2, \kappa_z = 24$

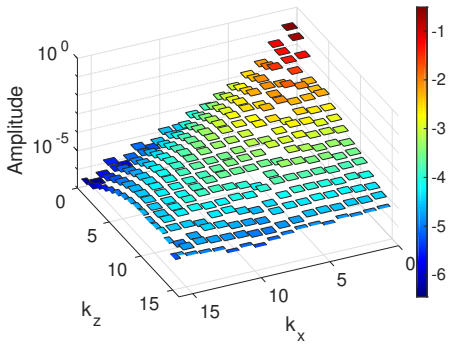

(e) $\kappa_x = 24, \kappa_z = 24$, nonlinear

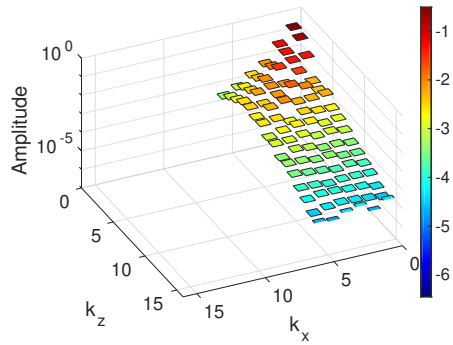

(f) $\kappa_x = 5, \kappa_z = 24$

Figure 6.1: Modal content of the NBC upper branch state at $Re = 250$ for the generalized quasilinear approximation with different streamwise and spanwise thresholds κ_x and κ_z, respectively. κ_x is increased from top to bottom with $\kappa_z = 5$ for figures a) and c) and with $\kappa_z = 24$ for the figures in the right column. Figure b) corresponds to the streamwise quasilinear approximation from chapter 5 and figure e) is the fully nonlinear case.

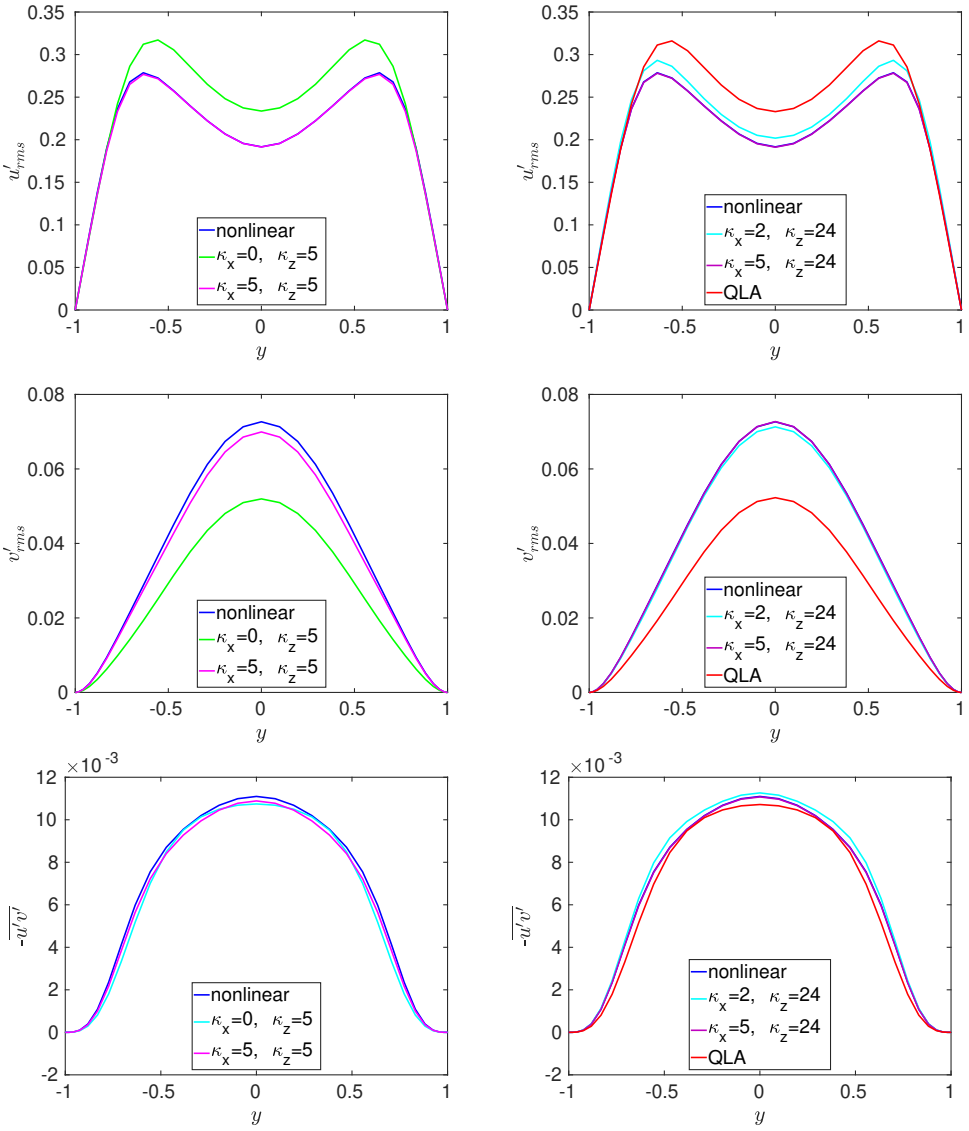

Figure 6.2: Statistics of the upper branch NBC state at $Re = 250$ for the generalized quasilinear approximations with $[\kappa_x, \kappa_z] = [0, 5]$ and $[\kappa_x, \kappa_z] = [5, 5]$ in the left column and $[\kappa_x, \kappa_z] = [2, 24]$, $[\kappa_x, \kappa_z] = [5, 24]$ and $[\kappa_x, \kappa_z] = [0, 24]$ (QLA) in the right column. Shown are the root mean squares of the streamwise and spanwise velocity components u' and v' and the Reynolds stress in dependence on y. The prime indicates deviations from the mean flow.

κ_z/κ_x	0	2	5	24
5	135.8	130.0	127.3	
24	135.5	127.6	127.6	127.7

Table 6.1: Reynolds number of the bifurcation point Re_c for different generalized quasilinear approximations with $|k_x| \leq \kappa_x$ and $|k_z| \leq \kappa_z$. The values of Re_c for the streamwise quasilinear approximation from chapter 5 and for the fully nonlinear system are shown in red and blue, respectively.

$[\kappa_x, \kappa_z] = [5, 24]$, see figure 6.2.

To quantify the differences of the individual modes we consider the relative errors, which are defined by

$$\delta A(\vec{u}_{k_x,k_z}) = \frac{|A_{nl}(\vec{u}_{k_x,k_z}) - A_{ql}(\vec{u}_{k_x,k_z})|}{|A_{nl}(\vec{u}_{k_x,k_z})|}, \tag{6.6}$$

where the subscript nl stands for nonlinear and ql stands for the respective quasilinear approximation. The relative differences of the individual modes from the fully nonlinear state are significantly reduced from top to bottom in the right column of figure 6.1, that is with increasing κ_x. The largest relative errors for the streamwise quasilinear approximation with $[\kappa_x, \kappa_z] = [0, 24]$ occur for modes $(k_x, k_z) = (0, 3)$ and $(k_x, k_z) = (1, 4)$, with $\delta A(\vec{u}_{0,3}) \approx 4.8$ and $\delta A(\vec{u}_{1,4}) \approx 1.2$, respectively. For $[\kappa_x, \kappa_z] = [2, 24]$ the relative errors increase for the smaller scales with $k_z \geq 9$, but they decrease for the larger scales, where $\delta A(\vec{u}_{0,3}) \approx 0.6$. For $[\kappa_x, \kappa_z] = [5, 24]$ all relative errors are smaller than 0.1 for $|k_x| \leq 3$ and $|k_z| \leq 9$.

Figure 6.1a is obtained by restricting the number of spanwise modes contained in set I of the streamwise quasilinear approximation to $\kappa_z = 5$. Even if the number of active $(k_x = 0)$-modes is reduced, this reduction hardly affects the relative errors of the present modes. Also the bifurcation points and the statistics of the fixed point worsen only slightly compared to QLA. The reduction in k_z does not have a strong impact on the results.

Figure 6.1c is obtained when the number of spanwise modes in set I is reduced to $\kappa_z = 5$ while at the same time the number of streamwise modes is increased

Figure 6.3: (Next page.) Bifurcation diagrams of the NBC-states in $[2\pi, 2, \pi]$ for the QLA with $[\kappa_x, \kappa_z] = [0, 24]$ and the GQL with $[\kappa_x, \kappa_z] = [2, 24]$, $[\kappa_x, \kappa_z] = [5, 24]$ and $[\kappa_x, \kappa_z] = [5, 5]$ from top to bottom. The diagrams obtained from the respective quasilinear approximation are shown in red. The diagram for the nonlinear case is reproduced from (Kreilos and Eckhardt, 2012) and is shown in grey. Dashed lines indicate the saddle-node bifurcations of the NBC-states. The arrows mark the Re for which the trajectories on the attractor are compared in figures 6.4 - 6.6.

to $\kappa_x = 5$. Here, the fixed point only contains modes with $|k_x| \leq 5$ and $|k_z| \leq 5$, but the statistics and the bifurcation point are captured fairly well with this small set of modes contained in set I, see table 6.1 and figure 6.2.

6.3 Dynamics and transition to turbulence

In section 5.6 it was shown that in QLA there exists a route to the creation of a local chaotic saddle which starts from the upper branch NBC state and which is qualitatively similar to that found by Kreilos and Eckhardt (2012) in the full nonlinear system. However, there are quantitative differences which are visible from the E_{cf}-bifurcation diagram, see figure 6.3 upper panel. The bifurcations in QLA take place at higher Reynolds numbers and the range of E_{cf}-amplitudes is smaller than in the nonlinear system. Now the E_{cf}-diagrams of the GQL will be compared to the nonlinear system for $[\kappa_x, \kappa_z] = [2, 24]$ and $[\kappa_x, \kappa_z] = [5, 24]$ with more streamwise modes, and for $[\kappa_x, \kappa_z] = [5, 5]$ with a restriction in spanwise direction. Computations again are performed in the box $[L_x, L_y, L_z] = [2\pi, 2, \pi]$ and in the s_1-symmetry subspace.

For $[\kappa_x, \kappa_z] = [2, 24]$, shown in the second panel in figure 6.3, the bifurcations of the nonlinear system are captured much better than for QLA. The saddle-node bifurcation of the NBC-states takes place at $Re_c = 162$ compared to $Re_c = 163.8$ in the nonlinear system. The Hopf bifurcation that creates the periodic orbit takes place at $Re \approx 166$ for both systems. The period-doubling bifurcations are shifted to higher Reynolds numbers; the first two occur at $Re \approx 181.5$ and $Re \approx 185.5$ instead of at $Re \approx 178.8$ and $Re \approx 182$ in the nonlinear system.

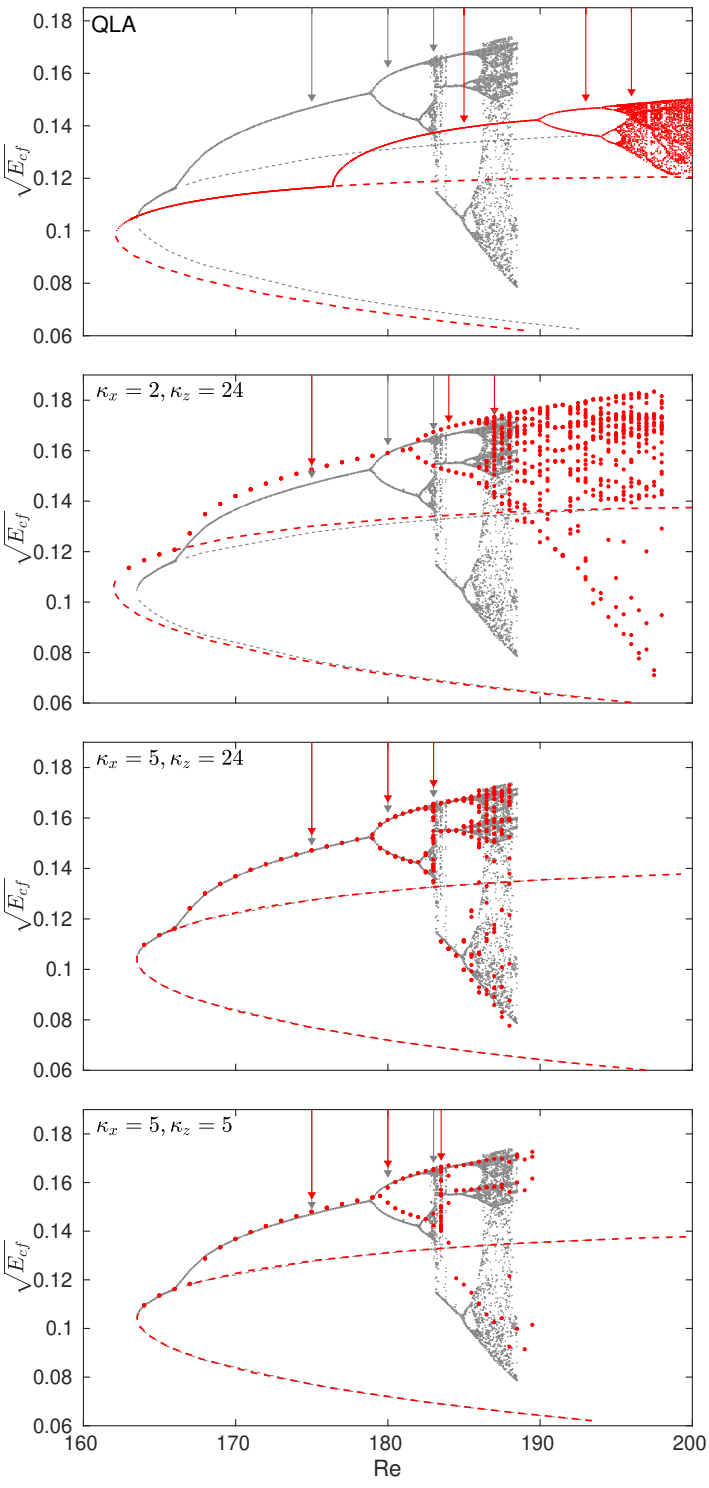

(Caption previous page.)

Also the range of amplitudes is reproduced much better than for QLA.

For $[\kappa_x, \kappa_z] = [5, 24]$, 11 streamwise modes are included in set I and the bifurcations and amplitudes of the full nonlinear system are captured almost exactly. This can be seen in the third panel of figure 6.3.

Reducing the number of spanwise modes to $\kappa_z = 5$ leads to the bifurcation diagram in the bottom panel of figure 6.3. The saddle-node bifurcation of the NBC states is still captured very well, but the Hopf and period-doubling bifurcations happen slightly later than in the nonlinear system. It is noticable that the system shows periodic behaviour in regions where the trajectories are chaotic in the fully nonlinear system. The periodic regime in the bifurcation diagram is extended compared to the nonlinear system and the chaotic bands are much narrower.

In figures 6.4 to 6.6 trajectories on the local chaotic attractor are compared for the different quasilinear approximations. Shown are $(D + I)/2$ versus $D - I$ for 1000 time steps of a trajectory (after the transient phase). The energy input I and the energy dissipation rate D have been defined in equations (5.26) and (5.27). The quasilinear trajectories (in red) are compared to the nonlinear trajectory (in grey) for different regimes of the attractor, i.e. for periodic orbits, period-doubled states or chaotic trajectories. The Reynolds numbers of the shown dynamics are marked with red and grey arrows in the bifurcation diagrams in figure 6.3. Note that the Reynolds number of the quasilinear and the nonlinear trajectory may be different such that the dynamical regime is comparable.

Figure 6.4 shows the trajectories on the periodic orbit that is created in a Hopf bifurcation from the upper branch fixed point. The four panels compare the trajectories for QLA, and GQL with $[\kappa_x, \kappa_z] = [5, 5]$, $[\kappa_x, \kappa_z] = [2, 24]$ and $[\kappa_x, \kappa_z] = [5, 24]$ (red lines) to the nonlinear system (grey lines). For all GQL the shape and location of the periodic orbit is improved compared to the QLA trajectory. This result is in agreement with the bifurcation diagrams from figure 6.3. The curves for $[\kappa_x, \kappa_z] = [5, 24]$ are indistinguishable. The approximation for $[\kappa_x, \kappa_z] = [5, 5]$ matches the nonlinear case much better than for $[\kappa_x, \kappa_z] = [2, 24]$, even though the number of modes contained in set I is smaller in the former case. Also for the period-doubled state shown in figure 6.5, the addition

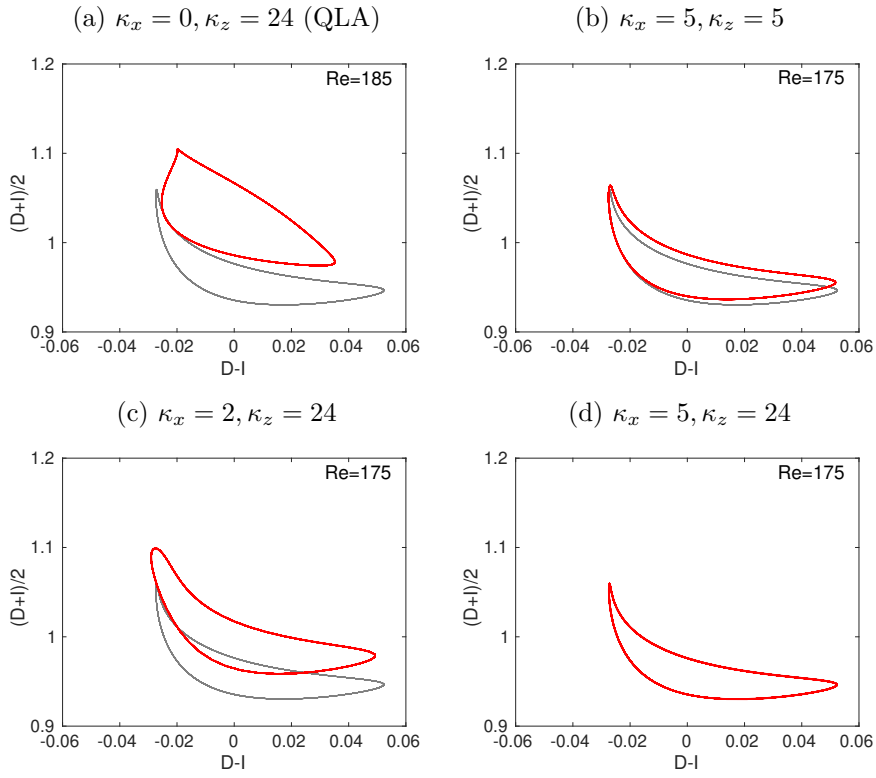

Figure 6.4: Periodic orbit on the EQ2 attractor for the different quasilinear approximations in red in comparison to the nonlinear system in grey. Shown are the average $(D+I)/2$ versus the difference $D-I$ of the energy dissipation rate D and the energy input I for 1000 time units of a trajectory. The Reynolds numbers for each quasilinear trajectory are given in the respective figure and they are marked with arrows in figure 6.3. The Reynolds number of the nonlinear periodic orbit is $Re = 175$.

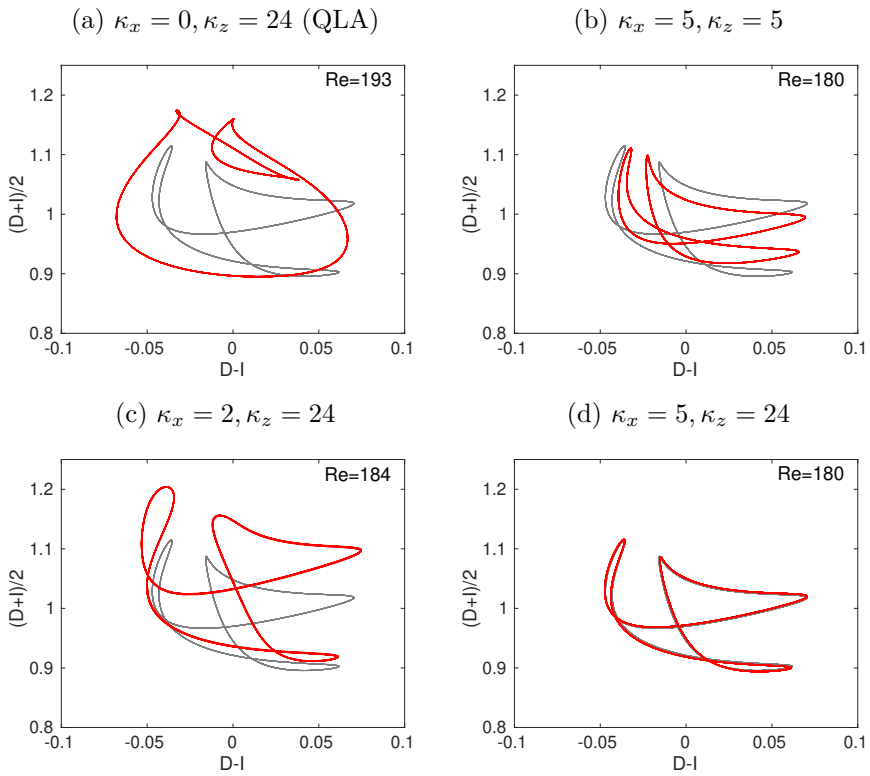

Figure 6.5: Period-doubled state on the EQ2 attractor for the different quasilinear approximations (red) as in figure 6.4. The Reynolds number of the nonlinear trajectory (grey) is $Re = 180$.

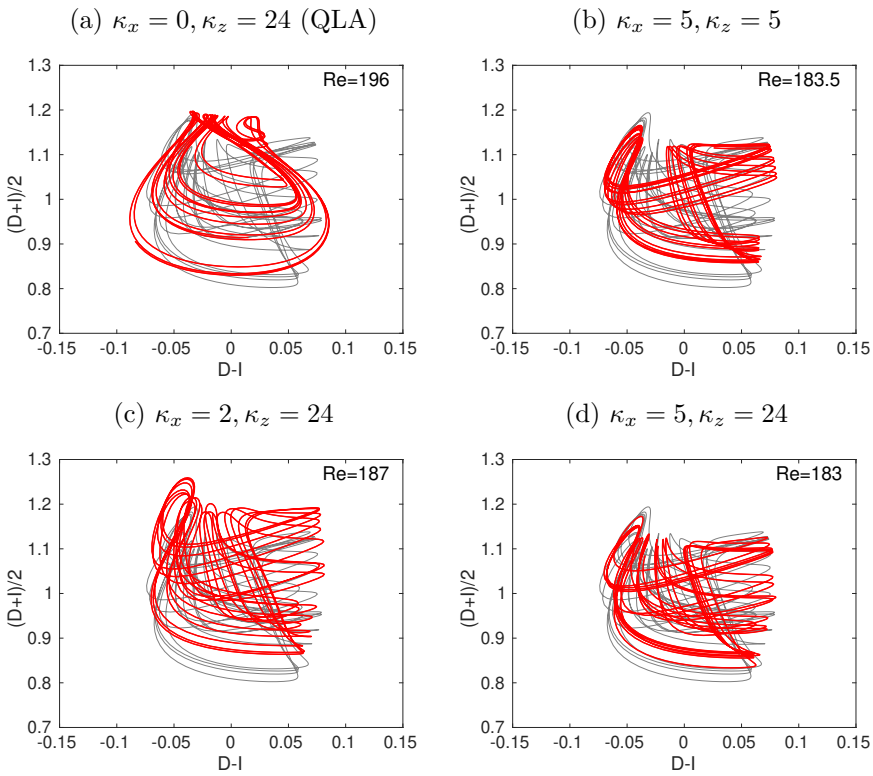

Figure 6.6: Chaotic trajectory on the EQ2 attractor for the different quasilinear approximations (red) as in figure 6.4. The Reynolds number of the nonlinear trajectory (grey) is $Re = 183$.

of modes in streamwise direction leads to an improved reproduction of the shape of the nonlinear trajectory. Again the trajectory for $[\kappa_x, \kappa_z] = [5, 24]$ shows the best agreement as it contains the most modes in set I, but also the trajectory for $[\kappa_x, \kappa_z] = [5, 5]$ matches the nonlinear one rather well. In figure 6.6, trajectories from the chaotic regime of the attractor are compared. For all generalized quasilinear approximations the trajectory looks more similar to the nonlinear one than the trajectory calculated using QLA.

In the four studied cases, no further modes are activated during the evolution of the attractor from the respective upper branch fixed point. The lack of small scale modes for the GQL with $[\kappa_x, \kappa_z] = [5, 5]$ is responsible for the reduced complexity of the attractor, which shows an extended periodic regime. Apparently, the addition of few k_x-modes to group I results in a much better quantitative representation of the dynamics on the attractor.

6.4 Turbulent trajectories

For the QLA it was shown in section 5.8 that the resolution in streamwise direction can be significantly reduced without affecting the results of the computations. For turbulent trajectories at low Reynolds numbers, only few k_x modes are active and further k_x-modes become activated successively with increasing Re. We will now adress the question whether a reduction of resolution in the approximated directions is also reasonable for the generalized quasilinear models. Moreover, the statistical means of turbulent trajectories are compared to the full system.

Figure 6.7 shows the time-averaged amplitudes of the modes (equation (5.23)) in dependence on k_x and k_z for Reynolds numbers $Re = 600$ and $Re = 800$. The left column corresponds to the approximation with $[\kappa_x, \kappa_z] = [5, 5]$ and the right column corresponds to $[\kappa_x, \kappa_z] = [5, 24]$. The averages are taken over every 10th flow field for 2000 time units and the colour correlates with the decadic logarithm of the amplitudes. For $Re = 600$ only the modes which are contained in group I are present in the turbulent trajectories. For $Re = 800$ further modes are activated in both approximations. Their amplitudes are noticeably smaller than for those modes which are contained in group I, but all modes with higher

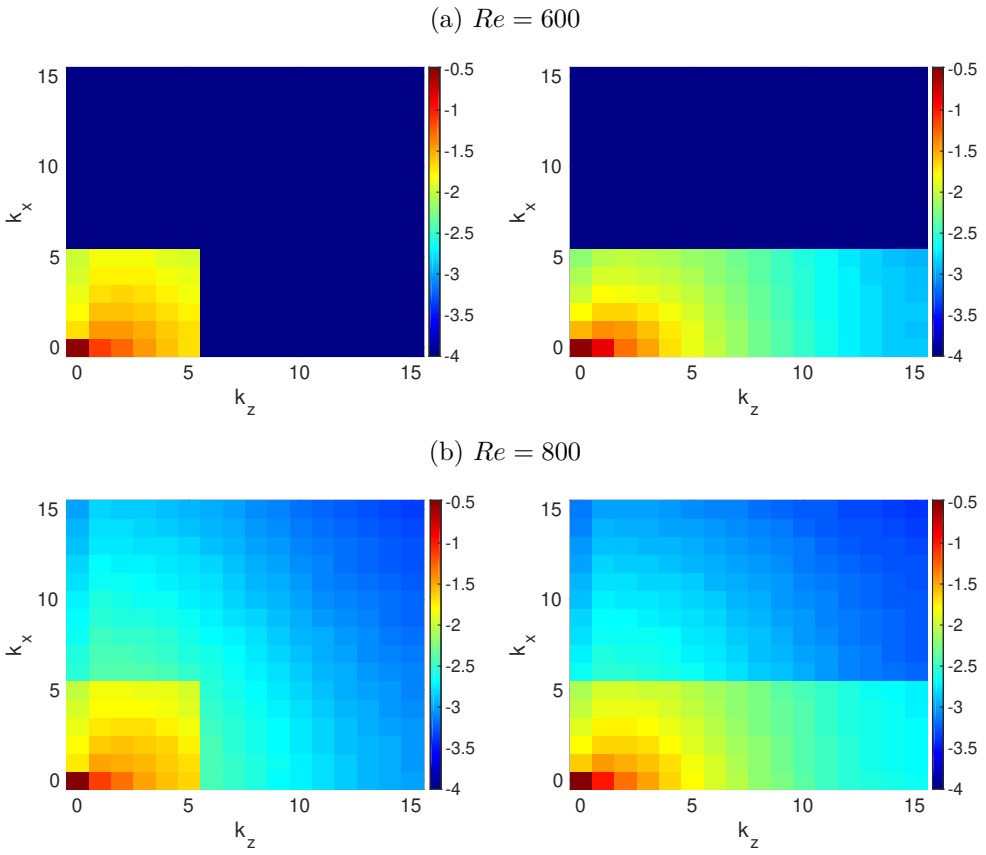

Figure 6.7: Averaged (k_x, k_z)-amplitudes for turbulent trajectories in the generalized quasilinear models with $[\kappa_x, \kappa_z] = [5, 5]$ (left column) and $[\kappa_x, \kappa_z] = [5, 24]$ (right column). Colour-coded is the decadic logarithm of the amplitudes. The rows correspond to $Re = 600$ (top) and $Re = 800$ (bottom).

$Re = 600$	$\bar{D}$	$\bar{I}$	σ_D	σ_I
$\kappa_x = 5,\ \kappa_z = 5$	2.50	2.50	0.32	0.26
$\kappa_x = 5,\ \kappa_z = 24$	2.32	2.32	0.36	0.28
QLA	2.30	2.30	0.56	0.44
nonlinear	2.24	2.24	0.39	0.30

$Re = 800$	$\bar{D}$	$\bar{I}$	σ_D	σ_I
$\kappa_x = 5,\ \kappa_z = 5$	3.19	3.19	0.33	0.26
$\kappa_x = 5,\ \kappa_z = 24$	2.98	2.98	0.35	0.26
QLA	2.83	2.83	0.54	0.43
nonlinear	2.80	2.80	0.37	0.27

Table 6.2: Comparison of mean values and standard deviations of the energy dissipation rate D and the energy input rate I for turbulent trajectories in the generalized quasilinear approximations with $[\kappa_x, \kappa_z] = [5, 5]$ and $[\kappa_x, \kappa_z] = [5, 24]$ to the streamwise quasilinear approximation with $[\kappa_x, \kappa_z] = [0, 24]$ and to the fully nonlinear system. The statistics are calculated for time series of $T = 100\,000$. The tables correspond to $Re = 600$ (top) and $Re = 800$ (bottom).

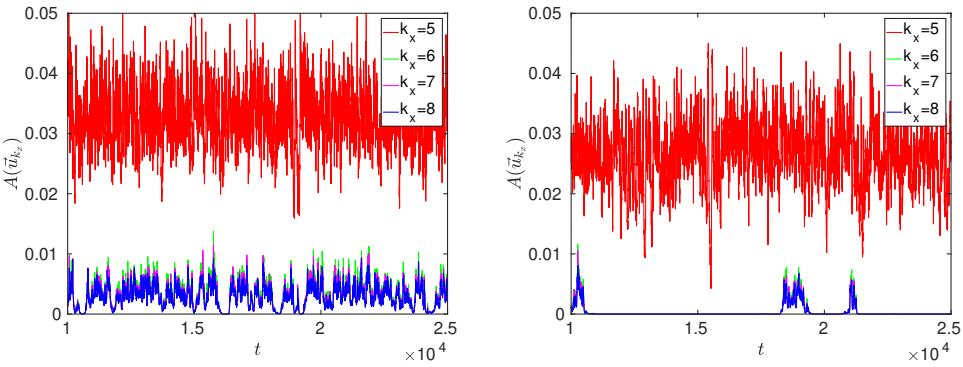

Figure 6.8: Time series of the amplitudes of the modes with $k_x = 5, 6, 7, 8$ for $Re = 650$ for $[\kappa_x, \kappa_z] = [5, 5]$ (left panel) and $[\kappa_x, \kappa_z] = [5, 24]$ (right panel). The emerging modes $k_x = 6, 7, 8$ show intermittent behaviour.

wavenumbers simultaneously become active. The reason is that the GQL allow for a transfer of energy between the small scale modes of group II by interacting with the large scale modes of group I. There are much more possibilities for interactions than for the QLA, where energy between the small scale modes can only be transferred via the mean flow. Figure 6.8 shows the time series of the amplitudes $A(\vec{u}_{k_x})$ of the modes with $k_x = 5, 6, 7$ and 8 for $[\kappa_x, \kappa_z] = [5, 5]$ and $[\kappa_x, \kappa_z] = [5, 24]$ for $Re = 650$ in the left and right panel, respectively. The data shown in the figures reveals that the new modes with $k_x = 6, 7, 8$ not only appear simultaneously and with intermittent time series, but that their active phases are synchronized. This observation also holds for the higher wavenumber modes that are not shown in the figure. When one of the group II modes is activated during the evolution of the flow, all other group II modes become activated simultaneously due to the nonlinear couplings with the large scale modes, which explains the synchronous bursts. However, the individual time series of the modes are different. It is noticeable that the time series for $[\kappa_x, \kappa_z] = [5, 5]$ shows significantly more active phases than the time series for $[\kappa_x, \kappa_z] = [5, 24]$. This observation can be explained by the fact that compared to the case with $[\kappa_x, \kappa_z] = [5, 5]$, the GQL with $[\kappa_x, \kappa_z] = [5, 24]$ has additional fully active modes with higher k_z-wavenumbers (compare figure 6.7). The energy contained in an intermittent burst can thus be carried to these higher wavenumbers where it is dissipated.

In table 6.2 the turbulent statistics are compared to the fully nonlinear system. The mean energy dissipation $\bar{D}$ and energy input $\bar{I}$ with standard deviations σ_D and σ_I are obtained from turbulent trajectories of $T = 100\,000$ time units, the transient phase is not included. While the mean values of the GQL models differ more from those of the nonlinear system than the mean values obtained for QLA, the standard deviations are captured much better by GQL.

6.5 Concluding remarks

With the GQL, the QLA discussed in chapter 5 can be improved in a systematic way. The addition of modes in k_x quickly leads to an improvement of the results compared to the fully nonlinear system. This is because in GQL the small scale

modes which are contained in group II can interact via the large scale modes of group I. A subsequent reduction in the spanwise modes of set I only has little adverse effect on the results as long as there remain enough possibilities to scatter energy between the small scale modes. Since in the generalized models all modes become activated, a reduction of the resolution is not possible without affecting the results. However, the required resolution for the generalized models will be lower than for the full system, because the overall amplitudes of the set II modes are smaller.

7 Conclusions

Much insight into the processes that support the onset of turbulence and maintain the turbulent dynamics in linearly stable shear flows has been gained by applying ideas from dynamical systems theory. This thesis explores the state space of some well-established simplified model systems in terms of these ideas.

In chapter 3 the different nature of deterministic and noise-induced transitions in state space has been analyzed for a 2-d model. The calculation of optimal perturbations with respect to different criteria revealed that in deterministic cases transition is most effectively triggered by vortices. For noise-induced transitions our results suggest that the optimal perturbations are of a different structure due to the stretched probability density function of noisy trajectories. We expect this to be relevant for realistic shear flows.

In chapters 4, 5 and 6 various quasilinear models are investigated from a dynamical systems perspective. An interesting property which all quasilinear models have in common is the zero eigenvalue condition of the matrix in the linear group II equations. This property has been studied in chapter 4 for two low-dimensional models with intrinsic quasilinear structure. The condition that the matrix needs to have one zero eigenvalue for non-trivial fixed points has been used to find the (known) fixed points of the model system. Making use of this self-consistency condition could establish new ways to determine fixed points of quasilinear models.

In contrast to many other simplified models for shear flows, the streamwise quasilinear approximation discussed in chapter 5 is directly obtained from the Navier-Stokes equations. The approximation consists in a separation of the modes into two sets: the streamwise mean with $k_x = 0$ and the streamwise varying modes with $k_x \neq 0$. The modes of set I are treated fully nonlinearly and they are driven by the Reynolds stresses from the modes of set II. For set II all self-interactions are neglected and the modes can only couple to the mean flow.

In this thesis the quasilinear approximation has been implemented into a DNS for plane Couette flow (`channelflow` by J. Gibson) and it has been studied from a dynamical systems perspective. The underlying phase space structure has been explored and compared to the nonlinear system and the results explain the close correspondence between the dynamics of the quasilinear approximation and that of full DNS. We followed exact coherent structures from the full system to the quasilinear system and we compared their properties. A reduction in the number of streamwise modes comes about naturally when the nonlinear couplings between the modes of set II are switched off. Qualitatively, all investigated features of the full system are also present in the approximation. Many of the identified and analyzed equilibria in the quasilinear system and their bifurcation diagrams are very similar to their nonlinear counterparts in spite of the low number of contained streamwise modes. The bifurcation scenario which leads to the formation of a local chaotic saddle has also been found within the quasilinear system. This shows that QLA is capable of capturing many properties of the flow and it provides a good starting point for modelling. Higher streamwise modes can be activated in the quasilinear dynamics through bifurcations and unstable eigenvectors. For the emerging higher streamwise modes we found intermittent time-series reminiscent to those which are present for the dissipation on small scales in fully developed turbulence. This observation should be pursued further and it suggests a hierarchical modelling approach for intermittency.

The class of quasilinear models has been successfully applied to statistical state dynamics of wall-bounded shear flows (Farrell and Ioannou, 2012; Thomas et al., 2014) and to geophysical flows (Farrell and Ioannou, 2007; Tobias and Marston, 2013). It has been shown that within the quasilinear approximation the dynamics are captured surprisingly accurately although a great deal of the nonlinear interactions in the Navier-Stokes equations are omitted.

The streamwise quasilinear approximation is a reduced model which is derived directly from the Navier-Stokes equation and which apparently inherits many of its fundamental features. At the same time the model contains significantly less streamwise modes than the full system which makes it computationally less expensive. The comparison of the streamwise quasilinear approximation with the full DNS in chapter 5 suggests that the mechanisms underlying the onset

of turbulence can be analyzed further within this simplified framework. We are optimistic that the results then can be transfered back to the fully nonlinear dynamics.

The generalized quasilinear approximation investigated in chapter 6 provides a means for systematically improving the streamwise quasilinear approximation by adding further modes to set I. The price of the quantitative improvement of the results is that the reduction in the number of streamwise modes is lost as all modes are activated simultaneously for higher Re. However, the generalized quasilinear approximation can be used for statistical closure in direct statistical simulations (Marston et al., 2016; Tobias and Marston, 2017) and for systematic studies of the modal interactions.

It will be interesting to apply quasilinear approximations to related shear flows and to use the insights gained within this simplyfied setting to derive low-dimensional models.

Bibliography

Andereck, C. D., Liu, S. S. and Swinney, H. L. (1986). Flow regimes in a circular Couette system with independently rotating cylinders, *Journal of Fluid Mechanics* **164**: 155–183.

Avila, K., Moxey, D., de Lozar, A., Avila, M., Barkley, D. and Hof, B. (2011). The onset of turbulence in pipe flow, *Science* **333**(6039): 192–196.

Avila, M., Willis, A. P. and Hof, B. (2010). On the transient nature of localized pipe flow turbulence, *Journal of Fluid Mechanics* **646**: 127–136.

Baggett, J. S. and Trefethen, L. N. (1997). Low-dimensional models of subcritical transition to turbulence, *Physics of Fluids* **9**(4): 1043–1053.

Barkley, D. (2011). Simplifying the complexity of pipe flow, *Physical Review E* **84**: 016309.

Boberg, L. and Brosa, U. (1988). Onset of turbulence in a pipe, *Zeitschrift für Naturforschung A* **43**: 697–726.

Bretheim, J. U., Meneveau, C. and Gayme, D. F. (2015). Standard logarithmic mean velocity distribution in a band-limited restricted nonlinear model of turbulent flow in a half-channel, *Physics of Fluids A* **27**(1): 011702.

Brosa, U. (1989). Turbulence without strange attractor, *Journal of Statistical Physics* **55**: 1303–1312.

Canuto, C., Hussaini, M. Y., Quarteroni, A. and Zang, T. A. (1988). *Spectral Methods in Fluid Dynamics*, Springer Berlin Heidelberg.

Cherubini, S. and De Palma, P. (2013). Nonlinear optimal perturbations in a Couette flow: bursting and transition, *Journal of Fluid Mechanics* **716**: 251–279.

Cherubini, S. and Palma, P. D. (2014). Minimal perturbations approaching the edge of chaos in a Couette flow, *Fluid Dynamics Research* **46**(4): 041403.

Clever, R. M. and Busse, F. H. (1997). Tertiary and quaternary solutions for plane Couette flow, *Journal of Fluid Mechanics* **344**: 137–153.

Cvitanović, P. and Gibson, J. F. (2010). Geometry of the turbulence in wall-bounded shear flows: periodic orbits, *Physica Scripta* **2010**(T142): 014007.

Darbyshire, A. G. and Mullin, T. (1995). Transition to turbulence in constant-mass-flux pipe flow, *Journal of Fluid Mechanics* **289**: 83–114.

de Lozar, A., Mellibovsky, F., Avila, M. and Hof, B. (2012). Edge state in pipe flow experiments, *Physical Review Letters* **108**: 214502.

Duguet, Y., Monokrousos, A., Brandt, L. and Henningson, D. S. (2013). Minimal transition thresholds in plane Couette flow, *Physics of Fluids* **25**(8): 084103.

Duguet, Y. and Schlatter, P. (2013). Oblique laminar-turbulent interfaces in plane shear flows, *Physical Review Letters* **110**: 034502.

Duguet, Y., Schlatter, P. and Henningson, D. S. (2010). Formation of turbulent patterns near the onset of transition in plane Couette flow, *Journal of Fluid Mechanics* **650**: 119–129.

Eckhardt, B. (2018). Transition to turbulence in shear flows, *Physica A: Statistical Mechanics and its Applications* **504**: 121 – 129.

Eckhardt, B., Faisst, H., Schmiegel, A. and Schneider, T. M. (2008). Dynamical systems and the transition to turbulence in linearly stable shear flows, *Philosophical Transactions of The Royal Society A: Mathematical, Physical and Engineering Sciences* **366**: 1297–1315.

Eckhardt, B., Marzinzik, K. and Schmiegel, A. (1998). Transition to turbulence in shear flows, *in* J. Parisi, S. C. Müller and W. Zimmermann (eds), *A Perspective Look at Nonlinear Media*, Springer Berlin Heidelberg, Berlin, Heidelberg, pp. 327–338.

Eckhardt, B. and Mersmann, A. (1999). Transition to turbulence in a shear flow, *Physical Review E* **60**: 509–517.

Eckhardt, B. and Pandit, R. (2003). Noise correlations in shear flows, *The European Physical Journal B* **33**(3): 373–378.

Farrell, B. F. and Ioannou, P. J. (2007). Structure and spacing of jets in barotropic turbulence, *Journal of the Atmospheric Sciences* **64**(10): 3652–3665.

Farrell, B. F. and Ioannou, P. J. (2012). Dynamics of streamwise rolls and streaks in turbulent wall-bounded shear flow, *Journal of Fluid Mechanics* **708**: 149–196.

Gebhardt, T. and Grossmann, S. (1994). Chaos transition despite linear stability, *Physical Review E* **50**: 3705–3711.

Gibson, J. F. (n.d.). Channelflow: a spectral Navier-Stokes solver in C++, `http://channelflow.org`.

Gibson, J. F., Halcrow, J. and Cvitanović, P. (2008). Visualizing the geometry of state space in plane Couette flow, *Journal of Fluid Mechanics* **611**: 107–130.

Gibson, J. F., Halcrow, J. and Cvitanović, P. (2009). Equilibrium and travelling-wave solutions of plane Couette flow, *Journal of Fluid Mechanics* **638**: 243–266.

Grebogi, C., Ott, E. and Yorke, J. A. (1983). Crises, sudden changes in chaotic attractors, and transient chaos, *Physica D: Nonlinear Phenomena* **7**(1): 181–200.

Grossmann, S. (2000). The onset of shear flow turbulence, *Reviews of Modern Physics* **72**: 603–618.

Halcrow, J. J. (2008). *Charting the state space of plane Couette flow: Equilibria, relative equilibria, and heteroclinic connections*, PhD thesis, Georgia Institute of Technology.

Hamilton, J. M., Kim, J. and Waleffe, F. (1995). Regeneration mechanisms of near-wall turbulence structures, *Journal of Fluid Mechanics* **287**: 317–348.

Hof, B., de Lozar, A., Kuik, D. J. and Westerweel, J. (2008). Repeller or attractor? Selecting the dynamical model for the onset of turbulence in pipe flow, *Physical Review Letters* **101**: 214501.

Hof, B., Juel, A. and Mullin, T. (2003). Scaling of the turbulence transition threshold in a pipe, *Physical Review Letters* **91**: 244502.

Hof, B., Van Doorne, C. W. H., Westerweel, J., Nieuwstadt, F. T. M., Faisst, H., Eckhardt, B., Wedin, H., Kerswell, R. R. and Waleffe, F. (2004). Experimental observation of nonlinear traveling waves in turbulent pipe flow, *Science* **305**(5690): 1594–1598.

Hof, B., Westerweel, J., Schneider, T. M. and Eckhardt, B. (2006). Finite lifetime of turbulence in shear flows, *Nature* **443**: 59–62.

Hutchins, N. and Marusic, I. (2007a). Evidence of very long meandering features in the logarithmic region of turbulent boundary layers, *Journal of Fluid Mechanics* **579**: 1–28.

Hutchins, N. and Marusic, I. (2007b). Large-scale influences in near-wall turbulence, *Philosophical Transactions of the Royal Society of London A: Mathematical, Physical and Engineering Sciences* **365**(1852): 647–664.

Kerswell, R. R. and Tutty, O. R. (2007). Recurrence of travelling waves in transitional pipe flow, *Journal of Fluid Mechanics* **584**: 69–102.

Kreilos, T. and Eckhardt, B. (2012). Periodic orbits near onset of chaos in plane Couette flow, *Chaos* **22**(4): 047505.

Kreilos, T., Eckhardt, B. and Schneider, T. M. (2014). Increasing lifetimes and the growing saddles of shear flow turbulence, *Physical Review Letters* **112**: 044503.

Luchini, P. (2010). A thermodynamic lower bound on transition-triggering disturbances, *in* D. Schlatter, P.and Henningson (ed.), *Seventh IUTAM Symposium on Laminar-Turbulent Transition*, Springer, pp. 11–18.

Luchini, P. (2017). Receptivity to thermal noise of the boundary layer over a swept wing, *AIAA Jounal* **55**(1): 121–130.

Marston, J. B., Chini, G. P. and Tobias, S. M. (2016). Generalized quasi-linear approximation: Application to zonal jets, *Physical Review Letters* **116**: 214501.

Mellibovsky, F. and Meseguer, A. (2009). Critical threshold in pipe flow transition, *Philosophical Transactions of the Royal Society of London A: Mathematical, Physical and Engineering Sciences* **367**(1888): 545–560.

Meseguer, Á. and Trefethen, L. (2003). Linearized pipe flow to Reynolds number 107, *Journal of Computational Physics* **186**(1): 178 – 197.

Moehlis, J., Faisst, H. and Eckhardt, B. (2004). A low-dimensional model for turbulent shear flows, *New Journal of Physics* **6**: 56.

Moehlis, J., Faisst, H. and Eckhardt, B. (2005). Periodic orbits and chaotic sets in a low-dimensional model for shear flows, *Siam Journal on Applied Dynamical Systems* **4**(2): 352–376.

Moffatt, H. K. (1990). Fixed points of turbulent dynamical systems and suppression of nonlinearity, Comment 1, *Whither Turbulence? Turbulence at the Crossroads: Proceedings of a Workshop Held at Cornell University*, Department of Applied Mathematics and Theoretical Physics, pp. 250–257.

Monokrousos, A., Bottaro, A., Brandt, L., Di Vita, A. and Henningson, D. S. (2011). Nonequilibrium thermodynamics and the optimal path to turbulence in shear flows, *Physical Review Letters* **106**: 134502.

Morrison, J. F., McKeon, B. J., Jiang, W. and Smits, A. J. (2004). Scaling of the streamwise velocity component in turbulent pipe flow, *Journal of Fluid Mechanics* **508**: 99–131.

Moxey, D. and Barkley, D. (2010). Distinct large-scale turbulent-laminar states in transitional pipe flow, *Proceedings of the National Academy of Sciences* **107**(18): 8091–8096.

Nagata, M. (1990). Three-dimensional finite-amplitude solutions in plane Couette flow: bifurcation from infinity, *Journal of Fluid Mechanics* **217**: 519–527.

Nikolaidis, M.-A., Farrell, B. F., Ioannou, P. J., Gayme, D. F., Lozano-Durán, A. and Jiménez, J. (2016). A POD-based analysis of turbulence in the reduced nonlinear dynamics system, *Journal of Physics: Conference Series* **708**(1): 012002.

Orszag, S. A. (1971). Accurate solution of the Orr–Sommerfeld stability equation, *Journal of Fluid Mechanics* **50**(4): 689–703.

Orszag, S. A. and Kells, L. C. (1980). Transition to turbulence in plane Poiseuille and plane Couette flow, *Journal of Fluid Mechanics* **96**(1): 159–205.

Ortiz de Zárate, J. M. and Sengers, J. V. (2011). Hydrodynamic fluctuations in laminar fluid flow. I. Fluctuating Orr-Sommerfeld equation, *Journal of Statistical Physics* **144**(4): 774–792.

Ortiz de Zárate, J. M. and Sengers, J. V. (2012). Hydrodynamic fluctuations in laminar fluid flow. II. Fluctuating Squire equation, *Journal of Statistical Physics* **150**(3): 540–558.

Pausch, M. and Eckhardt, B. (2015). Direct and noisy transitions in a model shear flow, *Theoretical and Applied Mechanics Letters* **5**(3): 111 – 116.

Pausch, M., Grossmann, F. and Eckhardt, B. (2014). Groebner basis methods for stationary solutions of a low-dimensional model for a shear flow, *Journal of Nonlinear Science* **24**(5): 935–948.

Pausch, M., Yang, Q., Hwang, Y. and Eckhardt, B. (2019). Quasilinear approximation for exact coherent states in parallel shear flows, *Fluid Dynamics Research* **51**(1): 011402.

Prigent, A. and Dauchot, O. (2005). Transition to versus from turbulence in subcritical Couette flows, *in* M. T. and K. R. (eds), *IUTAM Symposium on Laminar-Turbulent Transition and Finite Amplitude Solutions. Fluid Mechanics and its Applications*, Vol. 77, Springer, pp. 195–219.

Prigent, A., Grégoire, G., Chaté, H. and Dauchot, O. (2003). Long-wavelength modulation of turbulent shear flows, *Physica D: Nonlinear Phenomena* **174**(1): 100 – 113.

Pringle, C. C. T. and Kerswell, R. R. (2010). Using nonlinear transient growth to construct the minimal seed for shear flow turbulence, *Physical Review Letters* **105**: 154502.

Pringle, C. C. T., Willis, A. P. and Kerswell, R. R. (2012). Minimal seeds for shear flow turbulence: using nonlinear transient growth to touch the edge of chaos, *Journal of Fluid Mechanics* **702**: 415–443.

Reynolds, O. (1883). XXIX. An experimental investigation of the circumstances which determine whether the motion of water shall be direct or sinuous, and of the law of resistance in parallel channels, *Philosophical Transactions of the Royal Society of London* **174**: 935–982.

Romanov, V. A. (1973). Stability of plane Couette flow, *Functional Analysis and Its Applications* **7**: 137–146.

Rott, N. (1990). Note on the history of the Reynolds number, *Annual Review of Fluid Mechanics* **22**(1): 1–12.

Schmid, P. J. and Henningson, D. S. (1999). *Stability and transition of shear flows*, Springer.

Schmiegel, A. (1999). *Transition to turbulence in linearly stable shear flows*, PhD thesis, Philipps-Universitität Marburg.

Schmiegel, A. and Eckhardt, B. (1997). Fractal stability border in plane Couette flow, *Physical Review Letters* **79**: 5250–5253.

Schneider, T. M., De Lillo, F., Buehrle, J., Eckhardt, B., Dörnemann, T., Dörnemann, K. and Freisleben, B. (2010b). Transient turbulence in plane Couette flow, *Physical Review E* **81**: 015301.

Schneider, T. M., Eckhardt, B. and Vollmer, J. (2007a). Statistical analysis of coherent structures in transitional pipe flow, *Physical Review E* **75**(6): 066313.

Schneider, T. M., Eckhardt, B. and Yorke, J. A. (2007b). Turbulence transition and the edge of chaos in pipe flow, *Physical Review Letters* **99**: 034502.

Schneider, T. M., Gibson, J. F. and Burke, J. (2010a). Snakes and ladders: Localized solutions of plane Couette flow, *Physical Review Letters* **104**: 104501.

Schneider, T. M., Gibson, J. F., Lagha, M., De Lillo, F. and Eckhardt, B. (2008). Laminar-turbulent boundary in plane Couette flow, *Physical Review E* **78**: 037301.

Sengers, J. V. and Ortiz de Zárate, J. M. (2010). Velocity fluctuations in laminar fluid flow, *Journal of Non-Newtonian Fluid Mechanics* **165**(17-18): 925–931.

Skufca, J. D., Yorke, J. A. and Eckhardt, B. (2006). Edge of chaos in a parallel shear flow, *Physical Review Letters* **96**: 174101.

Smith, T., Moehlis, J. and Holmes, P. (2005). Low-dimensional modelling of turbulence using the proper orthogonal decomposition: A tutorial, *Nonlinear Dynamics* **41**: 275 – 307.

Sommerfeld, A. (1908). Ein Beitrag zur hydrodynamischen Erklärung der turbulenten Flüssigkeitsbewegung, *Proceedings of the 4th International Mathematical Congress, Rome* pp. 116–124.

Thomas, V. L., Farrell, B. F., Ioannou, P. J. and Gayme, D. F. (2015). A minimal model of self-sustaining turbulence, *Physics of Fluids A* **27**(10): 105104.

Thomas, V. L., Lieu, B. K., Jovanovic, M. R., Farrell, B. F., Ioannou, P. J. and Gayme, D. F. (2014). Self-sustaining turbulence in a restricted nonlinear model of plane Couette flow, *Physics of Fluids A* **26**(1): 105112.

Tobias, S. M. and Marston, J. B. (2013). Direct statistical simulation of out-of-equilibrium jets, *Physical Review Letters* **110**(10): 104502.

Tobias, S. M. and Marston, J. B. (2017). Three-dimensional rotating Couette flow via the generalised quasilinear approximation, *Journal of Fluid Mechanics* **810**: 412–428.

Trefethen, L. N., Trefethen, A. E., Reddy, S. C. and Driscoll, T. A. (1993). Hydrodynamic stability without eigenvalues, *Science* **261**(5121): 578–584.

Viswanath, D. (2007). Recurrent motions within plane Couette turbulence, *Journal of Fluid Mechanics* **580**: 339–358.

Waleffe, F. (1997). On a self-sustaining process in shear flows, *Physics of Fluids A* **9**: 883–900.

Waleffe, F. (2003). Homotopy of exact coherent structures in plane shear flows, *Physics of Fluids A* **15**(6): 1517–1534.

Danksagungen

Zum Schluss möchte ich mich bei allen bedanken, die mich während der Anfertigung meiner Arbeit unterstützt haben.

An erster Stelle bedanke ich mich herzlich bei meinem Doktorvater Prof. Dr. Bruno Eckhardt für die Betreuung der Arbeit. Danke, dass Ihre Tür bei Fragen immer offen stand. Ich habe es immer als großes Glück empfunden mit Ihnen arbeiten und von Ihnen lernen zu dürfen.

Bedanken möchte ich mich auch bei allen Mitgliedern der AG KoSy für die freundschaftliche Atmosphäre und für die fachliche und moralische Unterstützung.

Regina und Moritz danke ich für das Korrekturlesen der Arbeit.

Allen meinen Freunden danke ich dafür, dass es sie gibt. Regina und Yvonne, bessere Freundinnen als euch kann man sich nicht wünschen.

Von Herzen danke ich meiner Familie für die große Unterstützung und Geduld, besonders während der Zeit des Schreibens. Meinen Großeltern danke ich dafür, dass sie immer fest an mich geglaubt haben. Meinem Bruder Marcell danke ich dafür, dass er mir immer zur Seite steht. Mein Vater Norbert hat mein Interesse für die Naturwissenschaften schon als Kind geweckt. Danke Papa, ohne dich hätte ich diesen Weg vielleicht nicht eingeschlagen. Meiner Mutter Annerose verdanke ich so vieles. Danke Mama, dass du immer für mich da bist. Ohne dich hätte ich das nie geschafft. Und last but not least danke ich meinem Ehemann Chaled und meinem Sohn Luis Emilian für all ihre Liebe und Unterstützung. Ich bin sehr glücklich, euch zu haben.